A Search for Supersymmetry in Di-Lepton Final States using the Razor Variables with the ATLAS Detector

EMMA KUWERTZ

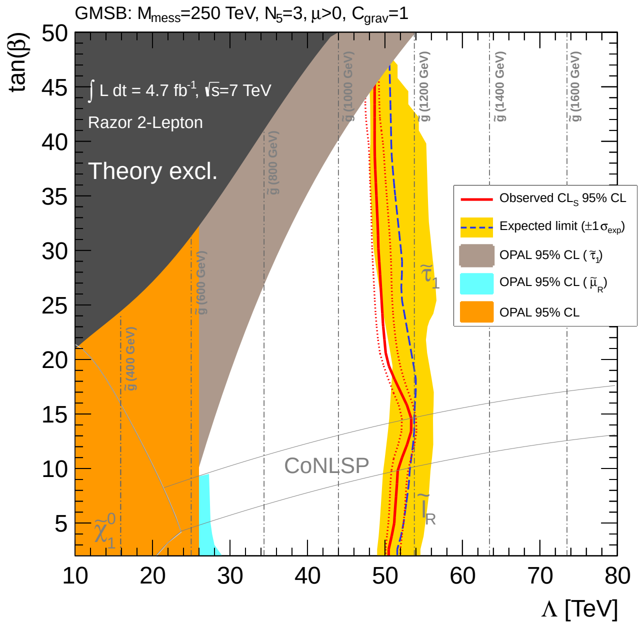

KTH Engineering Sciences

Licentiate Thesis
Stockholm, Sweden 2012

KTH Engineering Sciences

Licentiate Thesis

A Search for Supersymmetry in Di-Lepton Final States using the Razor Variables with the ATLAS Detector

Emma Kuwertz

Particle and Astroparticle Physics, Department of Physics,
Royal Institute of Technology, SE-106 91 Stockholm, Sweden

Stockholm, Sweden 2012

Cover illustration: Razor di-lepton exclusion contours for the GMSB in the $\Lambda - \tan\beta$ plane.

Akademisk avhandling som med tillstånd av Kungliga Tekniska Högskolan i Stockholm framlägges till offentlig granskning för avläggande av teknologie licentiatexamen torsdagen den 18 oktober 2012 kl 15:00 i sal FA32, AlbaNova Universitetscentrum, Roslagstullsbacken 21, Stockholm.

Avhandlingen försvaras på engelska.

ISBN 978-91-7501-327-5
TRITA-FYS 2012:74
ISSN 0280-316X
ISRN KTH/FYS/--12:74--SE

Printed by Universitetsservice US AB 2012

Abstract

A search for supersymmetry in final states with exactly two leptons (electrons or muons) is presented. These leptons can be of any flavour or sign combination, with events being selected by imposing constraints on the Razor variables. The analysis is performed on the full 2011 dataset of proton-proton collisions at 7 TeV centre-of-mass energy, totalling an integrated luminosity of 4.7 fb^{-1}, gathered by the ATLAS experiment at the CERN Large Hadron Collider. No significant deviation from the Standard Model expectation is observed. Exclusion limits are placed on the parameter space of Gauge Mediated supersymmetry, the constrained minimal supersymmetric extension to the Standard Model and simplified SUSY-inspired models.

In addition the nature of noise bursts and sporadically noisy channels in the ATLAS Liquid Argon calorimeter is studied. This includes the development of a tool for use by data quality experts at ATLAS to facilitate the identification and flagging of cells suffering from sporadic noise. This results in an average of less than 0.001% of calorimeter cells being flagged as sporadically noisy in each ATLAS run. The origin of the noise remains unknown, though is shown to display correlations with instantaneous luminosity, particularly in the barrel pre-sampler.

Contents

Introduction

The work contained within this thesis pertains to physics analysis and detector performance studies performed on data collected by the ATLAS detector at the Large Hadron Collider at CERN, Geneva. Chapter 1 outlines the basic concepts of particle physics, summarising the Standard Model as a theory describing the constituents of matter and their interactions. Focus is set on discussing evidence hinting at the limited scope of the Standard Model, with the implication of new physics lying beyond. Particular attention is given to supersymmetry, a theory of new physics which aims to resolve the short-comings of the Standard Model.

In Chapter 2 the Large Hadron Collider and the ATLAS experiment are introduced. An attempt is made to summarise all major accelerator, detector and reconstruction components, with emphasis put on the Liquid Argon Calorimetry system. The structure of the Liquid Argon detection systems and read-out electronics is discussed in detail, in anticipation of the next chapter. Chapter 3 documents several studies regarding the characterisation of, and issues related to, noise in the Liquid Argon Calorimeter.

Chapters 4 and 5 outline definitions concerning the object and event selection associated with the supersymmetry analysis that is the focus of this dissertation. The nature of the dataset and the methods employed to identify various physics object (eg. electrons, muons) as well as event level quantities (eg. missing transverse momentum) are presented first. These explanations are followed with the introduction of the variable set used to achieve signal-to-background discrimination in this analysis, the Razor variables.

The di-lepton Razor analysis, and the collaborative effort amongst the combined Razor analysis team at ATLAS, is presented in Chapter 6. This section lays out the analysis and is mostly dedicated to the identification, understanding and estimation of the background processes contributing to a di-lepton supersymmetry search. In addition, the signal models upon which the search is targeted are detailed.

The analysis results are presented in Chapter 7. Statistical analysis of the signal regions allows the placement of limits on the parameter space of the supersymmetric signal models studied. The resulting exclusions are compared to those of other supersymmetry analyses within the ATLAS community. In addition, the selection power of the variable set used in the signal selection process is scrutinised against alternative variables employed by other new physics analyses. To conclude, the work contained herein is recapitulated and reflected upon in the closing Chapter. Additionally, the potential for future analysis efforts are contemplated and discussed.

Author's Contribution

The work contained within this thesis is the work of the author. All distributions and plots have been generated by the author unless otherwise referenced. Much of the work concerning the Liquid Argon Calorimeter was carried out under the guidance of other collaboration members. The Razor analysis at ATLAS is carried out in a combination of zero-, one- and two-lepton final states, and the author is solely responsible for the two-lepton contribution.

Chapter 1

Theory and Motivation

Particle physicists strive to comprehend the workings of the universe on a fundamental level. The Standard Model of particle physics comprises the current accepted understanding of particles and their interactions. Despite the model's success in its description of observed phenomena, it is not a complete theory. Having been verified to high precision, the Standard Model is not thought to be incorrect, rather it presents a low energy approximation of a more comprehensive theory. Candidates for new physics models, such as Supersymmetry, build upon the Standard Model in an attempt to provide a more complete description of the fundamental laws governing our universe.

1.1 The Standard Model

The Standard Model (SM) [1] is a theory that aims to explain current observations of fundamental particles and the forces between them. It is based upon symmetry arguments and formulated using quantum field theory [2], treating particles as a quantisation of particle fields, to describe the electromagnetic, strong and weak nuclear forces. The symmetries upon which the SM is built result in several quantities that are necessarily conserved, comprising fundamental conditions of the theory. Examples of such quantities include energy, which is always conserved, with some quantities, such as parity or flavour, being conserved only within a given scope. The SM has been a tremendous success, with real-world observations and measurements well matched to its description of physical phenomena. Since its completion in the 1970s it has been probed in detail by experiments, permitting its verification to high precision. The most exceptional feature of the SM promoting its validity is its repeated demonstration of prediction and observation, with a particle's existence being inferred before subsequent discovery. An example of one such particle is the top quark [3].

The Standard Model introduces two main families of particles. Fermions are the matter particles. They have half-integer spin and include leptons and quarks. Bosons are the force-carriers. These have integer-spin and are responsible for propagating the electromagnetic (EM), strong and weak forces. A mechanism fully describing the nature of the gravitational force is yet to be incorporated into the SM. There is, in addition, a particle postulated to be responsible for the fundamental particles acquiring mass. This particle, the Higgs boson, is discussed separately in this section.

1.1.1 Matter

The fermionic particles of the SM constitute the normal matter surrounding us. Fermions themselves are divided into two groups based on their interactions. Quarks possess fractional charge and interact via the strong, weak and EM forces. Leptons do not interact strongly, coupling only to the weak and/or EM forces. There exist a total of twelve known quark and lepton flavours, six of each. These are listed in Table 1.1 with their respective charges and masses. They are grouped together in three so-called "generations," with the lowest mass fermions comprising the first generation and the generations increasing respective of mass thereafter. Only the first generation of quarks and leptons are stable, with second and third generation fermions decaying into their lighter counterparts. In the SM quarks and leptons are described by massless fermionic fields, denoted ψ, according to quantum field theory. As the quanta of a fermionic field, quarks and leptons obey Fermi-Dirac statistics, which results, among other things, in the Pauli Exclusion Principle[1].

The three massive leptons are the electron, the muon and the tau. All of these are negatively charged, with the electron being the only one that is stable. Each of the charged leptons are paired with a neutral lepton called a neutrino. Neutrinos only interact weakly in the SM and so tend to be produced in radioactive decays, or indeed, nuclear reactions such as those that take place in the Sun. As a result of their couplings they are very difficult to detect. Neutrinos were initially thought to be massless until the solar neutrino problem lead to the discovery of neutrino flavour oscillations and the implication of a non-zero mass [4,5]. Each one of the charged leptons is partnered with an anti-lepton, which has the same mass but is oppositely charged. All leptons have "lepton number," $L = 1$ ($L = -1$ for anti-leptons). Leptonic interactions must conserve lepton number, and so this is a conserved quantity in the SM[2].

The six quarks can all interact via the strong, weak and EM forces. These six are the up, down, charm, strange, top and bottom quarks. They carry fractional electric charge and also possess an additional "colour" charge. The value of this additional quantum number can be either "red," "green" or "blue;" or "anti-red," "anti-green" or "anti-blue," in the case of their anti-particles. Individual quarks are not seen in nature, rather they are bound in colourless states known as "hadrons." Hadrons are themselves split into "baryons" and "mesons." A baryon is formed when three quarks, (qqq), comprise a composite particle, with the proton, comprised of two up quarks and one down quark (uud), being one such example. A conserved quantum number concerning quarks is baryon number, B, which takes

[1]The Pauli Exclusion Principle asserts that no two fermionic particles are permitted to occupy the same quantum state simultaneously.

[2]Lepton number is also conserved across lepton flavours.

on values of 1 for baryons and −1 for anti-baryons. Mesons, by contrast, are bound quark–anti-quark states, $(q\bar{q})$, and are assigned $B = 0$. Hadrons such as Δ^{++}, which has quark structure (uuu), demonstrate the significance of colour charge, without which the existence of such a state would be forbidden under the Pauli Exclusion Principle.

Generation	1	2	3	Charge	Mass		
Leptons	e	μ	τ	−1	0.511 MeV	105.7 MeV	1.78 GeV
	ν_e	ν_μ	ν_τ	0		< 2 eV	
Quarks	u	c	t	+2/3	2.3 MeV	1.27 GeV	160-173.5 GeV
	d	s	b	−1/3	4.8 MeV	95 MeV	4.18-4.65 GeV

Table 1.1: The matter particles of the Standard Model with their respective masses and electric charges from Ref. [6].

1.1.2 Forces

Perturbative quantum field theory explains forces as being mediated by messenger particles, which mediate interactions between matter particles. In the SM the so-called "gauge bosons" are the messenger particles. They have integer spin, and they are of four known types. The gluon is a massless vector boson that interacts with coloured particles. As a result, it is responsible for the strong force. The photon is also a massless vector boson, but it interacts only with electrically charged particles and is therefore the mediator of the EM force. The weak force has more than one vector boson associated with it. The $W^\pm$ and Z^0 bosons are massive particles in contrast to their electromagnetic and strong counterparts, with masses of 80.4 GeV and 91.2 GeV respectively. The gauge bosons are summarised in Table 1.2, and the mechanism by which they come to be is discussed further in this section.

Force	Boson	Charge	Mass
Strong	g	0	0
Electromagnetic	γ	0	0
Weak	$W^\pm$	±1	80.3 GeV
	Z^0	0	91.2 GeV

Table 1.2: The gauge bosons of the Standard Model with their respective masses and electric charge from Ref. [6].

Each force in the SM is described by a gauge group. The SM is described by the non-Abelian[3] symmetry group $SU(3)_C \otimes SU(2)_L \otimes U(1)_Y$. The derivation of the SM is based upon demanding gauge invariance under the transformations of this group.

[3]The term non-Abelian is used to describe a group in which not all of the elements commute.

The theory describing the EM force is quantum electrodynamics (QED), and it invokes gauge invariance under $U(1)_Q$ transformations. QED is a relativistic field theory in which observed particles are the result of an excitation of their associated field. The EM field is the interacting field in QED, and its excitation results in the photon, the propagator of the EM force. The photon couples with particles possessing electric charge, such as quarks and the massive leptons. Photons are charge neutral and do not couple to themselves, in-line with the Abelian nature of $U(1)_Q$.

Quantum chromodynamics (QCD) describes the invariance of fermion fields under the $SU(3)_C$ group and corresponds to the strong nuclear force. Only coloured particles interact via the strong force, thus strong interactions are limited to the quarks and their anti-particles in addition to the associated gauge boson. The colour quantum number permits gluons to undergo self-interactions, with gluons existing in a superposition of combined colour–anti-colour states. These colour combinations result in there being eight massless gluons. Colour charge is a conserved quantity in $SU(3)_C$, and QCD dictates that free particles cannot exist with colour. In this spirit free quarks and gluons have never been observed.

The invariance of fermion fields under $SU(2)_L$ transformations describes the weak nuclear force, where here the L subscript indicates left-handed fermion interactions. Fermion fields are comprised of left- and right-handed components: $\psi = \psi_L + \psi_R$. The weak interaction concerns only the left-handed components of the fermion fields, a demonstration of the weak interaction's violation of parity conservation. It is a short range interaction, hinting towards a massive messenger particle.

The Electroweak (EW) theory culminates the understanding of the weak interaction and QED as a unified gauge theory. This demands invariance under $SU(2)_L \otimes U(1)_Y$ transformations. Here the electromagnetic interactions are described by a combination of $U(1)_Y$ and $SU(2)_L$, in contrast to $U(1)_Q$ that concerns only the EM force according to QED. The conserved quantity in QED is electric charge (Q), whereas $SU(2)_L$ demands conservation of isospin (third component), I_3, and in $U(1)_Y$ the conserved quantity is hypercharge, Y. The relationship between these quantities is given by:

$$Q = I_3 + \frac{1}{2}Y. \tag{1.1}$$

The $SU(2)_L$ symmetry gives rise to three massless bosons, $W_\mu^{1,2,3}$, and the non-Abelian nature of the group allows these to undergo self-interactions. The $U(1)_Y$ symmetry contributes one additional massless boson, B_μ.

At this point in the theory, all EW bosons are massless. Of course this is conflicting with observations in nature, since only the photon is found to possess zero mass and the nature of the weak force indicates that massive gauge bosons are required as mediators. Additional problems arise from the fact that $SU(2)_L$ requires massless fermions, just as QCD demands that quarks possess no mass. In order for the weak gauge bosons, and indeed the fermions, to have acquired mass, the EW symmetry must be a broken symmetry.

1.1.3 The Higgs Mechanism

To explain the presence of massive fermions and weak vector bosons, the $SU(2)_L \otimes U(1)_Y$ symmetry governing EW theory must spontaneously break, leaving distinct $U(1)_Q$ and $SU(2)_L$ components. The Higgs mechanism offers a solution. This mechanism proposes the existence of a Higgs field, a complex scalar field that possesses a non-zero vacuum expectation value (VEV). This VEV is not invariant under $SU(2)_L \otimes U(1)_Y$ gauge transformations, and therefore breaks the $SU(2)_L \otimes U(1)_Y$ symmetry. The symmemetry breaking results in mass terms in the SM Lagrangian for quarks and leptons. Mixing of the gauge bosons from $SU(2)_L \otimes U(1)_Y$ result in the charged $W^{\pm}$-boson fields

$$W^{\pm} = \frac{W^1_\mu \mp iW^2_\mu}{\sqrt{2}}, \tag{1.2}$$

the neutral Z-boson fields

$$Z^0 = cos\theta_w W^3_\mu - sin\theta_w B_\mu, \tag{1.3}$$

and the massless photon field

$$A^\mu = cos\theta_w B_\mu + sin\theta_w W^3_\mu, \tag{1.4}$$

where θ_w is the weak mixing angle. The fact that Z^0 includes an EM component results in its ability to couple to right-handed fermions, while the $W^{\pm}$ is restricted to left-handed interactions.

The excitation of the scalar Higgs field gives rise to a neutral scalar boson. This proposed boson couples to weak gauge bosons and fermions in proportion to the mass they acquire from interacting with the Higgs field itself. Since the Higgs mechanism has been put forward as an explanation of EW symmetry breaking and describes the origin of mass in the SM, the SM is essentially incomplete without it. Originally suggested in 1964, the Higgs has been fervently sought after by particle physicists for decades. The elusive boson proved difficult to find, with the limits being placed on the possible Higgs mass resulting in the accepted mass range becoming ever narrower.

On July 4$^{\text{th}}$, 2012, the ATLAS [7] and CMS [8] experiments formally announced the discovery of a new boson with properties consistent with a Higgs boson. Each experiment made the observations independently, quoting a Higgs mass, m_H, of $126\pm^{0.4(stat.)}_{0.4(syst.)}$ GeV [9] and $125.3\pm^{0.4(stat.)}_{0.5(syst.)}$ GeV [10], respectively.

1.1.4 Short-comings of the Standard Model

The SM has been introduced as a physics success, describing and predicting observations in nature with satisfactory, and sometimes astounding, accuracy. Unfortunately the SM does not provide a complete picture. There is no obvious candidate particle to explain the nature of dark matter, which will be discussed in the coming sections, and the SM fails to confront the matter – anti-matter asymmetry in the universe. Gravity is not incorporated into the SM, with the strength of the gravitational force being many orders of magnitude lower than the strength of the other forces. In fact the gravitational force does not reach a strength comparable to that of the other forces until energies approaching 10^{18} GeV, with possible unification of the four forces occurring around the Planck scale, $\Lambda_{PL} \sim 10^{19}$ GeV. The reason for this hierarchy of scales in physics is a mystery, and it leads to the hierarchy problem [11], explained below.

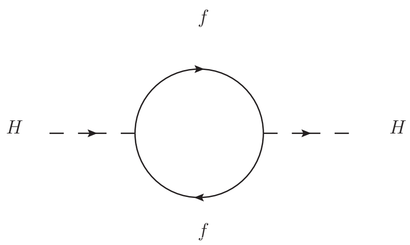

Figure 1.1: Feynman diagram depicting a fermion loop, contributing a correction to the Higgs mass.

The Higgs boson mass, both by necessity and according to recent observations, is at the EW scale of $\sim$ 100 GeV ($\sim$ 125 GeV according to recent experimental results). This mass is subject to radiative corrections from quantum loop interactions with fermions and bosons. An example of such a loop is shown in Figure 1.1. These quantum corrections are of order $\Delta m_H^2 \sim f^2\Lambda^2$, where f is a factor containing other terms (including the mass of the particle the Higgs is coupling to and the associated coupling squared), and Λ is the cut-off scale of the theory. That is to say, the Higgs mass term is sensitive to the scale of physics beyond the EW scale. For a cut-off scale of $\Lambda \sim 1$ TeV the corrections to the Higgs mass are small, with large divergences being avoided. If the SM as it is now were the final word, and therefore considered valid up to Λ_{PL}, the Higgs mass will be subject to enormous corrections $\sim \Lambda_{PL}^2$. The quantum corrections to the physical Higgs mass term would require the bare Higgs mass to be $\mathcal{O}(\Lambda_{PL})$ before the loop corrections. The model then needs to be fine-tuned such that quadratic terms of this order cancel to within $\sim$ 100 GeV. Such exact tuning without adequate physical motivation spoils the naturalness of the theory, making it far less attractive. This problem serves as motivation for theories suggesting the existence of new physics between the EW and Planck scales, with the SM being a low energy approximation valid up to $\Lambda \sim 1$ TeV.

1.2 Supersymmetry

Supersymmetry (SUSY) is a theory that postulates a new symmetry between fermions and boson such that every SM boson has a fermionic "super partner," and every SM fermion a bosonic "super partner." These SUSY particles, or "sparticles," are identical to their SM counterparts in every way with the exception of the difference in spin. The naming convention for these new particles is to add the prefix s- for the super partner of a SM fermion, and the suffix -ino to the super partner of a SM boson. For example the super partner of an electron is a selectron, $\tilde{e}$, and the gluons super partner is known as the gluino, $\tilde{g}$. Supersymmetric particles are labelled with a tilde, as shown above, in order to distinguish them from their SM counterparts. A summary of the SM particles and their SUSY partners is given in Table 1.3.

SM particle	Spin	Super partner	Spin
ℓ q	$\frac{1}{2}$	$\tilde{\ell}$ $\tilde{q}$	0
g B $W^{\pm}, W^0$	1	$\tilde{g}$ $\tilde{B}$ $\tilde{W}^{\pm}, \tilde{W}^0$	$\frac{1}{2}$
$H_u^+, H_u^0, H_d^-, H_d^0$	0	$\tilde{H}_u^+, \tilde{H}_u^0, \tilde{H}_d^-, \tilde{H}_d^0$	$\frac{1}{2}$

Table 1.3: The particles of the Standard Model and their MSSM super partners.

As with the Standard Model, supersymmetry invokes quantum field theory, and the gauge theory upon which it is based leads to the introduction of two sets of fields. Chiral fields associated with the SM fermions produce their bosonic SUSY counterparts. The nature of this field results in left-handed and right-handed fermions being treated differently, with right-handed fermions becoming members of these chiral fields by way of their charge conjugate. This results in the two projections being treated as separate particles in SUSY. In the case of the SM bosons, vector fields link with the associated fields of the SM gauge bosons to produce fermionic super partners.

If SUSY represents an exact symmetry between fermions and bosons, then sparticles would be expected to possess masses identical to those of their SM counterparts. Experiments denounce the existence of, for example, a particle with identical mass to that of the electron whose spin differs by one half integer. The conclusion is that SUSY is a broken symmetry. It is thought that SUSY breaking is analogous to electroweak symmetry breaking, although the mechanism responsible for SUSY breaking is unknown. There are a number of models that attempt to explain the occurrence of SUSY breaking, and the details concerning each of these impact the features and phenomenology of SUSY.

The reason for SUSY being a favoured theory to provide an extension to the SM is its natural introduction of a large number of particles. The hierarchy problem has already been discussed, but the introduction of these new particles to the SM could counteract the divergences of the Higgs mass corrections. These loop corrections can be written in terms of the fermionic and bosonic contributions, as

$$\Delta m_H^2 \sim \lambda_f^2(\Lambda^2 + m_f^2 ...) - \lambda_B(\Lambda^2 + m_B^2 ...), \tag{1.5}$$

where λ_f and λ_B are the couplings of the Higgs to the SM fermions and bosons respectively, m_f and m_B the fermion and boson masses. The addition of sparticles to the SM results in each fermionic term earning one extra bosonic contribution, and vice versa. From Equation 1.5 this resolves the quadratic divergences naturally for the case $\lambda_f^2 = \lambda_B$, providing an elegant solution to the hierarchy problem. The naturalness of this cancellation is preserved provided the difference in mass between SM particles and their super partners is not beyond $\mathcal{O}(1)$ TeV.

1.2.1 Minimal Supersymmetric Standard Model

The extension to the SM which requires the introduction of the minimum number of particles, and therefore the fewest adjustments, is called the Minimal Supersymmetric Standard Model (MSSM). Mass terms are added to the SM Lagrangian, constrained such that the hierarchy problem remains resolved. The first most noticeable modification concerns the Higgs mechanism. Given the nature of the chiral fields introduced in the implementation of SUSY, the single scalar Higgs field is not sufficient to give mass to both left- and right-handed fermions. One additional scalar field is introduced to compensate. In the SM the Higgs field is a doublet, and of the four associated degrees of freedom only one remains as a consequence of EW symmetry breaking, resulting in one Higgs boson. The two Higgs doublets of the MSSM are

$$H_u = \begin{pmatrix} H_u^+ \\ H_u^0 \end{pmatrix}, \qquad H_d = \begin{pmatrix} H_d^0 \\ H_d^- \end{pmatrix};$$

which total eight degrees of freedom, three of which are lost in EW symmetry breaking. There are therefore five Higgs bosons in the MSSM: h^0, H^0, H^+, H^-, A^0. The one that most closely resembles the Higgs boson of the Standard Model is h^0, which is the lightest of the five.

In the SM, mixing of the electroweak gauge bosons yield the mass eigenstates γ, Z and $W^\pm$. In the MSSM the charge neutral higgsinos and gauginos mix to form the four neutralinos: $\tilde{\chi}_1^0, \tilde{\chi}_2^0, \tilde{\chi}_3^0, \tilde{\chi}_4^0$. Similarly the charged higgsinos and winos mix resulting in two charginos: $\tilde{\chi}_1^\pm, \tilde{\chi}_2^\pm$.

In the MSSM baryon and lepton number violating couplings are allowed. This is problematic as it implies that a proton can decay, with a lifetime of around 10^2 s, to final states including leptons and mesons. In fact, the proton is observed to be stable, with a lifetime lower limit of 1.6×10^{33} years according to experiment [12]. This motivates the introduction of a new conserved quantum number called "R-parity," defined as

$$R = (-1)^{3(B-L)+2s} \tag{1.6}$$

where B and L are baryon and lepton number, and s denotes the spin. SM particles and SUSY sparticles have R-parity $+1$ and -1 respectively. The conservation of this quantum number influences the phenomenology of the MSSM greatly. R-parity is multiplicative, incurring the need for sparticles to be created in pairs. Furthermore each sparticle must decay into an odd number of sparticles thereafter to ensure R-parity conservation. Consequently the lightest supersymmetric particle (LSP) must be stable in R-parity conserving SUSY models. Naturally the properties of the LSP vary according to the SUSY model with which it is associated, though there are some inherent constraints on its nature. Since no such particle has as yet been observed, the LSP must be non-baryonic, charge neutral and weakly interacting. A particle fitting these criteria presents an excellent candidate to account for the elusive dark matter in the universe.

The existence of dark matter was first inferred as a result of an observed inconsistency between the mass estimated from galaxy rotation curves and that from their luminosity [13]. The difference in mass estimates is by no means insignificant, with a discrepancy of two orders of magnitude between the estimated and visually observed mass of the Coma cluster of galaxies, indicating a large presence of non-luminous (dark) matter. Experimental constraints can be put on model parameters in order to refine SUSY scenarios. Distance measurements from type 1a supernovae combined with measurements on the cosmic microwave background (CMB) from the Wilkinson Microwave Anisotropy Probe (WMAP) [14] yield the approximate dark matter and dark energy densities of our universe.

1.2.2 Supersymmetry Breaking

The MSSM is formulated by adding the fewest new particles to the SM. Even with the "minimal" adjustments produced by the MSSM, it contains 105 associated parameters. This presents a challenge for making predictions regarding the nature and phenomenology of SUSY interactions. Conventionally the vast parameter space of the MSSM is constricted upon applying physically motivated simplifications to the MSSM. The MSSM can be refined further upon assuming the SUSY is broken due to fields as yet unobserved in the SM, which do not couple to the "visible" MSSM particles. SUSY breaking therefore occurs in a "hidden" sector, the effects of which are propagated to the SUSY sector via some particle exchange. Many models based on this framework exist, two of which are further discussed in the following.

mSUGRA

One of the models attempting to explain how SUSY breaking could be communicated to the MSSM from the hidden sector is minimal SuperGravity (mSUGRA). Here gravitational interactions mediate SUSY breaking from the hidden sector, with these interactions originating from new physics occurring beyond 10^{10} GeV. The introduction of mSUGRA constrains the MSSM greatly, reducing the number of associated parameters from 105 to 5. For this reason the mSUGRA interpretation of the MSSM is often referred to as the constrained Minimal Supersymmetric Standard Model (cMSSM).

The five parameters characterising mSUGRA are m_0, the GUT scale unified scalar mass; $m_{1/2}$, the GUT scale unified gaugino mass; A_0, the trilinear coupling; $\tan\beta$, where β is the ratio of the H_u and H_d VEVs; and sign(μ), the sign of the higgsino mass parameter.

GMSB

In Gauge Mediated Supersymmetry Breaking (GMSB), SUSY breaking is mediated by gauge interactions, communicated from the hidden sector via a so-called "messenger" sector. The messenger fields couple to the MSSM and the hidden sector, with the latter yielding a characteristic supersymmetric mass of the order M_{mess}, and mass-squared splittings of order F. Within the messenger sector the scale of SUSY breaking is $\sqrt{F}$, with the scale of SUSY breaking in the SUSY sector approximately $\Lambda = F/M_{mess}$. The messenger sector itself is comprised of N_i superfields ($i = 1, ..., n$), the excitation of which result in messenger particles. The squarks, sleptons and gauginos get their masses as a result of gauge interactions with the messenger particles, with the masses being determined by the strength of the gauge couplings and the SUSY mass scale, Λ.

There are six free parameters associated with the GMSB. The SUSY mass scale, Λ, typically expected to be $1 - 100$ TeV to ensure the cancellation of the quadratic divergences in the Higgs loop corrections are not overly fine-tuned, with sparticles at the weak scale (~ 100 GeV). Second is the messenger mass, M_{mess}, indicating the mass scale of SUSY breaking in the messenger sector. The number of messenger fields, denoted N, influences the sparticle mass spectrum, with $m_{sfermion} \propto \sqrt{N}$ and $m_{gaugino} \propto N_i$. The ratio of the Higgs VEVs, $\tan\beta$, is a free parameter in the GMSB similarly to mSUGRA, as is sign(μ). Finally C_{grav} dictates the lifetime of the next-to-lightest supersymmetric particle (NLSP).

Chapter 2

The ATLAS Experiment and the LHC

The Large Hadron Collider (LHC) at CERN (European Organisation for Nuclear Research) is the largest scientific experiment in history. After a year of repairs following a fault in 2008, the LHC is now successfully colliding proton beams in the 27 km accelerator ring, located 100 m beneath the Swiss-Franco boarder in the tunnel which used to house the Large Electron-Positron Collider (LEP). A faulty electrical connection between two bending magnets caused a magnet quench, damaging 53 magnets and resulting in the loss of approximately six tonnes of liquid helium. This meant that the LHC was not ready for operation until almost a year later. In the early hours of November 30th 2009, the proton beams were accelerated to an impressive 1.18 TeV, exceeding the 0.98 TeV reached by the US Fermi National Accelerator Laboratorys Tevatron collider. This makes the LHC not only the largest, but the highest energy particle accelerator in the world. Its successful operation marks the beginning of a new era for particle physics.

Collisions occur at four points around the LHC at the sites of the four main experiments, ALICE (A Large Ion Collider Experiment) [15], ATLAS (A Toroidal LHC ApparatuS) [7], CMS (Compact Muon Solenoid) [8], and LHCb (Large Hadron Collider beauty) [16]. An overview of the LHC ring and the position of each of the experiments therein is shown in Figure 2.1. LHCb specialises in physics associated with the b-quark, while ALICE studies collisions of lead nuclei, in a bid to understand the strong interaction at high energy densities. CMS and ATLAS are both multi-purpose detectors designed to search for new physics beyond the Standard Model.

2.1 The Large Hadron Collider

By pushing the energy frontier in particle collisions, searches at the LHC are permitted to explore the nature of physics at the TeV scale. In 2011 the LHC provided proton-proton collisions with a centre of mass energy ($\sqrt{s}$) of 7 TeV, still only half

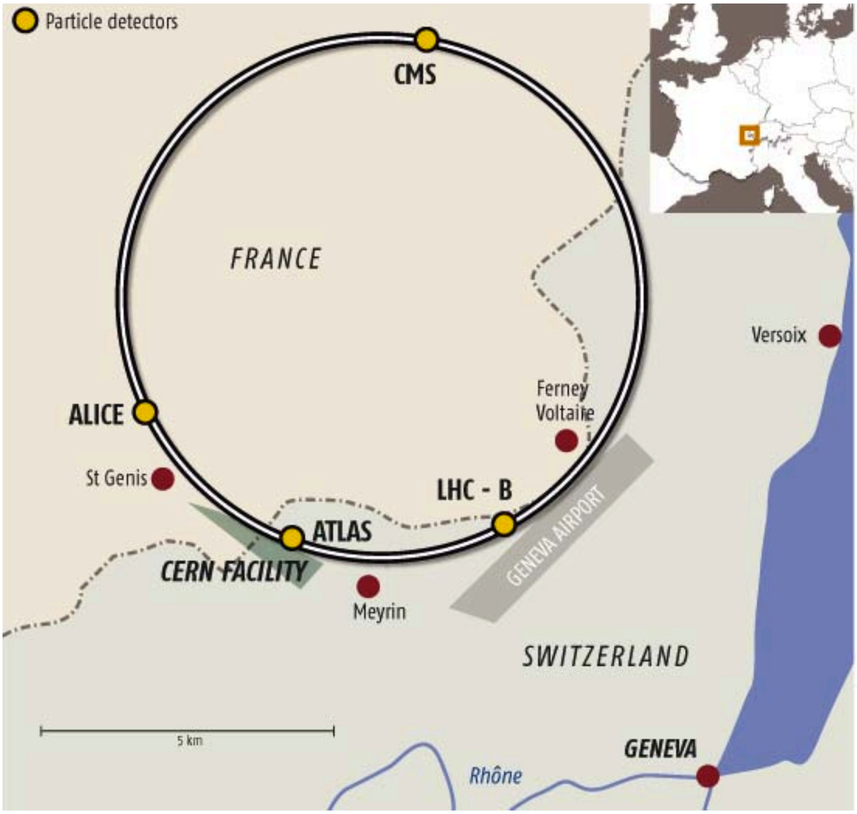

Figure 2.1: An overview of the LHC and the location of the four interaction points, one for each experiment. ATLAS is situated on the Swiss side of the ring right beside the main CERN site.

its design energy. The proton beams are comprised of “bunches” (1380 during 2011 data–taking[1]) of $\sim 10^{11}$ protons which collide 20 million times each second. This bunch structure ensures that collisions occur at the desired collision points, where the bunches cross paths. Each bunch was separated from the next by 50 ns, on average, during 2011. With so many protons packed into each bunch, multiple proton-proton collisions are associated with each bunch–crossing, resulting in an average of ~ 10 interactions per bunch-crossing in 2011. This number more than doubles in 2012, and the centre-of-mass energy increases to of 8 TeV.These multiple collisions per bunch–crossing leads to a “pile-up” of events. Such conditions demand high performance detectors in order to resolve individual events, and the effects of event pile-up must be well understood. This is a challenging task, but new physics processes, such as those from Supersymmetry, are incredibly rare compared with far more common SM processes. This means that the LHC must provide a large number of collisions in order to yield a sample of interesting events significant enough to be isolated and identified. It is the luminosity of a particle accelerator

[1]This was the optimum number of colliding bunches in the LHC during 2011, though this number was approached gradually, increasing in steps from 48 in April reaching 1308 in June.

which dictates the number of events per unit cross-section per second that it is possible to achieve. The luminosity of a collider is defined as:

$$L = \frac{\nu \times \gamma \times N_b \times N_p^2}{4 \times \pi \times \epsilon \times \beta^*} \times F \qquad (2.1)$$

where ν is the collision frequency, γ is the relativistic gamma factor for the protons, N_b is the number of proton bunches in the beam pipe, N_p is the number of protons per bunch, F describes a geometric characteristic due to the fact that the beams cross at an angle, ϵ is the transverse beam emittance and β^* is the β function of the beam at the collision point. Both ϵ and β^* are quantities describing the spread of the beam in both position and momentum space. In 2011 the peak instantaneous luminosity delivered at the LHC reached 3.6×10^{33} cm^{-2}s^{-1}, 36% of its design luminosity of 10^{34} cm^{-2}s^{-1}. If the instantaneous luminosity of the LHC describes the rate at which interactions occur, then this quantity may be integrated over time to yield the total size of the collected data set. It is, therefore, common to quote the dataset size in units of inverse cross-section. The rate of data acquisition at ATLAS for the years 2010 through to 2012 can be seen in Figure 2.2. A set of LHC operating parameters and their values for the 2011 proton-proton runs can be found in Table 2.1.

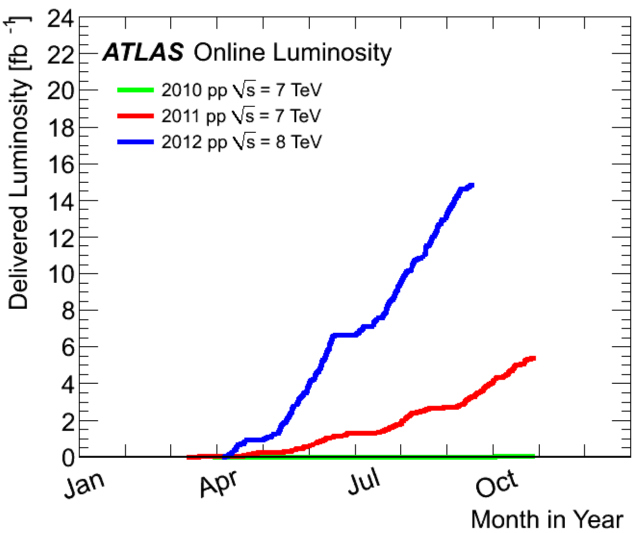

Figure 2.2: Cumulative luminosity as a function of day during 2010, 2011 and 2012 proton-proton collisions [17].

Before entering the LHC tunnel, the protons are accelerated in a number of stages through several smaller accelerators comprising the LHC injector complex. A schematic of the LHC and associated accelerators is shown in Figure 2.3. Protons are produced in a small linac, called Linac-2. Here the protons are accelerated, following their production, up to approximately 50 MeV. These protons then enter the Proton Synchrotron Booster where they are further boosted to 1.4 GeV before

Parameter	Value
Centre-of-mass energy	7 TeV
Number of bunches per beam	1380
Number of protons per bunch	$1.2–1.5 \times 10^{11}$
Bunch spacing	50 ns
Peak instantaneous luminosity	3.65×10^{33} cm^{-2}s^{-1}
Mean interactions per bunch crossing	3–20
Beam spot	34 μm
β^*	1.0 m
ϵ	2.4 μm
Relativistic γ-factor	3730
Geometric crossing factor	0.95
Beam crossing angle	200 μrad

Table 2.1: LHC operating parameters for 2011.

being fed into the Proton Synchrotron, where they are accelerated to energies of 26 GeV. The proton bunches are held together by means of the radio frequency (RF) acceleration system used in the accelerator, where the bunches tend to sit at the points of minimum RF. The Proton Synchrotron can hold up to seven proton bunches at a time, though in practice only six "spaces" tend to be filled. This "abort gap" is imperative to the clean transfer of proton bunches between accelerator systems, as well as the eventual dumping of the beam altogether from the main LHC ring. During the abort gap, "kicker magnets" within the rings are quickly switched on. The magnetic field deflects the proton bunches out of the ring and on to the next accelerator system. Ensuring a gap of a few μs prevents protons bunches from passing between the magnets as they are turning on. Should this happen, the protons would be deflected in the wrong direction, presenting a radiation hazard and the risk of serious damage to the equipment.

From the Proton Synchrotron the protons are directed to the Super Proton Synchrotron (SPS) to be accelerated further to 450 GeV. Once the protons have completed this series of acceleration stages, they are ready to be injected into the main LHC ring. This process continues until the two counter-rotating beams in the LHC tunnel are filled with proton bunches. Following injection, the magnets are ramped up to gradually increase the energy of each beam to half the target centre-of-mass energy (3.5 TeV per beam during 2011). Running at full capacity, the LHC will be capable of achieving energies of up to 7 TeV per beam, resulting in a centre of mass energy of 14 TeV. In order to obtain such energies, 8.4 T superconducting magnets are used to bend the proton beams along the beam pipe. This is done using 1232 dipole magnets along the LHC ring, in addition to over 3500 quadrupole corrector magnets which focus the beam. There are additional magnets which provide higher order corrections. Superfluid helium ensures the magnets remain superconducting at a temperature of 1.9 K.

Once the beams have been successfully ramped up to operation energy, they go through a "squeezing" stage. The beams are compressed in the transverse plane

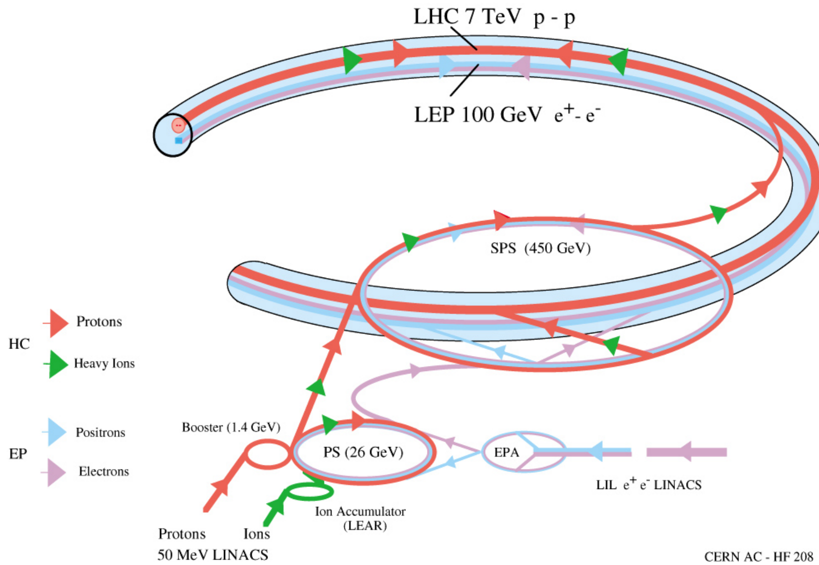

Figure 2.3: Schematic drawing of the Large Hadron Collider and its injection complex. Also shown are the electron–positron accumulator (EPA) and the linear accelerator used for LEP (LIL).

so as to concentrate the beam and maximise the number of interactions per bunch crossing. When the proton beams have undergone all required adjustments and are colliding at the desired centre-of-mass energy, LHC control declares that the beams are in a "stable" state. This condition is called "stable beams" and should always be true for data in use for physics analyses, though in practice experiments will enforce their own additional data-taking requirements. At ATLAS once stable beams have been achieved, the detector and experiment itself must too be declared "ready for physics." This condition is typically satisfied within a minute or two of stable beams, and involves switching on many of the ATLAS detector sub-systems. In particular the parts of the detector nearest the beam pipe are not switched on until the beams are "stable," so as not to risk beam splash damaging delicate detector components. The longer the run duration, the more the instantaneous luminosity drops off until after a beam duration of approximately 15 hours the beam must be dumped and the whole setup started over. As more and more proton collisions occur over time, the proton population within the beam decreases, resulting in this luminosity drop. This means that the instantaneous luminosity obtained at an interaction point in the LHC is always changing, becoming lower over time. The beam dump marks the end of the current LHC "fill," and more protons must then go through the setup, injection and ramping process all over again. At ATLAS the run duration is split into so-called "lumi-blocks" (LBs), small sections of time where the luminosity is approximated to be constant. During 2011 one LB corresponded to ~ 60 s, and so it is LBs themselves that are flagged as having stable beams and being ready for physics, making it easier to keep track of the beam conditions and detector state over time.

2.2 The ATLAS Detector

The ATLAS detector (shown in Figure 2.4) is 44m in length, 25m in diameter, and weighs an enormous 7,000 tonnes, making it the largest[2], of the four main experiments situated around the LHC tunnel. As it is a multi-purpose detector, its objectives are broad, including searching for Supersymmetric particles, the Higgs boson, and any other new physics, as well as carrying out precise measurements of SM particles. In this way ATLAS will aim to achieve both a better understanding of the SM at high energies and an insight into any physics that exists beyond the SM.

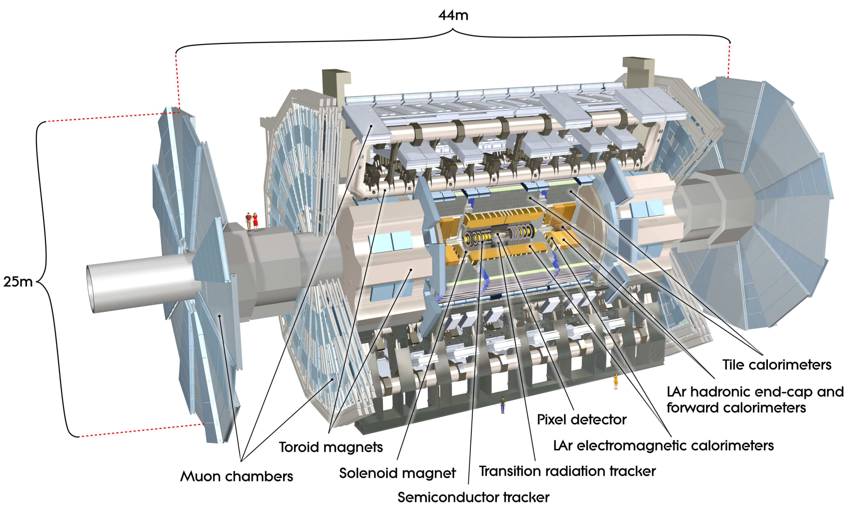

Figure 2.4: The ATLAS detector.

The ATLAS detector coordinate system is defined with the positive x-axis pointing towards the ring's centre and the positive y-axis pointing upwards. The z-axis points along the beam pipe following the beam line in the anti-clockwise direction. The interaction point is defined at $\sim z = 0$, and the detector is "split" at this juncture into two halves denoted the "A" ($z > 0$) and "C" ($z < 0$) sides of the detector. Since the ATLAS detector is itself cylindrical it is convenient to define the transverse radius from the beam line, r, as $\sqrt{x^2 + y^2}$. Then θ represents the polar angle with respect to the z-axis and ϕ is the azimuthal angle around the z-axis as measured with respect to the x-axis.

[2]Though it is the largest, ATLAS is not the heaviest detector at the LHC. The CMS detector weighs in at over 12,500 tonnes, even though it is far smaller than ATLAS!

As the LHC is a pp (proton - proton) collider, measuring particle momenta and energies becomes complex due to the fact that protons are themselves not fundamental particles. It is the constituent partons that will interact upon collision rather than the proton system as a whole. The energy and momentum of individual partons cannot be known, since the momentum is not shared equally between constituents but follows a more complex parton distribution function. With this in mind, particle energies and momenta measured at ATLAS are quoted normally in the transverse plane. Transverse momentum is defined as:

$$p_T = \sqrt{p_x^2 + p_y^2}, \tag{2.2}$$

where p_x and p_y are the x and y components of the momentum and the total p_T in an event sums to ∼zero, with a slight offset due to the fact that the beams cross at an angle. Similarly for transverse energy:

$$E_T = \sqrt{E_x^2 + E_y^2}. \tag{2.3}$$

An additional quantity to note here is the rapidity of a particle, which describes its angle relative to the beam pipe and is formally defined in terms of a particle's energy and momentum:

$$y = \frac{1}{2} \ln \left[\frac{E + p_z}{E - p_z} \right] \tag{2.4}$$

An attractive feature of this quantity is that differences in particle rapidity are invariant under Lorentz transformations along the z-axis, which is useful since the p_z of a particle is normally unknown. In the relativistic limit where the approximation $\beta \sim 1$ holds, pseudorapidity, η, is used as an approximation to true rapidity. Pseudorapidity is useful as it is a function of θ rather than the usually unknown E and p_z parameters, and is defined as:

$$\eta = -\ln \left[\tan \frac{\theta}{2} \right] \tag{2.5}$$

Since η has the same value for all objects at a given θ independent of mass, it is used in place of y to denote not only particle and physics object positions, but also to describe the position of components of the detector itself. The ATLAS detector covers the range $|\eta| < 4.9$. Particles close to the beam pipe have high η and are described as being "forward," whereas particles which stray further from the beam pipe have small η and are "central."

The ATLAS detector is comprised of multiple sub-detector systems, with each of these constituent parts playing an important role in particle identification and measurement. Beginning closest to the beam pipe, the inner detectors provide high precision vertexing and momentum measurements, while the calorimetry systems measure energy deposits left by traversing hadrons and electromagnetic particles. The muon system resides further out still and will identify muons, which penetrate the entire ATLAS detector. A quantity that is measured indirectly at ATLAS is the missing transverse momentum (E_T^{miss}) associated with an event. Since the energy of colliding partons in the transverse plane prior to collision sums to zero, the

E_T^{miss} in an event denotes the momentum imbalance observed after the interaction. The derivation of this quantity requires input from multiple detector systems, and so this too is discussed in the following sections. In addition to these, a sophisticated trigger and data acquisition (TDAQ) framework is required in order to filter through the enormous volume of interactions and identify the interesting events to be recorded.

2.2.1 Magnet System

The aesthetically impressive ATLAS magnet system consists of one solenoid and three toroid magnets. Powerful magnetic fields are required at ATLAS in order to bend the trajectories of charged particles so as to aid in charge identification and accurate momentum measurements. The central solenoid measures 5.8 m in length and is arranged with the beam-pipe at its centre, with an inner radius of 1.23 m. The solenoid immerses the inner detector in an axial 2 T magnetic field, and its thickness has been optimised so as to minimise the amount of material a particle must penetrate between the inner detector and the calorimeters, with a thickness of only 45 mm. In this spirit, the central solenoid and the barrel electromagnetic calorimeter share a vacuum chamber so as to avoid the unnecessary obstruction of an extra wall.

The total length of the barrel toroid is 25.3 m, with inner and outer radii of 4.7 m and 10.05 m. Two end-cap toroids are inserted within the barrel toroid, each measuring 5 m in length. Each of these toroids contain eight individual coils, which are arranged at constant radius with respect to the beam-pipe at evenly spaced intervals. The toroids provide the muon system with a magnetic field of 0.5 T (1 T) in the barrel (end-caps).

The ATLAS magnet system drives the geometry of the entire detector. The sheer size and weight of them necessitated the construction of the rest of the detector around them.

2.2.2 The Inner Detectors

With every bunch crossing at ATLAS, the number of particles emerging from the interaction region is in excess of a thousand. This results in a high density of particle tracks, all of which must be isolated and identified by the inner detector. Such a large number of particles penetrating the detector, and at such high frequency, presents a challenging environment in which precision measurements of position and momentum must be made. The ATLAS inner detector is responsible for isolating individual particle tracks and making the necessary measurements, and has been designed to handle the volume and frequency of particle bombardment experienced at ATLAS. It provides tracking information for charged particles with $p_T > 0.5$ GeV, with a coverage of $|\eta| < 2.5$. In principle this p_T threshold could be lowered, though considering lower p_T particles the time take to process different hit combinations to check for and identify tracks increases. In practice a compromise is reached between p_T and processing time, with this being reoptimised each year.

The entire inner detector resides within the central solenoid, and so is immersed in a 2 T magnetic field. The solenoidal field, pointing along the beam pipe, bends particle tracks in inverse proportion to the particle momenta. Shown in Figure 2.5, the inner detector is comprised of three main components: the pixel detector, the semi-conductor tracker (SCT) and the transition radiation tracker (TRT). The pixel detector is the innermost part of the inner detector, with the SCT and TRT positioned at larger radii from the beam pipe, as shown in Figure 2.6. Spatial and resolution specifications, in addition to coverage information on all the inner detector sub-systems, can be found in Table 2.2.

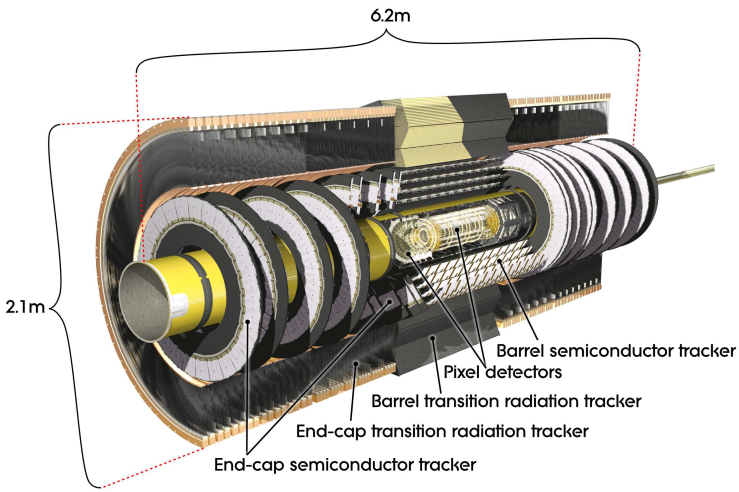

Figure 2.5: The ATLAS Inner Detector.

Pixel Detector

The pixel detector, constructed around the thin beryllium beam pipe and therefore positioned as close to the interaction region as possible, provides the most precise tracking information of the three inner detector components. It is comprised of three layers, each consisting of rectangular pieces of silicon divided into pixels. Each pixel has approximate dimensions 50 μm $\times$ 400 μm, providing the high granularity necessary for the precise position measurements desired. These silicon layers are cylindrical in the barrel and form disks in the end-caps. This setup dictates that charged particles will normally pass through three layers of pixels. Charged particles penetrating the silicon create electron-hole pairs. Due to the bias voltage across the pixel the holes drift towards the cathode. This current is then collected at the cathode and read out, denoting a "hit."

The accuracy of the pixel detector in the r–ϕ plane is 10 μm, and the high precision of position measurements allows the distinction between primary and secondary vertices near the interaction point. Containing in excess of 80 million

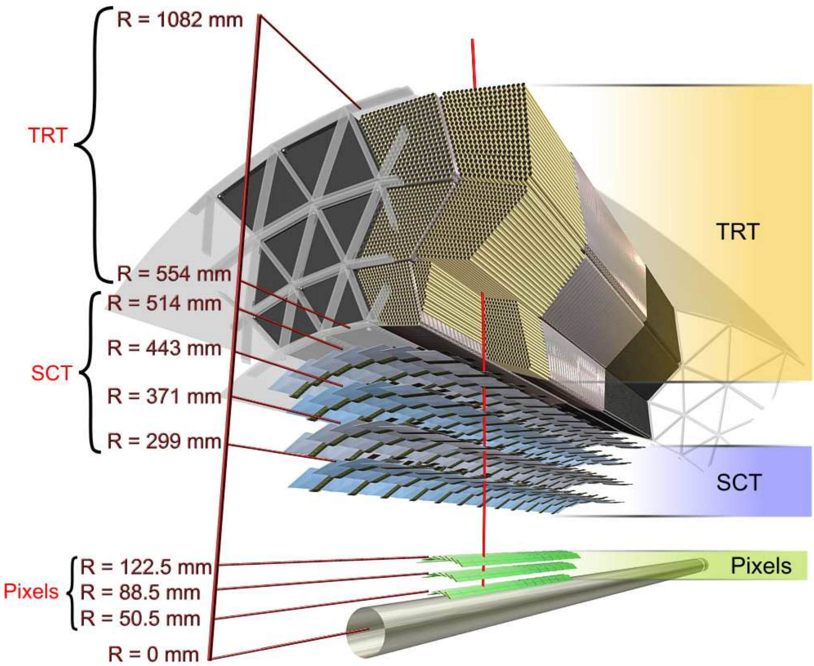

Figure 2.6: Schematic showing the three inner detector sub-systems and their respective layering and distances from the beam pipe.

pixels, no sub-system comes close to matching such a high number of read–out channels, and in fact the pixel detector alone comprises almost 90% of all the ATLAS read–out channels. Such precision is of great importance for identifying particles decaying promptly, with the decay vertices of b-quarks and τ-leptons being prime examples. At the time of construction, the engineering and design of the pixel detector, permitting such superior performance, was at the limit of current technology. The production expense was such that the pixels are used only in the most central region of the inner detector, with other lower-cost technologies being used further from the interaction region. Given the harsh radiation environment the pixels are exposed to, being so close to the interaction region, this part of the detector has a short expected lifetime at the LHC. The innermost layer is expected to suffer in performance after only 3 years of running at design luminosity, and plans for a replacement have been long underway [18].

SCT

The SCT is a cheaper alternative to the pixel detector, since the high cost of the innermost detector material prohibits its use throughout the entire ATLAS tracking system. Being positioned further away from the interaction point, the track density is lower, and so the demands on fine granularity are not as high. There are ~ 6 million read-out channels in the SCT, and it works in much the same way as the pixel detector. Four cylindrical layers of two-sided silicon micro-strip modules comprise the SCT in the barrel, where as in the end-caps the SCT is composed of nine disks. This layout dictates that a track usually passes through 8 strip layers. A module in the SCT consists of four rectangular silicon pieces with dimensions 63.6 mm $\times$ 64.0 mm. With an intrinsic accuracy of 17 μm in the r–ϕ plane, the SCT, while not sharing the elite performance of the pixel detector, still provides excellent resolution for disentangling particle tracks.

TRT

The TRT is low-cost and lightweight, consisting of polyimide "straws" of 4 mm in diameter containing gas (Xe, O_2, CO_2) and gold plated tungsten wire to act as the anode. The straws are themselves wrapped in the same kind of tungsten wire, and comprise the system's cathodes. This drift tube system identifies a hit when the gas contained therein is ionised by a penetrating particle. In the barrel region there are in total $50,000$ of these detector straws, each running parallel to the beam axis, and each with a length of 144 cm. In the end-caps, $160,000$ straws 37 cm in length are arranged radially around the beam axis. In addition to its tracking capabilities, the TRT is also able to detect and generate transition radiation. Positioned between the drift tubes is polypropylene radiator material. When relativistic particles encounter the boundary between a gas-filled straw and the polypropylene, x-rays will be emitted due to the change in dielectric constant of the traversed medium. Electrons typically emit radiation at a much lower energy compared with hadrons, and as such the TRT offers some distinction between the two.

Sub-detector	Partition	Coverage	Spatial resolution [μm]	Hits per track
Pixel	Barrel	$\lvert\eta\rvert < 2.5$	10 (r–ϕ), 115 (z)	3
	End-caps	$2.0 < \lvert\eta\rvert < 2.5$	10 (r–ϕ), 115 (z)	3
SCT	Barrel	$\lvert\eta\rvert < 1.5$	17 (r–ϕ), 580 (z)	8
	End-caps	$1.3 < \lvert\eta\rvert < 2.5$	17 (r–ϕ), 580 (z)	8
TRT	Barrel	$\lvert\eta\rvert < 1.0$	130	35
	End-caps	$0.8 < \lvert\eta\rvert < 2.0$	130	35

Table 2.2: Coverage, spatial resolution and the average number of hits per track for the inner detector sub-systems.

2.2.3 Calorimetry

The ATLAS calorimeters, shown in Figure 2.7, provide coverage over the range $|\eta| < 4.9$. In contrast to the inner detectors the calorimeters can detect neutral and charged particles. For the η range covered by the inner detectors, the granularity is very fine, allowing for particle identification and precise measurements of E_T.

The ATLAS calorimetry system is split into two sub-detectors, the electromagnetic (EM) calorimeter (ECAL) and the hadronic calorimeter (HCAL). Particles which interact primarily via the electromagnetic interaction tend to be less penetrating than strongly interacting particles. Furthermore, EM showers are generally

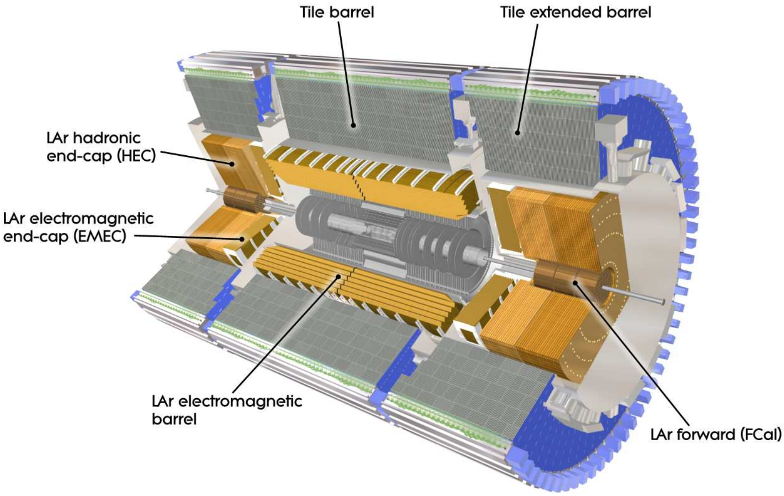

Figure 2.7: The ATLAS Calorimeters.

shorter and narrower than those due to hadrons. The EM radiation length, χ_0, which describes the energy loss of EM particles as they traverse a material, is ~ 10 times less that the nuclear interaction length, λ. As such, hadrons will penetrate the ATLAS detector to a greater depth than EM particles. It follows then, that the ECAL is the second detector sub-system particles encounter as they traverse ATLAS (if the Inner Detector is to represent the first), with the HCAL being the third.

The granularity of the HCAL is coarser than that of the ECAL due to its increased distance from the beam pipe. A complete account of the pseudorapidity coverage and granularity of all the ATLAS calorimeter systems can be found in Table 2.3. Both calorimeters are so-called "sampling" calorimeters, consisting of two types of material: one absorber to initiate showering, and one additional material to make energy measurements. By layering these two types of material it is ensured that a particle traversing the detector loses its energy in stages. The energy deposited by the particle at each stage may then be measured, permitting the calculation of the total particle energy. To measure these energy deposition, the ATLAS calorimeters use liquid argon (LAr) and scintillating tile technologies. The scintillating tiles are used in the central regions of the HCAL, and due to radiation damage the signal read-out from the tiles degrades over time. This is not the case with the LAr active medium. Since the LAr is continuously flowing and therefore being replaced, there is no lasting effect from radiation damage. For this reason LAr technology tends to be favoured in areas close to the interaction point and the very forward regions.

The energy resolution of the LAr barrel [19], end-cap and forward [20] calorimeters was measured during beam tests at the CERN SPS. Measurements were made using electron beams of $E \leq 245$ GeV ($E \leq 200$ GeV) in the case of the barrel (end-caps and forward regions). For the hadronic end-caps pion beams of $E < 200$ GeV were used at test beam [21], whereas pions of up to 350 GeV were used when determining the energy resolution of the tile barrel of the HCAL [22]. Since the energy resolution is dominated by an energy dependent term, though is also influenced by noise and other instrumental effects (which tend to be energy–independent), it is expressed as a function of the form $\frac{a}{\sqrt{E}} \oplus b$, where a and b denote the energy dependent and independent terms respectively, and the $\oplus$ indicates that the two terms are added in quadrature. The measured resolutions are:

$$\frac{\sigma_E}{E} = \frac{(10.1 \pm 0.1)\%\ \mathrm{GeV}^{1/2}}{\sqrt{E}} \oplus (0.17 \pm 0.04)\% \quad \text{(EM Barrel)},$$

$$\frac{\sigma_E}{E} = \frac{(52.7 \pm 0.9)\%\ \mathrm{GeV}^{1/2}}{\sqrt{E}} \oplus (5.7 \pm 0.2)\% \quad \text{(Hadronic Barrel)},$$

$$\frac{\sigma_E}{E} = \frac{(13.5 \pm 0.5)\%\ \mathrm{GeV}^{1/2}}{\sqrt{E}} \oplus (0.7 \pm 0.1)\% \quad \text{(EM End-caps)},$$

$$\frac{\sigma_E}{E} = \frac{(84.1 \pm 0.3)\%\ \mathrm{GeV}^{1/2}}{\sqrt{E}} \oplus (0.0 \pm 0.0)\% \quad \text{(Hadronic End-caps), and}$$

$$\frac{\sigma_E}{E} = \frac{(29.3 \pm 0.7)\%\ \mathrm{GeV}^{1/2}}{\sqrt{E}} \oplus (3.0 \pm 0.1)\% \quad \text{(Forward)}.$$

The obtained relative energy resolutions are consistent with the values expected from simulation. The Monte Carlo was found to slightly over-estimate the resolution at low energies, gaining better agreement as the energy increases. Beam tests such as these permit the energy response of detector systems to be measured upon the bombardment of single particles, which is not entirely representative of the exact conditions the calorimeters are exposed to in practice. With the LHC now in full operation, the performance of the ATLAS calorimeters is continuously monitored during data taking with proton and heavy ion beam collisions.

Electromagnetic Calorimeter

The central region of the ATLAS ECAL shares a vacuum chamber with the central solenoid magnet, and measures EM showers (and in addition any hadronic showers which may initiate before reaching the HCAL). The ECAL is comprised of a central barrel and two end-caps, with the end-caps housed in separate cryostats. The barrel is in two identical sections joined with a 4 mm gap at $z = 0$, with coverage $|\eta| < 1.475$. The end-caps are each comprised of two rings (inner and outer), the coverage of the outer disk being $1.375 < |\eta| < 2.5$ and that of the inner disk being $2.5 < |\eta| < 3.2$.

The ECAL uses a liquid argon active medium sandwiched between layers of lead absorbers. The lead induces particle showers while the LAr becomes ionised by particles in the shower. High voltage lines are used to put a potential difference across the active medium, and thus the electrons induced upon ionisation drift towards the anode. This charge is collected at the anode and read out as a current. The ECAL has been built with an accordion geometry, shown in Figure 2.8, in the barrel which has the benefit of offering total coverage in ϕ. Before particles reach the ECAL they must first penetrate the LAr pre-sampler, which is positioned on the cryostat wall. This contains only one thin layer of LAr. The function of the pre-sampler is to compensate for the energy lost by particles in the inner detector, before having reached the calorimeter system.

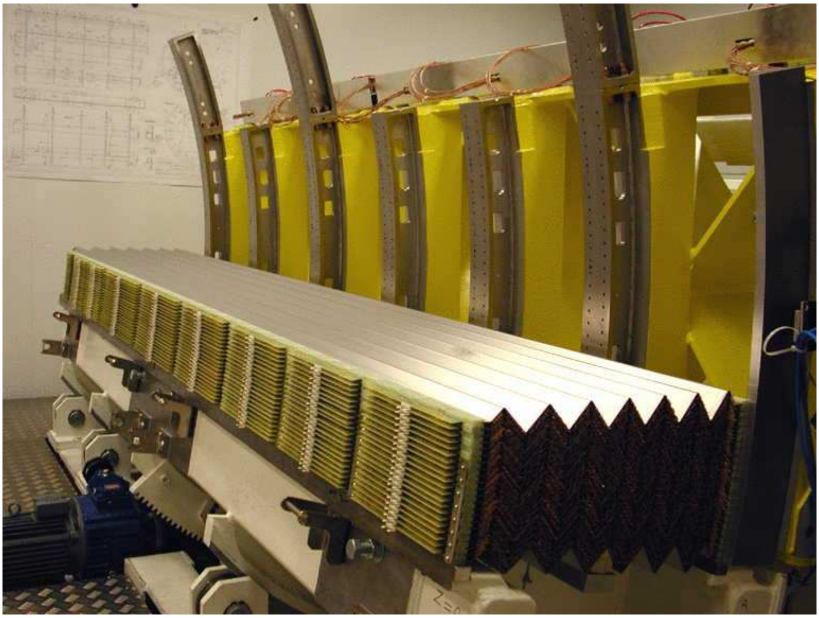

Figure 2.8: Photograph of an EM LAr module from the barrel, part–way through assembly. Here the accordion geometry utilised in the ECAL is clearly visible.

- Pre-Sampler
  Single layers of LAr active medium, making up the ATLAS EM pre-sampler, are used in the range $|\eta| < 1.8$ to correct for energy lost by electrons and photons in the detector material upstream of the calorimeters. The barrel pre-sampler (EMBPS) is fitted in front of the barrel of the EM calorimeter, on its inner surface, and measures ~ 11 mm in depth. It is divided into 64 azimuthal pre-sampler sectors in total, 32 per half barrel, with dimensions 3.1 m $\times$ 0.28 m. Each pre-sampler sector is comprised of 8 modules of different sizes. The size of the modules increases with $|\eta|$ so as to achieve an η coverage of 0.2 per module, with the exception of the module closest to the end–caps, whose coverage is reduced to 0.12.

  In the EM end-caps (EMEC) the pre-sampler (EMEC0A/C) consists of only ~ 5 mm of LAr active medium and covers the range $1.5 < |\eta| < 1.8$. Each end-cap contains 32 PS modules.

- Barrel
  The EMB has total coverage in ϕ and covers $|\eta| < 1.475$. The full coverage in ϕ is achieved with the accordion geometry of the barrel calorimeter (this accordion layout is also used in the EM end-caps). It is constructed of two half-barrels, the EMBA (the A-side barrel) and EMBC (the C-side barrel),

each measuring 3.2 m in length. Each half-barrel contains 1024 accordion shaped lead absorbers designed to induce electromagnetic showers. The read-out electrodes are positioned within the gaps, with the absorber-electrode spacing measuring 2.1 mm throughout the accordion layers. In this way, the waves of the accordion shape in the barrel extend outwards from the beam pipe, with the angle between waves increasing such that the 2.1 mm gap remains constant.

The electrodes themselves are copper etched onto polyimide, a substance known for being strong, flexible, lightweight, thermally stable and resistant to chemicals. The high-voltage (HV) is distributed over the outer surface of the electrodes on the front and back of the polyimide structure. There is, in addition, a separate conductive layer between the two outer surfaces which collects any signal reaching the electrodes via capacitive coupling. On applying a voltage of 2 kV (nominal operating voltage) between the electrodes any charge induced upon ionisation of the LAr active medium drifts towards the electrodes. At this 2.1 mm separation, the drift time for these charges is 450 ns.

Each half–barrel is divided into 16 modules, and each EMB module has three layers. The front layer, sampling 1 (EMB1A/C), has the finest granularity ($\eta \times \phi = 0.003 \times 0.1$) due to its proximity to the interaction region. The middle layer, sampling 2 (EMB2A/C), has coarser granularity ($\eta \times \phi = 0.025 \times 0.0245$) and covers the greatest distance in r. It is here that much of the energy deposits are gathered from EM showers. The back layer, sampling 3 (EMB3A/C), has the coarsest granularity ($\eta \times \phi = 0.05 \times 0.0245$) and is furthest away from the interaction region. A diagram of an example barrel module is shown in Figure 2.9. Here the different layers can be seen, with the η–ϕ dimensions of the cells in each clearly displayed. Also shown is the granularity of a trigger tower. In total the EMB contains 3424 read-out cells (including the PS) per module.

- End-caps

  The EMEC covers the range $1.375 < |\eta| < 3.2$ and consists of two identical wheels, one on each side of the EMB. Each wheel itself consists of two coaxial wheels, an inner wheel ($2.5 < |\eta| < 3.2$) and an outer wheel ($1.375 < |\eta| < 2.5$). As is the case in the barrel, each end-cap is split into three layers (or "samplings") in the region $1.5 < |\eta| < 2.5$, but only two in the region $2.5 < |\eta| < 3.2$. The front layer (EMEC1A/C) is the strip layer, so–called as the read–out structure has fine granularity in $\Delta\eta$ of 0.003 with comparably larger granularity in $\Delta\phi$ of 0.1. The middle layer (EMEC2A/C) is coarser with a granularity of 0.025×0.0245 in η–ϕ, and the back layer (EMEC3A/C) being coarser still. Both the inner and outer wheels of the EMEC are split into eight segments. The accordion geometry once again guarantees complete coverage in ϕ, with the size of the drift gap varying between 0.9–3.1 mm.

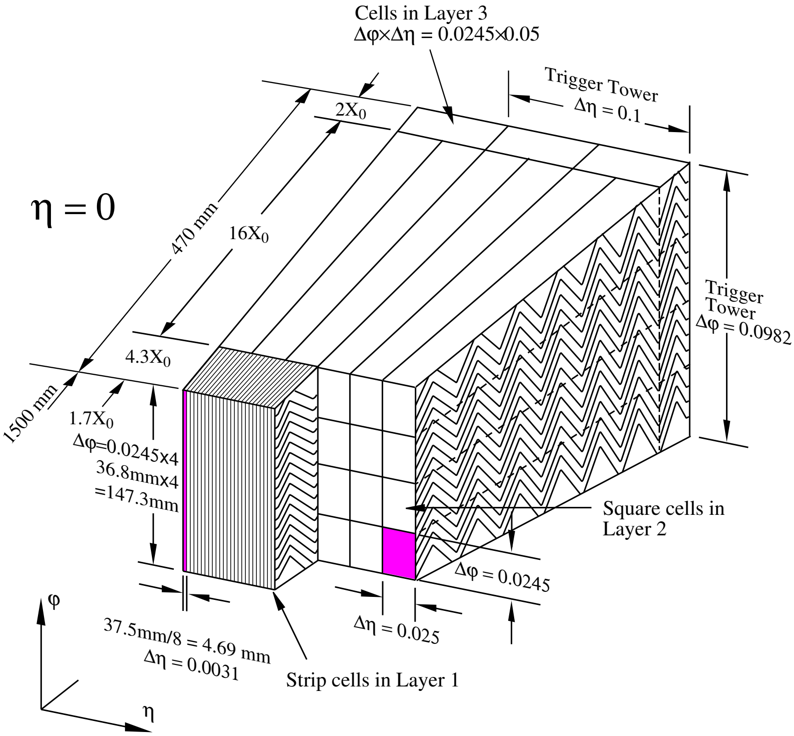

Figure 2.9: An example EM barrel module, showing the difference in cell dimensions in layers 1, 2 and 3, along with the trigger tower granularity.

The resolution of the ATLAS ECAL partition samplings for various particle energies was studied and measured upon exposure to electron, photon and pion beams. The η resolution of the front and middle layers of the EMB and EMEC for different beam energies were fit with a function of the form $c_1 \oplus \frac{c_2}{\sqrt{E}} \oplus \frac{c_3}{E}$, with the results found to be as follows [23]:

$$\sigma(E) = (0.40 \pm 0.88) \times 10^{-4} \oplus \frac{(1.91\pm0.22)\times10^{-3}\ \text{GeV}^{1/2}}{\sqrt{E}} \oplus \frac{(1.03\pm0.13)\times10^{-2}\ \text{GeV}}{E} \quad \text{(EMB1)}$$

$$\sigma(E) = (1.20 \pm 0.50) \times 10^{-4} \oplus \frac{(5.05\pm0.20)\times10^{-3}\ \text{GeV}^{1/2}}{\sqrt{E}} \oplus \frac{(0.65\pm1.14)\times10^{-2}\ \text{GeV}}{E} \quad \text{(EMB2)}$$

$$\sigma(E) = (0.43 \pm 0.16) \times 10^{-4} \oplus \frac{(0.17\pm0.03)\times10^{-2}\ \text{GeV}^{1/2}}{\sqrt{E}} \oplus \frac{(0.17\pm0.23)\times10^{-4}\ \text{GeV}}{E} \quad \text{(EMEC1)}$$

$$\sigma(E) = (0.19 \pm 0.03) \times 10^{-3} \oplus \frac{(0.27\pm0.03)\times10^{-2}\ \text{GeV}^{1/2}}{\sqrt{E}} \oplus \frac{(1.15\pm0.10)\times10^{-2}\ \text{GeV}}{E} \quad \text{(EMEC2)}$$

Hadronic Calorimeter

The hadronic calorimeter covers the range $|\eta| < 4.9$. With such a large η coverage, the radiation environment and typical particle trajectories confronting the calorimeter varies widely. As such the HCAL uses different materials and technologies depending on the varying demands over the full range in η. In the barrel the tile calorimeter (TileCal) uses steel absorbers paired with scintillating tiles to detect hadronic showers. In the end-caps and forward regions LAr technology is used to cope with the increasingly harsh radiation environment.

An important requirement for the HCAL, in addition to the obvious demands on hadronic energy measurements and resolution, is the ability to sufficiently contain hadronic showers. It's thickness must, therefore, be adequate to reduce as much as possible any "punch-through" from the HCAL to the muon system. In the most central region, the HCAL is 11 interaction lengths (λ) thick, which has been shown in both simulation and test measurements [24] to suppress punch-through from high–momentum hadronic particle jets into the muon system. Such containment coupled with the large η coverage also ensures the ability to provide a good measurement of the missing momentum (E_T^{miss}) in an event. This feature is especially important in SUSY searches, where "invisible" LSPs traverse the entire ATLAS detector without interacting with the detector material.

- Tile Calorimeter
  Covering the central region, the tile calorimeter is placed outside of the EMB and the central solenoid magnet, and extends in radius from $\sim$ 2.28 m to $\sim$ 4.25 m. The tile system consists of a main barrel (of length 5.8 m) covering the range $|\eta| < 1.0$ and two extended barrels covering $0.8 < |\eta| < 1.7$ (of length 2.6 m). Each of these sections consist of 64 modules, split in ϕ, and have three layers at different radii similarly to the ECAL. Since the tile calorimeter is also a sampling calorimeter, alternating layers of absorber (steel) and active medium (scintillator tiles) are the basis of construction. Scintillator tiles, approximately 3 mm in thickness, are arranged radially along the beam pipe with the tile face along the z-axis, with steel absorbers sandwiched between the tiles in this orientation. The granularity of the tile barrel is approximately $\Delta\eta \times \Delta\phi = 0.1 \times 0.1$, with $\Delta\eta$ increasing to 0.2 in the back layer. The scintillation light induced in a tile upon the passage of radiation is read-out on each side of the tile through optical fibres, and transmitted to two separate photo-multiplier tubes (PMTs), one for each side of the read-out.

- Hadronic End-caps
  The hadronic end-caps (HEC) cover the region $1.5 < |\eta| < 3.2$ and reside in the end-cap cryostats along with the EMEC and forward calorimeters (FCAL). This means that the HEC overlaps slightly with the forward calorimeter as well as with the EMEC, with an aim to minimise the detector material in the transition region between calorimeter partitions. The HEC is constructed in two wheels per end-cap, with each wheel consisting of two layers, resulting in four layers per end-cap in total. Each HEC wheel is split into 32 modules segmented in ϕ, with layers of copper absorber and LAr active material orientated normal to the beam line. In the front wheel there are 24 copper absorbers per module, each 25 mm thick, and held at a plate-plate spacing of 8.5 mm. In the rear wheel there are fewer plates, 16 in total, each being 50 mm thick. One extra copper plate is placed at the very front of each of the front and rear wheels, measuring 12.5 mm and 25 mm in thickness

respectively. Within the 8.5 mm gap, three electrodes divide the LAr active medium into four layers of 1.8 mm. The central of these three electrodes acts as the read-out, with the two either side carrying HV. This layout, shown in Figure 2.10, results in an electrostatic transformer (EST). This means that the two 1.8 mm LAr layers behave like a single 3.6 mm gap, but the operating voltage can be lower. In addition the ion density at the LAr-electrode boundaries, and the ion drift time, can be kept lower than for the case of a single large gap. The nominal HV for the HEC is $\sim$ 1800 V and at this voltage the drift time for ions in the LAr gaps is approximately 430 ns.

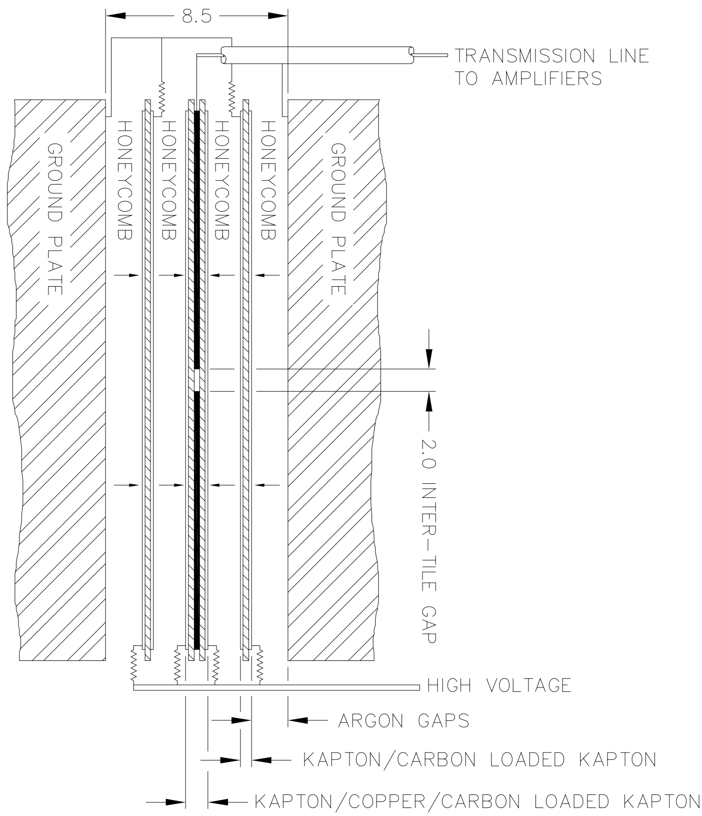

Figure 2.10: Schematic showing the layout of the HEC read–out structure in the 8.5 mm LAr gaps. All dimensions quoted are given in mm.

- Forward Calorimeters

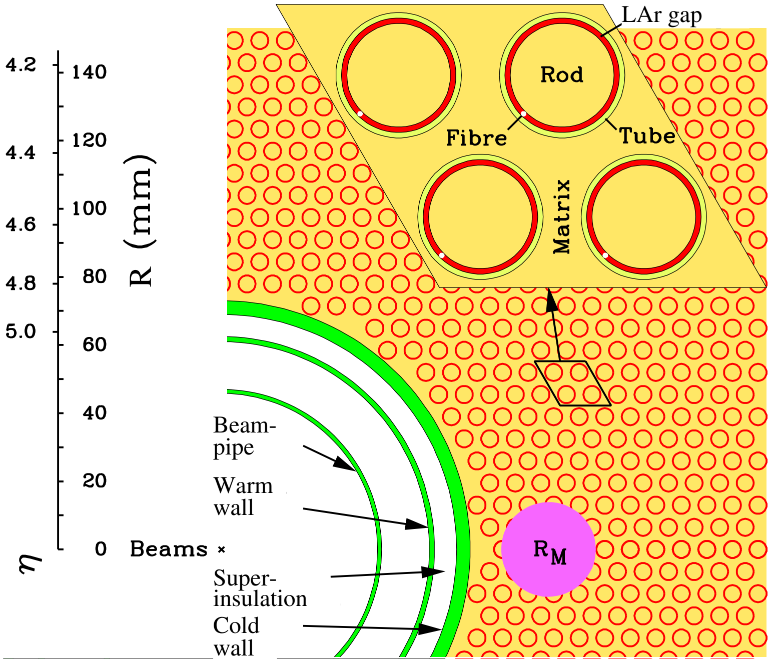

Figure 2.11: Schematic of the electrode structure in an FCAL1 module.

The LAr FCAL consists of two independent sections, one in each end-cap cryostat, placed upstream in $|\eta|$ from the HEC. An overview of the arrangement of the partitions occupying the end–caps is given in Figure 2.12. Overlapping slightly with the HEC, the FCAL covers an η range of $3.1 < |\eta| < 4.9$. At these high η values the FCAL is exposed to a high flux of particles, and the structure of the FCAL has been optimised accordingly. The three FCAL layers are each 45 cm in depth, the first module (FCAL1) being dedicated to EM particle reconstruction (so in fact this comprises part of the ECAL system), with the outer two layers (FCAL2/3) being the hadronic modules. The FCAL uses LAr active medium, with absorbers of copper in FCAL1 and tungsten in FCAL2 and FCAL3. The layout of the absorber-sampling layers is somewhat different from the geometry used elsewhere in the calorimeter system, and is shown in some detail in Figure 2.11. For FCAL1, the copper absober plates are packed together normal to the beam line, with a total of $12,260$ holes drilled at regularly spaced intervals parallel to the z-axis. Within these holes, central copper electrodes provide the read-out for each channel, with these central rods being maintained at a positive high voltage. The outer copper tubes, which contain the electrodes at their centre, are kept at ground and the LAr gaps between these structures are maintained at $\sim 250\ \mu$m by fibrous spacers, as shown in Figure 2.11. Such small gap sizes are required to cope with such a high density of particle interactions, and avoid ion build up in the LAr. For FCAL layers 2 and 3, two copper end-plates of 2.35 cm are placed either end of the modules, which contain a tungsten matrix with the same tube-electrode structure. The main difference here is that the use of tungsten for the tubes and read-out rods, with a LAr gap of 375 μm. This layout provides a high density detector medium to contain energetic particles at high η, and short drift times to avoid charge build up.

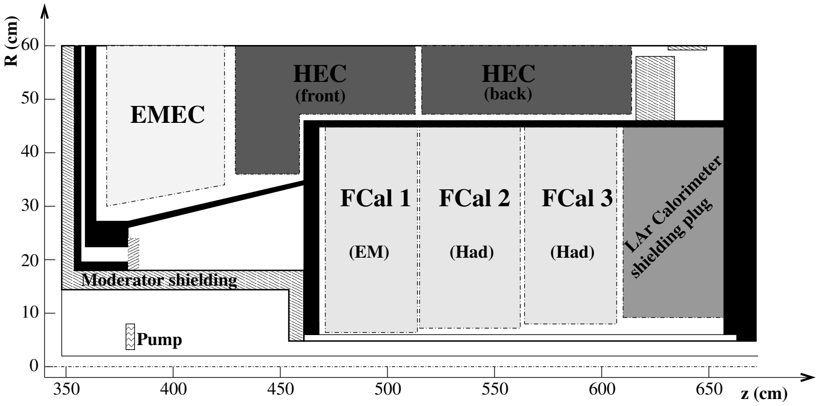

Figure 2.12: Diagram showing the arrangement of the EMEC, HEC and FCAL modules located in the end–cap cryostats.

LAr Electronics and Read-out

Most of the calorimeter includes LAr as the active medium, and as such the LAr calorimeter system accounts for the majority of the ATLAS calorimeter complex. Signal collected at the electrodes for each cell is read-out from each channel at a rate of up to 40 MHz annd temporarily stored in a switched capacitor array pending a trigger decision. The energy is summed in trigger towers of 0.1×0.1 in η–ϕ before being used as input to the Level 1 trigger. A schematic of the LAr read–out electronics is shown in Figure 2.13. The signal read-out goes through several stages, beginning with the electronics within the cryostats. In the EMB (outer EMEC wheel) the read-out electrodes are connected to summing boards, which sum the signal over 16 (12) electrodes. This corresponds to $\Delta\phi = 0.1$ for layer 1, while layers 2 and 3 in the EMB have summing boards for groups of four adjacent calorimeter cells, each corresponding to a region of $\Delta\phi = 0.025$. In the inner wheel of the EMEC one summing board serves eight electrodes, with four adjacent electrodes comprising a single read-out cell, resulting in a cell read-out coverage of $\Delta\phi = 0.1$.

The output from the summing boards is fed to mother boards, still within the cryostat, where the signal is sent to the read-out cables. These read-out cables leave the cryostat through cold-to-warm feedthoughs, which take the output from the cryostats between the barrel and extended barrel TileCal (EMB) or around the back of the end-caps (EMEC, HEC, FCAL) to the front-end crates (FECs). The 58 FECs are located in boxes attached to their respective feedthroughs in the gaps between the barrel and extended barrel or behind the end-caps and form part of the "on-detector" electronics. The FECs contain the calibration boards, which are used to calibrate the calorimeter energy response. This is done by injecting a current pulse at a precisely known value to simulate the effect of a real energy deposit

Table 2.3: Pseudorapidity coverage and granularity for each partition layer of the ATLAS calorimeter system.

Partition	Layer	Coverage	Granularity ($\Delta\eta \times \Delta\phi$)
EMB	PS	$\|\eta\| < 1.52$	0.025×0.1
	1	$\|\eta\| < 1.475$	0.003×0.1
	2	$\|\eta\| < 1.475$	0.025×0.025
	3	$\|\eta\| < 1.475$	0.05×0.025
EMEC	0	$1.5 < \|\eta\| < 1.8$	0.025×0.1
	1	$1.375 < \|\eta\| < 1.5$	0.025×0.1
		$1.5 < \|\eta\| < 1.8$	0.003×0.1
		$1.8 < \|\eta\| < 2.0$	0.004×0.1
		$2.0 < \|\eta\| < 2.5$	0.006×0.1
		$2.5 < \|\eta\| < 3.2$	0.1×0.1
	2	$1.375 < \|\eta\| < 2.5$	0.025×0.025
		$2.5 < \|\eta\| < 3.2$	0.1×0.1
	3	$1.5 < \|\eta\| < 2.5$	0.05×0.025
Tile Barrel	1	$\|\eta\| < 1.0$	0.1×0.1
	2	$\|\eta\| < 1.0$	0.1×0.1
	3	$\|\eta\| < 1.0$	0.2×0.1
Tile Extended Barrel	1	$0.8 < \|\eta\| < 1.7$	0.1×0.1
	2	$0.8 < \|\eta\| < 1.7$	0.1×0.1
	3	$0.8 < \|\eta\| < 1.7$	0.2×0.1
HEC	0/1/2/3	$1.5 < \|\eta\| < 2.5$	0.1×0.1
		$2.5 < \|\eta\| < 3.2$	0.2×0.2
FCAL	1/2/3	$3.1 < \|\eta\| < 4.9$	0.2×0.2

in the calorimeter cells. The results of these calibrations are vital in maintaining up-to-date values for energy reconstruction.

Also on the FECs, the front-end boards (FEBs) amplify the signal via a preamplifier, before feeding it through shapers which take samples at 25 ns intervals. Each FEB serves up to 128 calorimeter cells. The energy read-out from a single cell can range from 10 MeV - 3 TeV, and in order to ensure coverage of this full dynamic range the cell signal is read-out over three ranges. For each input signal the shapers produce three outputs with the relative gains of approximately 1/10/100 (low/medium/high gain). These signals are then aligned according to pulse time, and summed to form the trigger tower signals, on the tower builder boards (TBBs). This is the final preparation stage before feeding the trigger tower information to the level 1 trigger interface. In parallel with this step, following the shaping, the analogue signals are stored in memory on the FEB. If the level 1 trigger decision is to store this information, the memorised signals on the FEBs are sampled at 5 intervals (32 for calibrations) and digitised using 12 bit analogue-to-digital converters (ADCs) before being sent to the "off-detector," or "back-end," electronics.

Each FEC is connected to a read-out driver crate (ROC), which houses the read-out drivers (RODs). The RODs receive the raw signal from the FEBs and convert the signal into the relevant time and energy measurements, in addition to determining the quality of the signal itself. An optimal filtering (OF) method calculates the energy deposition from each cell while minimising the contribution from electronic pile-up noise. This is done using optimal filtering weights evaluated upon this minimisation, in conjunction with known calibration constants.

The signal energy is determined using the 5 (32) samples taken for physics (calibration) runs. The time of the signal pulse relative to the first sample, τ, can also be determined, but with an associated uncertainty inversely proportional to energy, this quantity is only calculated for cells with energy values above a certain threshold to keep the errors within a reasonable range. In general this threshold will reject up to 90% of cells, leaving no more than 10% for which the full calculations are made.

$$E_{cell} = \sum_{i=1}^{N} a_i(s_i - ped) \tag{2.6}$$

$$E_{cell}\tau = \sum_{i=1}^{N} b_i(s_i - ped) \tag{2.7}$$

Here N is the number of samples, s is the amplitude of the sample in ADC counts and, *ped* is the pedestal value for the cell in question. The pedestal is the constant residual background in the read-out cells and is measured during pedestal calibration runs and subtracted from each read-out sample, s_i, before energy calculation. The electronic noise in a cell is given by the R.M.S. of the pedestal. The a_i and b_i are the optimal filtering weights. These coefficients are taken from calibration runs carried out between LHC fills and are updated approximately once a week.

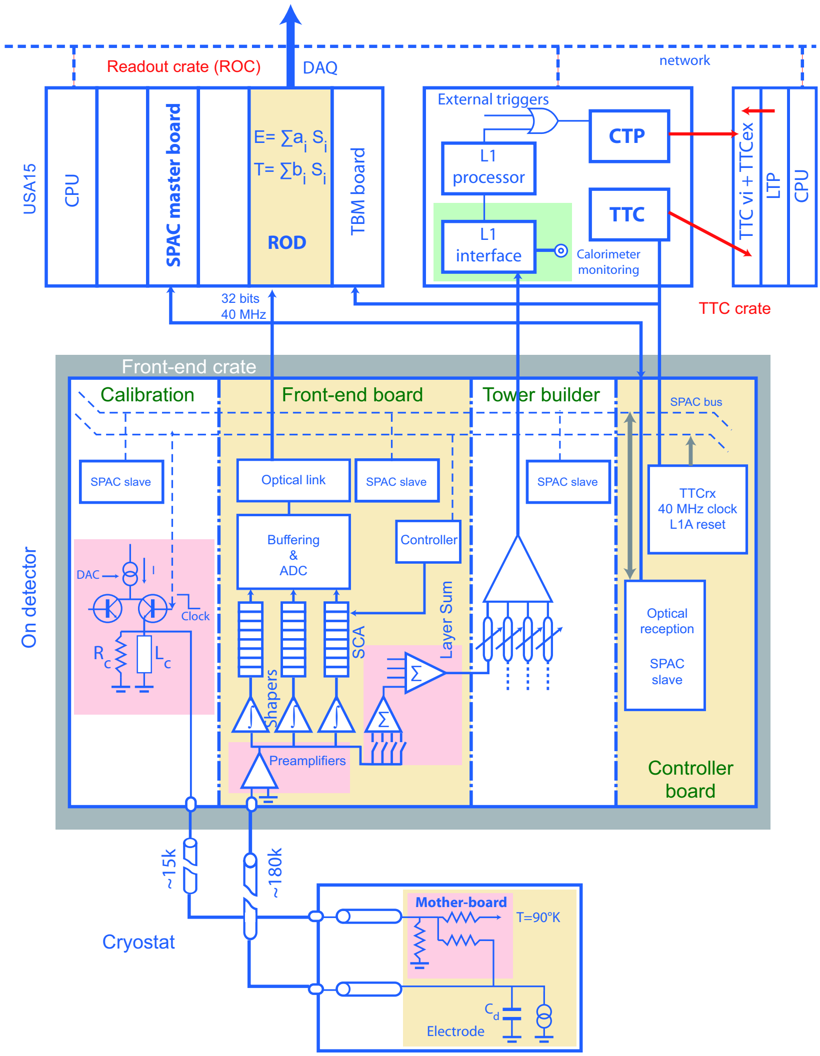

Figure 2.13: Schematic of the read–out electronics for the Liquid Argon Calorimeter. The cold on–detector electronics are shown at the bottom of the diagram, with the front–end crate just above. The read–out crate is shown in the top left of the figure. The tower builder electronics can also be seen at the top, and their associations with the L1 trigger system.

The quality of the read-out is quantified by comparing the shape of the read-out signal with the predicted shape of the pulse. The predicted pulse shape is estimated using calibration pulses in addition to the various parameters associated with the read-out electronics. The so-called quality factor (q-factor) describes the extent to which the measured pulse deviates from the predicted shape.

$$Q = \sum_{i=1}^{N} (s_i - ped - E_{cell}(g_i - \tau g'_i))^2 \tag{2.8}$$

In the above equation the g_i term represents the normalised predicted pulse shape. Following these calculations the information is sent to the ATLAS data acquisition system (DAQ). The cell energy calculated by equation 2.6 is the energy deposited in the active medium of the respective cell. In order to extrapolate this to the original particle energy, the fraction of the detector in which the signal was actually measured must be taken into account. This so-called "sampling fraction" varies over the η range due to the changing structure of the detector. Once the energy, E_{cell} is scaled according to the relevant sampling fraction, and the digital pulse has been converted from ADC counts back to an analogue signal, the energy output is at the "EM scale." This is the energy scale appropriate for measuring electrons and photons. For hadrons the calibration is more complex due to the non-compensating nature of the ATLAS calorimeters. The average fractional energy deposited by an electron or photon in the active calorimeter layers tends to be greater than the portion of energy deposited by a hadron. The energy of hadrons at ATLAS must therefore be corrected to account for this feature, and the way in which this step is performed is described in Section 4.1.3.

2.2.4 Muon System

The muon spectrometer, shown in Figure 2.14, is the largest of the ATLAS sub-detectors. It is built both in and around the toroid magnets which surround the calorimeters. Muons are highly penetrating and are the only particles (with the obvious exception of "invisible," weakly interacting particles) that reach the muon system.

The muon system was designed with the knowledge that it would be exposed to challenging background conditions. Collision products undergoing secondary interactions in the detector, shielding or surrounding machine result in a large amount of particles, mainly photons and neutrons with energy of order $\sim$ 1 MeV, penetrating the muon system. With this in mind, the muons spectrometer meets the requirements of radiation hardness, adequate granularity for tracking and the ability to cope with high rates of particle flux. Cosmic ray event data was used to measure the muon reconstruction efficiency and the momentum resolution of the muon spectrometer [25]. For muons with transverse momenta up to 400 GeV, the p_T resolution was measured to be:

$$\frac{\sigma_{p_T}}{p_T} = \frac{0.29 \text{ GeV}}{p_T} \oplus 0.043 \oplus 4.1 \times 10^{-4} \text{ GeV}^{-1} \times p_T.$$

The toroid magnets provide the end-cap regions with a magnetic field of 1 T and the central regions with 0.5 T. The muon system also includes a separate trigger designed to identify high energy muon events, which are interesting for new physics searches. The trigger covers $|\eta| < 2.4$, with the full range of the muon system being $|\eta| < 2.7$. In the barrel the muon system forms three concentric cylinders

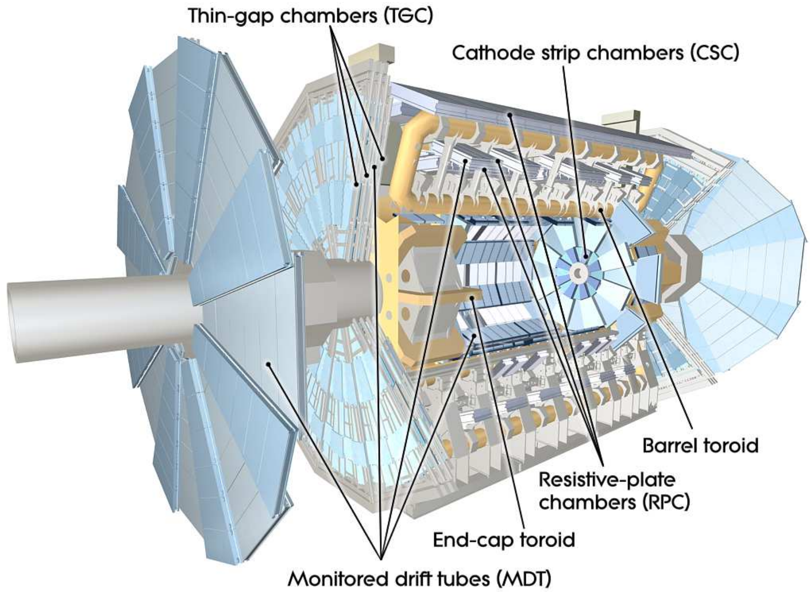

Figure 2.14: The ATLAS Muon System.

surrounding the calorimeters at radii of 5 m, 7.5 m and 10 m. Wheels are placed at distances of approximately 7.4 m, 10.8 m, 14 m and 21.5 m from the interaction point, constituting the muon system in the end-caps. Four different technologies are incorporated into the muon system to fulfil the triggering and precision physics requirements. The "monitored drift tubes" (MDTs) and "cathode strip chambers" (CSCs) provide precision energy measurements and tracking, whereas the "resistive plate chambers" (RPCs) and "thin gap chambers" (TGCs) constitute the trigger chambers. A particular challenge for the muon trigger system is the ability to maintain a stable p_T resolution for the full $|\eta| < 2.4$. The extent of this challenge stems from the fact that the momentum, p, of a muon of a given p_T increases with η. This places increased granularity requirements on the more forward regions in order to match the resolution in the barrel, and as such different technologies are used in the barrel and end-cap region of the muon system so as to meet the custom needs.

MDTs

The MDTs are aluminium tubes, of diameter ~ 30 mm, filled with gas (Ar, CO_2) with tungsten wires immersed within. Penetrating muons will ionise the gas, with the resulting electrons collecting on the tungsten. These are used in both the barrel and the end-caps to provide precision position and momentum measurements for the full $|\eta| < 2.7$ range of the muon system. The size and spacing of the MDT chambers increases with distance, r, from the beam pipe. A typical MDT chamber consists of two "multi-layers" of drift tubes, which are separated by spacer bars made of aluminium. In the inner barrel layer each of these multi-layers contains four layers of tubes, with only three comprising the layers in the middle and outer portions of the muon system. With this configuration, a muon traversing the MDTs will on average pass through 20 individual tubes.

CSCs

The safe operational counting rate per unit area for the MDTs is exceeded in the forward regions of the muon system. Cathode strip chambers, with a quicker response time and double the resolution, are used in this region. The CSCs cover the range $2.0 > |\eta| > 2.7$ and are used in the innermost part of the muon system in the end-caps. They are multi-wire proportional chambers containing multiple closely spaced anode wires surrounded by gas (Ar, CO_2, CF_4), with cathode strips running perpendicular to the wires. This orthogonal layout allows the charge distribution to be measured in both directions normal to the beam axis. The CSC system itself is segmented in ϕ, resulting in eight chambers in each of the two disks. With four CSC layers in each chamber, the average number of measurements per track is considerably less than in the MDTs.

RPCs

The RPCs make up the barrel part ($|\eta| < 1.05$) of the dedicated trigger system. Two resistive plates are separated by 2 mm of gas ($C_2H_2F_4$, Iso-C_4H_{10}, SF_6), which may be ionised by a muon passing through, causing a cascade of electrons at the anode. These chambers are made simpler in construction due to the absence of any wires within, and this feature also makes them less sensitive to any small deviations in positioning (eg. wire sag). There are three cylindrical trigger layers in the barrel, and each layer contains two RPCs. As such, a muon in the barrel will deliver six hits in the RPCs. The RPCs are able to provide adequate triggering for the barrel region.

TGCs

In addition to the increased demands on granularity, the forward region suffers from radiation levels up to 10 times those in central regions. This further complicates the already challenging environment in the end-caps. The TGCs are used to trigger on muon tracks in the end-caps ($1.05 < |\eta| < 2.4$). They are multi-wire proportional chambers working similarly to the CSCs, but in this case in order to satisfy the higher granularity requirements the gap between the wire and cathode is smaller than the wire-wire spacing. They exist in two concentric rings, one inner ring containing two TGC layers and one outer ring containing seven. These layers are segmented radially, are tailored to provide excellent time resolution and are able to cope with high particle flux rates. Both the TGCs and RPCs are designed to deliver signals over a time spread of less than 25 ns. This way the bunch crossing responsible for the muon triggering the chamber can be identified with an efficiency of $> 99\%$.

2.2.5 Luminosity Measurement

Luminosity is monitored in ATLAS with two separate systems. The first of these in the so-called “beam conditions monitor” (BCM), which is attached to the pixel detector. Four diamond sensors are positioned in around the beam pipe in a cross pattern on each side of the iteraction point. This makes two horizontal and two vertical BCM detector pairs, denoted BCMH and BCMV. BCMH and BCMV are read-out separately, and so provide two independent luminosity measurements. The BCM has a fast response time and time resolution, with a typical pulse length of 3 ns. As a result the BCM is capable of delivering bunch-by-bunch luminosity measurements, and is also able to distinguish between particles arriving along the beam line and those originating from the collision point. In fact the primary task of the BCM is to monitor the beam background levels and take action in the event of beam incidents. If the beam becomes unstable beam loss could result in a dangerous influx of particles being directed towards the ATLAS detector. In the case of such an incident the BCM would issue a beam dump request, with the beam subsequently being expelled from the LHC ring. The BCM is the only detector sub-system capable of automatically triggering beam dump.

The other detector at ATLAS responsible for luminosity monitoring is LUCID (LUminosity measurement using Cherenkov Integrating Detector). This Cherenkov detector covers the range $5.6 < |\eta| < 6.0$ and consists of sixteen aluminium tubes filled with C_4F_{10} gas on each side of the detector. As a charged particle traveses the gas filled medium the emitted Cherenkov radiaton is collected and travels to a PMT at the base of the tube. The collected radiation is used to calculate the luminosity.

2.2.6 Trigger and Data Acquisition

With collisions occurring at ATLAS at a maximum rate of 40 MHz, a great deal of information is being read-out from the detector. Even when not operating at design luminosity, ATLAS would need to read-out and record terabytes of data every second if events were not required to pass some prerequisites. It is impossible to store all the information of every single event, but with a bunch-crossing every 25 or even 50 ns, a sophisticated system is required to make the time-critical decision on whether or not to record an event. This is where the ATLAS trigger comes in. The trigger and data acquisition system (TDAQ) is responsible for deciding which events are interesting enough to keep, based on predetermined selection criteria.

The trigger chain has three main levels. The level 1 (L1) trigger uses input from a sub-set of the detector systems to isolate events worthy of further investigation. At this early stage the trigger will search for events containing high p_T muons, electrons and photons, as well as jets and tau leptons which decay hadronically. In the case of early muon identification the RPCs and TGCs are the only components of the muon system to contribute to the trigger decision at L1. Electrons and photons in the ECAL are identified using reduced granularity information in addition to isolation information, with this also being the case for jets and taus in the HCAL. A trigger decision based on the missing transverse (E_T^{miss}) and total (uncalibrated) energy in an event is also possible at L1, with the calculation being made upon summing over the calorimeter trigger towers. ATLAS also makes trigger decisions according to the p_T sum of all jets in the event, a quantity called H_T.

At design operation, bunch–crossings occur every 25 ns at ATLAS. It is vital that the L1 trigger is able to identify each bunch–crossing of interest, and with such high bunch-crossing rates this is not trivial. The task is made more challenging by the fact that the pulse shapes in the calorimeters are well over 25 ns in duration, and can extend over several bunch-crossings. Additionally, the time-of-flight between an interesting collision and produced muons triggering the RPCs/TGCs can also be comparable to or in excess of this interval. Finally, the maximum rate at which the front-end electronics can process information from the triggers is 75 kHz. The L1 trigger has therefore been designed to reach a decision on each event within 2.5 ns, with the verdicts being delivered to the FEBs at a rate within this constraint.

If an event is selected at L1 all of the detector information from the bunch-crossing in question is read-out from the front-end electronics and stored on the ROBs. It is here where the so-called "event building" takes place. All of the fragmented information stored on separate FECs on the detector are now gathered to build a picture of the events. At this stage this information is scrutinised by the next step in the ATLAS trigger system, the level 2 (L2) trigger. The L2 trigger uses regions of interest (RoI) passed on from L1. These are the regions where L1 identified high-p_T objects, driving the decision for front-end read-out. The L2 trigger scans over the regions in question and accesses all the event information from the relevant ROBs in order to make its decision. In this way only a small fraction of information need be transferred from the ROBs to L2 for this stage of the TDAQ process, preventing unnecessary mass information transfer. This is to ensure that decisions can be made quickly, since information is being collected at such a high rate.

The output rate of L2 compared with L1 is much lower, with the typical rate being ~ 1 kHz. Whereas the L1 rates were constrained by the limitations of the on-detector electronics, the 1 kHz rate is not a limit set in stone and is constantly being studied, optimised, and altered depending on physics needs. The rate is reduced by applying "pre-scales" to the data. This means that only a certain percentage of events passing the given trigger selection will actually pass at L2. A pre-scale value of 0.1, for example, implies that only 10% of events passing the given trigger requirement will in fact be passed from L2. One result of this is that physics analyses tend to choose to use un-pre-scaled triggers, or at least triggers which are not subject to extreme pre-scales, since the pre-scale needs to be taken into account upon analysis. At L2 the p_T thresholds on objects are generally tighter, and the full granularity of the calorimeters are now available to use. In addition, the ID information is made available permitting calorimeter deposit-track matching.

The final level of the trigger is called the event filter (EF). Here, the final selection is made before physics events are written to disk, where they await further scrutiny in offline data quality and integrity checks. The EF will first re-check everything that was concluded at L2 using more sophisticated algorithms, along with up-to-date calibration and detector information. This corresponds to a more thorough determination of important quantities, given the increased time the EF has to process events compared with L2. By the time data has been dealt with by the EF the output rate should have reached $\mathcal{O}(100)$ Hz, corresponding to approximately $\mathcal{O}(100)$ MB/s being written to disk. The output rate is limited by the capacity of the on–site data–processing centre, known as Tier 0. Here the reconstruction takes place and there is a finite rate at which the data can be processed. In fact in 2012 there have been some so–called "delayed" trigger streams introduced. For these streams the output from the EF is written to disk and stored, rather than being sent directly to be processed at Tier 0. This data will be kept on disk until the LHC machine technical shutdown, scheduled to begin in March 2013. Once data–taking stops, the data–processing infrastructure at Tier 0 will be free to process the data collected in the delayed trigger streams. In this way ATLAS will continue to recover new events even during the LHC machine shutdown. These streams record information output from the EF but the data is not sent on for reconstruction. In this way the data recorded in these streams are not subject to the same strict limit on output rates. The information output in these streams is to be stored until the technical stop in 2013, and will then be processed. The trigger rates at ATLAS for an example run at a luminosity of 3.2×10^{33} cm^{-2}s^{-1} are shown in Figure 2.15.

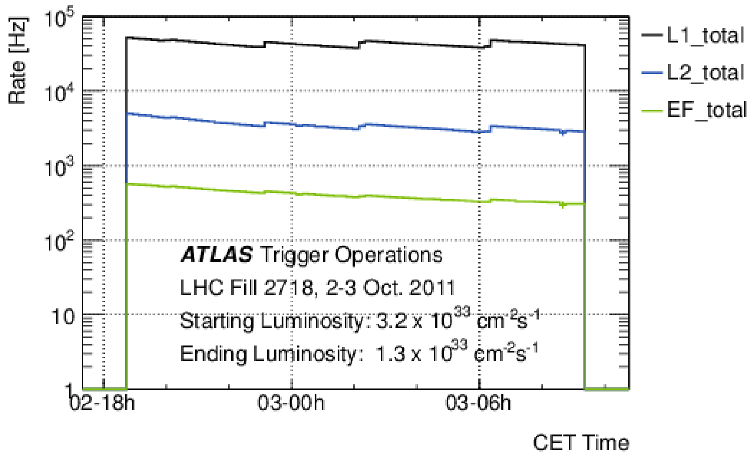

Figure 2.15: Data trigger rate at ATLAS for L1, L2 and EF at a luminosity of 3.2×10^{33} cm^{-2}s^{-1} during the 2011 proton–proton data taking [17].

After being output from the EF, events are categorised into various data "streams" depending on their characteristics. For example, events firing the electron triggers are placed in the "Egamma" stream, with events which triggered the muon system being placed in the "Muons" stream. In addition to the physics streams there are also calibration streams, which contain events triggering on empty bunch-crossings. These can be used for calibration purposes and noise studies.

Further scrutiny of the data once it is written to disk is done offline at Tier 0, which is the CERN on-site data-processing centre. Here full reconstruction algorithms are run, and every procedure not conforming to the strict time constraints imposed on the online environment is carried out. After this step the data is ready for distribution among off-site computer centres.

Chapter 3

Liquid Argon Noise Studies

Following Event Filter acceptance, events are required to pass rigorous data quality (DQ) checks offline, before being cleared to be used in physics analyses. These offline DQ checks are numerous, and with LAr being a large detector sub-system, many checks are associated with the performance of this particular detector system. This section focuses on studies related to noise bursts and sporadically noisy cells in the LAr detector. Noise bursts occur when a sudden electronic effect causes many calorimeter cells to fire at once, resulting in large energy readings from the affected region. Additional "fake" energy deposits can be seeded by cells that suffer from sporadic noise. These tend to be more isolated than noise bursts in that they involve individual cells rather than larger regions of the calorimeter. In both cases, such events are not from physics processes, and so they must be vetoed from physics analyses. This chapter explains the various methods used to identify and flag noise bursts and sporadically noisy channels and includes details on several studies made into the nature of sporadic cell noise, particularly with regards to the EMPS.

3.1 Trigger Streams for Noise Studies

In order to facilitate the study of cell noise the detector behaviour in the absence of physics data must be monitored. To do this, trigger streams with very low-threshold cuts are maintained, in order to ensure that even low-level noise is picked up. In addition to this, trigger streams can be designed such that events are only recorded if they occur on "empty" bunch-crossings, meaning that no collisions have taken place and there are no crossing protons. In this way, information on the noise evolution of individual cells and partitions can be monitored while simultaneously taking physics data.

One such trigger stream is the so-called "CosmicCalo" stream. This stream is subject to the lowest threshold empty triggers - "empty" meaning they are triggered on empty bunch crossings - (a full list of these L1 triggers is given in Table 3.1), and as such has a very high event pass rate. In order to manage such high acceptance the CosmicCalo stream is heavily pre-scaled. This limits the content of the CosmicCalo stream, with many events being discarded, resulting in potential LAr noise being overlooked.

As an alternative to CosmicCalo, the LArCellsEmpty stream was introduced. This stream also uses the low-threshold empty triggers at L1, but is not subject to the same pre-scales as CosmicCalo at L2. This is made possible via partial-event building, which is employed in this stream. Only the region of interest surrounding the trigger tower (typically a region of $\Delta\eta \times \Delta\phi = 0.2 \times 0.2$) in question is written out, permitting the storage of more events in total compared with CosmicCalo. Table 3.2 shows the number of events recorded in the LArCellsEmpty, CosmicCalo and some other physics streams used for analysis, for an example proton run from mid-2011. The total number of events recorded in the CosmicCalo stream is 30% of the LArCellsEmpty event count. Table 3.2 also shows that 21% of the events recorded in LArCellsEmpty also appear in the CosmicCalo, and in fact for run 183003 this corresponds to 73% of the content of the CosmicCalo stream being duplicated in LArCellsEmpty. With such a large proportion of CosmicCalo events being recorded by both these streams compared with the far smaller fraction of the LArCellsEmpty event population being captured in CosmicCalo, the motivation for using LArCellsEmpty to ensure higher statistics is clear.

L1 Trigger Chain	Pre-Scale	Conditions
L1_ EM3_ EMPTY	$\sim 10^2$	$E > 3$ GeV in the ECAL
L1_ EM5_ EMPTY	$\sim 10^2$	$E > 5$ GeV in the ECAL
L1_ TAU8_ EMPTY	~ 10	Tau candidate $E > 8$ GeV
L1_ J10_ EMPTY	$\sim 10^2 - 10^3$	Central jets ($\|\eta\| > 3.2$) $E > 10$ GeV
L1_ FJ10_ EMPTY	~ 1	Forward jets ($\|\eta\| > 3.2$) $E > 10$ GeV
L1_ J30_ EMPTY	$\sim 10^2 - 10^3$	Central jets ($\|\eta\| > 3.2$) $E > 30$ GeV

Table 3.1: List of L1 triggers feeding the CosmicCalo and LArCellsEmpty streams along with typical associated trigger pre-scale values. All listed items trigger on empty bunch-crossings (no collisions). The energy values listed here are uncalibrated, and therefore do not correspond to "real" jet energies, for example.

Stream	Events Recorded	Overlap (% events)
LArCellsEmpty	741,692	100
CosmicMuons	93,987	0.00054
JetTauEtmiss	6,111,758	0.05
Egamma	4,597,927	0.00013
Muons	4,133,179	0.0036
CosmicCalo	218,028	21
IDCosmic	3,441	0.00054

Table 3.2: Percentage of events in LArCellsEmpty also recorded in other physics streams along with the total number of events recorded in each stream. Values are taken from a single proton physics run (Run Number 183003) which was taken over Wednesday June 1st and Thursday June 2nd 2011, totalling 1080 LBs of which 911 were under stable beams with 897 declared "ready for physics."

3.2 Noise Bursts

At ATLAS noise bursts often effect a whole LAr partition, with noisy channels in large fractions of the EM barrel or end-caps. The patterns in $\eta - \phi$ are always more or less the same, with possible sites of injection being situated at $\eta \sim 1.4$ (1.5) in the EMB (EMEC). The origin of the bursts themselves is not currently understood, but their potential impact on physics data motivates the removal of noise burst events from physics data streams prior to physics analysis.

3.2.1 Noise Burst Identification

Dedicated algorithms are used in order to identify and flag noise bursts offline. These are defined as follows:

- LArNoisyROAlg_std – This is the "standard" LAr Noisy Read Out Algorithm. For each FEB ($\sim$ 128 channels) the number of channels with a bad q-factor ($q > 4000$) is extracted; if the FEB contains more than 30 channels fitting this prescription, it is declared to be noisy; if an event contains more than five 5 noisy FEBs (strictly *more* than), the event is flagged as a noise burst candidate by this algorithm.

- LArNoisyROAlg_SatMedium – This is the "medium saturated" LAr Noisy Read Out Algorithm. If an event contains more than 9 cells with $|E| > 0.5$ GeV and a *saturated* q-factor (q-factor = 65535) then the event is flagged as a noise burst candidate by this algorithm.

- LArNoisyROAlg_SatTight – This is the "tight saturated" LAr Noisy Read Out Algorithm. If an event contains more than 20 cells with $|E| > 1$ GeV and a *saturated* q-factor (q-factor = 65535) then the event is flagged as a noise burst candidate by this algorithm.

These algorithms are run in the CosmicCalo so that noise bursts are not confused with events originating from collisions. By default events flagged with the standard flag are denoted as "severe" noise bursts, given their large detector coverage, and must be discarded. In 2011 the LB in which the offending event occurred - as opposed to the event itself - was flagged as a whole, and so the entire LB removed from physics data. This corresponds to a loss of information on up to 24 billion interactions per noise burst, a rather large amount. In fact noise bursts tend to last somewhere between 1 μs and 1 ms. For 2012 running the development of an event "time-window" veto resulted in the ability to remove all events occurring within a small period surrounding a noise burst event. This time window is typically of the order of a few ns, a vast improvement on the ~ 60 seconds lost upon rejecting an entire LB.

In the case of flagging noise bursts based on individual LBs the following prescription was in force for the majority of 2011 data-taking:

- Yield of events flagged by LArNoisyRO_Std> 0: SEVNOISEBURST

- Yield of events flagged by LArNoisyRO_SatTight> 5% *or* LArNoisyRO_SatMedium> 10%: SEVNOISEBURST

- Yield of events flagged by LArNoisyRO_SatTight> 2% *or* LArNoisyRO_SatMedium> 5%: NOISEBURST

The SEVNOISEBURST flag indicates a severe noise burst. This is classified by LAr DQ as an intolerable defect, with LBs fitting this criteria rejected from physics analyses. In the case of the NOISEBURST flag, which indicates a "tolerable" defect, a LAr warning keyword is recorded so that in principle the event itself can be discarded during physics analyses as the analysis groups perform their own "event cleaning" procedure.

3.2.2 LArCellsEmpty and CosmicCalo Noise Burst Monitoring

All methods and techniques to implement noise burst cleaning rely on the ability to identify and flag noise bursts in data. Since the LArCellsEmpty stream will record many more events in a typical run compared with CosmicCalo it is natural to wonder whether LArCellsEmpty might record some noise burst events missed by the CosmicCalo stream. Noise burst events identified upon applying the LArNoisyRO algorithms to data recorded in the CosmicCalo stream are compared as they appear in the CosmicCalo and LArCellsEmpty streams. This can be done fairly easily since each recorded event is allocated a unique event number. This, along with the ATLAS run number, means that every event can be uniquely identified and filtered out for comparison if so needed.

In the CosmicCalo stream there are two main event variables pertaining to noise burst specification. Firstly, the LArNoisyRO flag assigned to an event; and secondly, the percentage of cells in the 3σ "tails" per event. The latter refers to the percentage of calorimeter cells contributing to an event with an energy value $E_{\text{cell}}/\text{noise} > 3$. Here "noise" is the sum in quadrature of the electronic and pile-up noise associated with the cell in question. These values are gleaned from calibration runs and vary from cell to cell, therefore they are being constantly updated.

In the LArCellsEmpty stream this information is not recorded, since it is a calibration stream rather than a physics stream. Information is gathered on a cell-by-cell basis rather than event-by-event. Events in a particular cell are only triggered for read-out to LArCellsEmpty if the value of the maximum sample [1] (the third sample taken to measure the pulse read out from the cell in question), less the value of the pedestal for the cell, is more than five times the pedestal RMS value (if $(s_3 - ped)/ped_{RMS} > 5 \rightarrow$ record event for the cell in question). Since for LArCellsEmpty only the RoI surrounding the trigger tower is written out, cells triggered by a noise burst event may not necessarily be associated with that particular event in the LArCellsEmpty stream if the energy deposition in the cell in question is below this threshold.

Owing to the absence of the LArNoisyRO flag in the LArCellsEmpty stream, the yield of cells in the 3σ tails are compared for several runs listed in Table 3.3. This comparison is complicated by the fact that an event in the 3σ tails in CosmicCalo will not necessarily have satisfied the criteria to be stored in the LArCellsEmpy stream. The conditions are not exactly equivalent, but it is interesting to see how many events are matched between streams and whether or not matched events look similar in each. Most importantly, are there noise burst candidates appearing in the LArCellsEmpty stream that do not appear in CosmicCalo? If so, it could be that some noise bursts in collision runs are being missed.

Run Number	Stable Beams (LBs)	Ready for Physics (LBs)	Total LBs	Date and Time
182424	104758	112748	777	Sat May 21 2011 18:53:52 – Sun May 22, 07:26:51
182454	185416	191412	420	Sun May 22 2011 23:10:57 – Mon May 23, 05:31:58
182456	1572	5562	591	Mon May 23 2011 10:23:25 – 20:04:48
182486	148760	155756	770	Mon May 23 2011 23:47:56 – Tue May 24, 12:29:35
182518	156210	163210	210	Wed May 25 2011 05:42:57 – 09:14:17
182676	FALSE	FALSE	596	Thu May 26 2011 18:13:51 – Fri May 27, 04:23:30
182726	206318	213315	323	Fri May 27 2011 19:16:22 – Sat May 28, 00:32:06
183003	169-1080	1771074	1080	Wed Jun 01 2011 23:15:48 – Thu Jun 02, 16:57:25
183347	7511340	7571330	1344	Fri Jun 10 2011 15:12:48 – Sat Jun 11, 13:29:06
183462	3961331	4021330	1336	Tue Jun 14 2011 00:55:31 – 22:42:04
183581	204676	209673	739	Fri Jun 17 2011 02:53:14 – 15:06:44

Table 3.3: List of data runs used to study the nature of noise bursts in the LArCellsEmpty and CosmicCalo streams.

[1] Here "sample" refers to the samplings taken at 25 ns intervals to reconstruct the physics pulse from the LAr cells.

The top three distributions in Figure 3.1 show the percentage of cells in the 3σ tails for events in CosmicCalo flagged with the LArNoisyRO_Std Algorithm compared with events written to the LArCellsEmpty stream. The two appear to be highly correlated, with the CosmicCalo stream having a factor of ~ 2 higher percentage of cells in the 3σ tails compared with the same event in LArCellsEmpty. The shape of these distributions is similar to those shown in the bottom left and right plots of Figure 3.1, which show the percentage of cells in the 3σ tails in CosmicCalo compared with the number of RoIs written out in LArCellsEmpty. There are some cases where events in CosmicCalo show high cell yields with far fewer cells showing up in LArCellsEmpty. This could be explained by the fact that the LArCellsEmpty stream will not include cells in an event if the energy deposited in those cells is very low and the cells occur outside the RoI that has been written out. In these cases it is possible that there are many cells with relatively low energy deposits associated with a noise burst event. Such cells would be included in CosmicCalo, but neglected in LArCellsEmpty. The same apparent correlation can be seen in Figure 3.2, which gives the same distributions for events flagged with the tight algorithm, though here there are more events with low noisy cell yields from CosmicCalo having correspondingly low yields in LArCellsEmpty. This suggests a higher event overlap between streams for events flagged with this algorithm compared with the standard flag. This is confirmed by the bottom middle distributions of Figures 3.1 and 3.2, which show the number of events matched between streams in each run studied.

In order to visualise what a noise burst event looks like in each of these streams it is intuitive to plot the energy distribution in the $\eta - \phi$ plane. Figures 3.3 and 3.4 compare the distribution of energy for single noise burst events in the CosmicCalo and LArCellsEmpty streams for example events flagged using the standard (Figure 3.3) and tight saturated (Figure 3.4) algorithms. In general it is obvious that a far larger area of the detector is written out in the CosmicCalo stream. Figure 3.4 in particular illustrates how the higher energy deposits show similar patterns in both streams, with the lesser deposits being omitted from LArCellsEmpty. For this reason the cell yields in LArCellsEmpty will always be less than those in CosmicCalo – unless of course an event is missed by CosmicCalo completely.

In order to check for the occurrence of noise burst events in LArCellsEmpty that do not appear in CosmicCalo, events are selected in the LArCellsEmpty stream if the number of cells contributing to the energy total of the event is $> 1\%$. These events are compared with noise burst events flagged with the standard algorithm in the CosmicCalo stream. Run 182424 is used to search for these events. It is found that one event is found in the LArCellsEmpty stream in a LB which has no associated noise burst events according to CosmicCalo (Figure **??**). Since a whole LB is discarded if one such event occurs within it this could be an example of a noise burst LB being overlooked. However, comparing the energy deposits in $\eta - \phi$ (Figure 3.6) shows that this event is very low energy, and so would not classify as a major concern for DQ. It is also worth pointing out that often if noise burst events are not picked up by the standard flag they are instead flagged by the tight saturated algorithm.

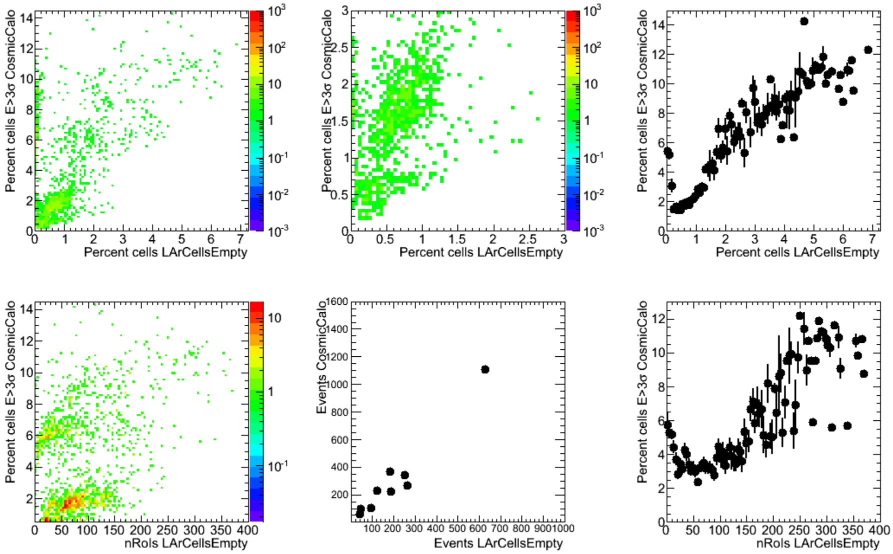

Figure 3.1: Comparing the events written to the LArCellsEmpty and events flagged with LArNoisyROAlg_Std in CosmicCalo. The percentage of cells are compared in the top three plots, with the middle plot focusing in on the region where the percentage of cells in each stream are below 3%. The bottom left and right plots show the percentage of cells in the 3σ tails for LArNoisyROAlg_Std in the CosmicCalo stream compared with the number of RoIs written out in LArCellsEmpty. The lower middle distribution compares the number of matched events in each stream, with one data point representing a single run.

The conclusion of this exercise is that though noise burst events do appear in the LArCellsEmpty stream, the limited coverage provided for each event means that the CosmicCalo stream does better at providing the information required to flag them. No convincing noise burst candidates were found in the LArCellsEmpty stream that were not also present in CosmicCalo. The LArCellsEmpty stream, therefore, would not be recommended as a stream in which to search for noise burst events.

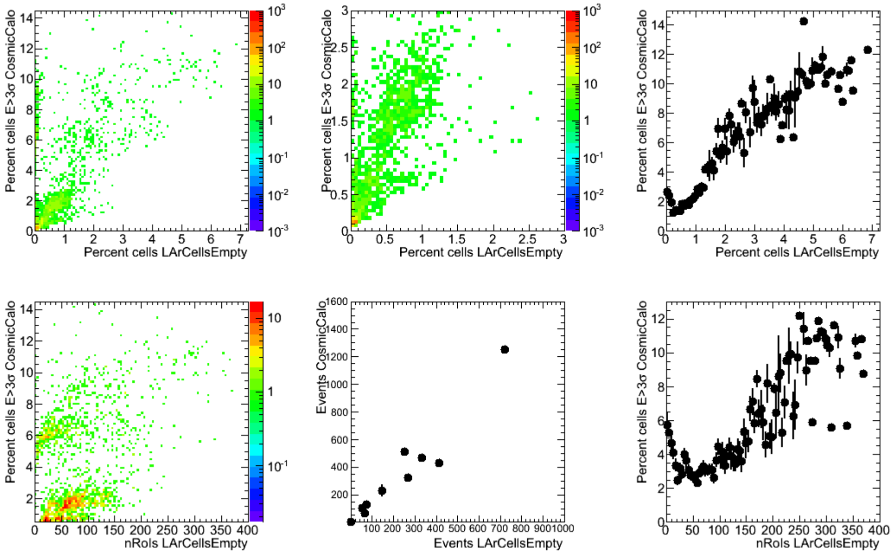

Figure 3.2: Comparing the events written to the LArCellsEmpty and events flagged with LArNoisyROAlg_SatTight in CosmicCalo. The percentage of cells are compared in the top three plots, with the middle plot focusing in on the region where the percentage of cells in each stream are below 3%. The bottom left and right plots show the percentage of cells in the 3σ tails for LArNoisyROAlg_SatTight in the CosmicCalo stream compared with the number of RoIs written out in LArCellsEmpty. The lower middle distribution compares the number of matched events in each stream, with one data point representing a single run.

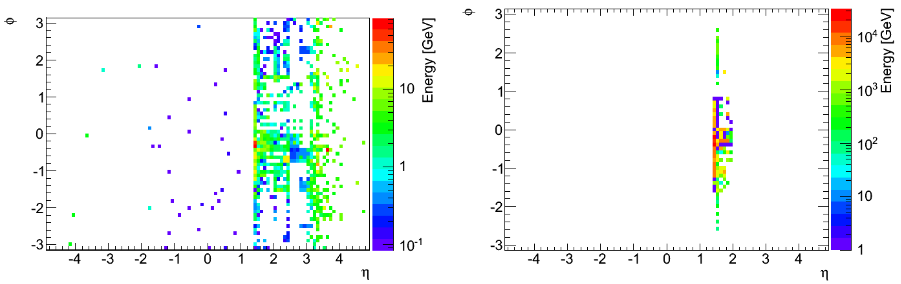

Figure 3.3: The energy distribution of a noise burst event in $\eta - \phi$ as recorded by the CosmicCalo (left) and LArCellsEmpty (right) streams. This event was flagged by the LArNoisyRO_Std Algorithm during ATLAS run 182424.

3.3 Sporadically Noisy Channels

There are several types of noise issues associated with read-out in the LAr calorimeter that have been identified during the running of the LHC. The majority of these have a fairly low-level effect, with significant contributors like the noise bursts de-

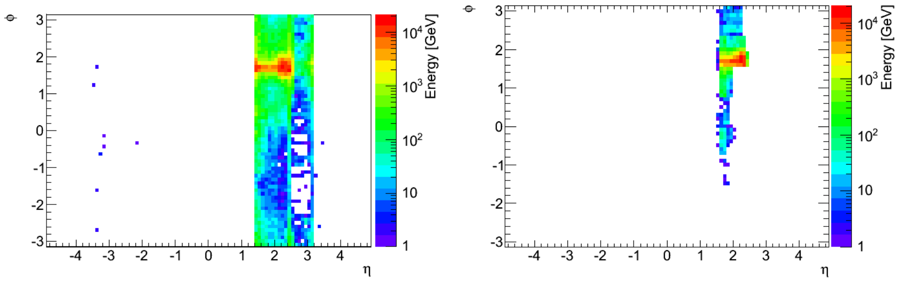

Figure 3.4: The energy distribution of a noise burst event in $\eta - \phi$ as recorded by the CosmicCalo (left) and LArCellsEmpty (right) streams. This event was flagged by the LArNoisyRO_SatTight Algorithm during ATLAS run 182424.

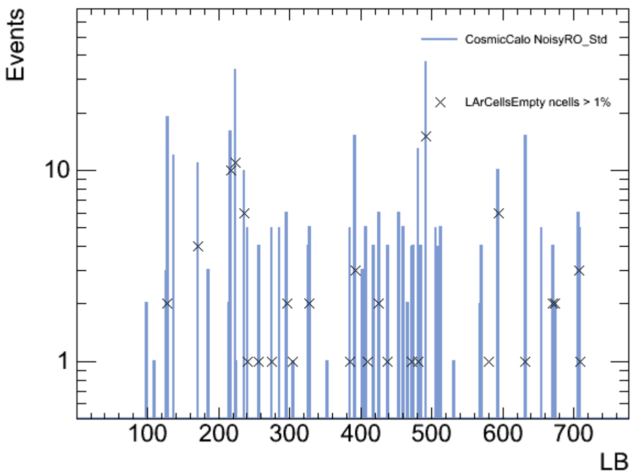

Figure 3.5: Number of events marked with the standard flag in CosmicCalo and marked as having a cell yield of $> 1\%$ in LArCellsEmpty per LB for run 182424. One instance of a LB where an event is flagged in LArCellsEmpty, with no noise bursts having been identified (with the standard flag) in the CosmicCalo stream can be seen around LB 570.

scribed in the previous section being sought out and removed from physics streams to ensure high quality data. Of course, all cells have some baseline noise associated with them. The approximate electronic noise expected for cells in various parts of the calorimeter is shown in Figure 3.7. This noise is known from calibration, and updated accordingly every time a calibration run is taken. Other noise categories are potentially problematic if frequently occurring or permanently present. In simple terms, such candidates include the following:

- Permanently noisy channels – These tend to be isolated cells which permanently display raised baseline noise compared with its neighbours. Such chan-

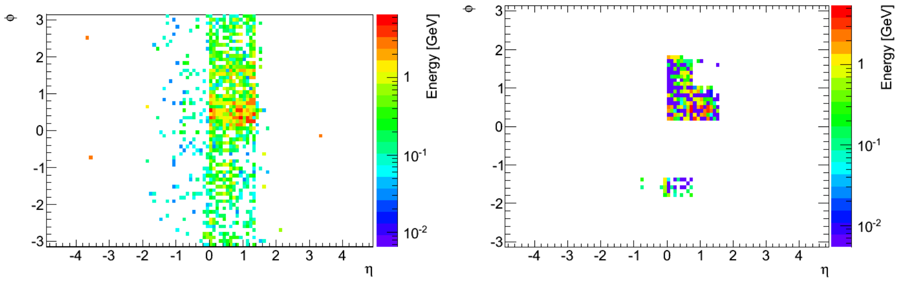

Figure 3.6: The energy distribution of a noise burst candidate event in $\eta - \phi$ as recorded by the CosmicCalo (left) and LArCellsEmpty (right) streams. This event has a cell yield of > 1% in the LArCellsEmpty stream, and was recorded during ATLAS run 182424.

nels are generally spotted during calibration runs and flagged as having "highNoise," and the prescription is to mask the offending cell. Having been flagged as highNoise, a cell would not be included in reconstruction, being treated in much the same way as if it were "dead." Only a dozen or so channels are flagged as high noise at one time, with the noise database being constantly updated as a result of daily calibration runs.

- HEC spikes – Large energy deposits of order 1 TeV affect individual channels in the HEC, with the noise occasionally appearing to propagate to neighbouring cells. This effect has been observed both in the presence and absence of collisions, though the rate of occurrence is seemingly decreasing with increasing instantaneous luminosity. Physics events containing an instance of a HEC spike will be removed at the analysis level with jet quality and event cleaning cuts, as described in Sections 4.1.3 and 4.2.

- Sporadic noise – In the case of sporadic noise, large energy deposits are observed in isolated LAr cells at an apparently randomly fluctuating rate. A cell can be actively noisy over the period of a few hours to a few days and remain silent thereafter. In some cases the noise occurs frequently enough to increase the L1 calorimeter trigger rates. The number of channels suffering from sporadic noise is constantly changing, with the intermittent nature of the noise complicating the diagnosis and treatment. These channels are flagged as "sporadicBurstNoise."

It is the last category in the above list that is the subject of investigation in this section. With the cause of sporadic noise yet to be determined, attention towards the understanding of the nature and behaviour of this noise is imperative to its prevention.

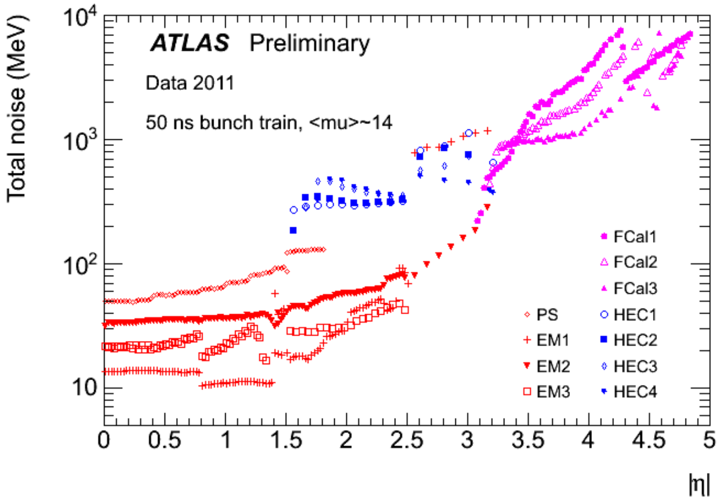

Figure 3.7: Total electronic and pileup noise seen in 2011 data for different partitions of the LAr calorimeter [17]. Noise is calibrated to the electron energy scale.

Currently sporadic noise is treated offline during the 36 hour calibration loop, during which time the data is subject to quality checks before being cleared for processing and reconstruction. If a cell is flagged as sporadicBurstNoise it is treated on an event-by-event basis, with the following prescription:

- $q > 4000$ – In this case the cell is regarded in the same way as those flagged "highNoise," being masked in the reconstruction.

- $q < 4000$ – In this case the cell is treated like any other calorimeter cell.

In order for sporadically noisy channels to be treated offline they have to be effectively flagged as sporadicBurstNoise. Reliable and comprehensive flagging of noisy channels relies on basic understanding on the noise characteristics to isolate noisy channels. In the following sections, the LArCellsEmpty stream is used to identify and study noisy channels, with the aim of optimising the cell monitoring procedure and gaining a better understanding as to the nature of sporadic noise in LAr.

3.3.1 Identification of Noisy Channels

The LArCellsEmpty stream is useful for noise studies, since information is recorded on a cell-by-cell basis, permitting the isolation of individual cells and their properties. In order for an event to be recorded in the LArCellsEmpty stream, the signal pulse read-out from a cell must be $\mathrm{ADC}_{\mathrm{max}} > 5\sigma$. On this basis the RoI surrounding the trigger tower in question will be written to the LArCellsEmpty stream. The distribution of the cell mean energy, denoting the mean of the energy distribution in a each LAr cell included in an example run, yields a peak at ~ 8 GeV shown in Figure 3.8a. Comparing this distribution for all calorimeter cells (black line) to those in the barrel pre-sampler only indicates that the PS is largely responsible for triggering the read-out to LArCellsEmpty. During the run in question an individual cell included in the LArCellsEmpty stream is found to record, on average, ~ 8 events leaving an energy deposit $E > 4\sigma$. Cuts upon the number of cell hits ($E > 4\sigma$) are applied systematically to this sample, and the effect on the distribution of cell mean energy can be seen in Figure 3.8b, with the results summarised in Table 3.4. From the distributions of Figure 3.8 two noise populations can be identified. A portion of cells in the PS are firing multiple times yielding mean cell energies of up to 10 GeV, with a smaller number of cells producing less frequent bursts, but at higher energies.

Cell hit threshold ($E > 4\sigma$)	Number of LAr cells	Number of EMBPS cells	% of sample from EMBPS
8	1319	1060	80%
10	1087	910	84%
18	868	752	87%
41	516	491	88%

Table 3.4: Number of LAr cells passing increasingly tight cuts on the number of hits/counts with $E > 4\sigma$, for ATLAS run 166466. Cells with the highest event counts appear mostly in the EMBPS. The effect these cuts have on the mean cell energy distribution can be seen in Figure 3.8b.

Based on these separate populations of noisy channels, three separate flagging algorithms are employed. The first, more complicated algorithm aims to identify noisy PS cells. The cut thresholds tested above are chosen based on the mean number of hits per cell (baseline requirement to denote a "hit" will be $E > 4\sigma$ for the duration of this section unless otherwise stated) as calculated for the run in question. The time over which an ATLAS run lasts is not stable, with some runs being longer in duration that others. In order to normalise the average number of cell hits over a more stable time period, the average number of hits per cell is determined on a LB by LB basis. This calculation is made by first determining the average number of hits per cell (with $E > 10\sigma$ this time, the baseline having been raised in order to avoid over-flagging cells in the EMBPS) within each LB in the given run:

$$< N_{\text{cell counts}}^{\text{LB},i} >= \frac{\sum_{i=1}^{N_{cells}} < N_{\text{hits}} >}{N_{\text{cells}}}, \tag{3.1}$$

where $< N_{\text{hits}}^{\text{LB},i} >$ is the mean number of hits per cell for LB i, $< N_{\text{hits}} >$ is the mean number of hits per cell (including only hits occurring within LB i) and N_{cells} denotes the number of LAr cells contributing to the cell hit count in LB i. This calculation is done for each individual LB. The mean of this quantity is then determined by:

$$< N^{\mathrm{LB,tot}}_{\mathrm{cell\ counts}} >= \frac{\sum_{i=1}^{N_{LB}} < N^{\mathrm{LB},i}_{\mathrm{hits}} >}{N_{\mathrm{LB}}} \tag{3.2}$$

where $< N^{\mathrm{LB,tot}}_{\mathrm{cell\ counts}} >$ denotes the mean number of hits per cell per LB, averaged over all LBs. Multiplying this quantity by the total number of LBs, N_{LB}, results in an estimate for the average number of hits per cell ($E > 10\sigma$), denoted by $< N^{\mathrm{hits}}_{\mathrm{cell}} >$. This is one of the quantities of interest in the LArCellsEmpty cell flagging criteria.

Three criteria for bad channel flagging are set:

1. number of counts ($E > 10\sigma$) in a cell are greater than 10 sigma from the mean ($< N^{\mathrm{hits}}_{\mathrm{cell}} >$),

2. number of counts ($E > 1$ GeV) are greater than 250 and the average energy per hit is more than 1.5 GeV,

3. number of counts ($E > 1$ GeV) are greater than 25 and the average energy per hit is more than 30 GeV.

Here first and second points target the PS cells, with the third focusing on the less frequent and more energetic energy deposits. The monitoring script runs on the LArCellsEmpty data, flagging a cell as "noisy" if it satisfies one of the criteria above, with (1) being referred to as the "MeanCellHits" cut and the others as the "EnergyThreshold" cuts.

These two complimentary cuts were introduced in May 2011 in a monitoring package to be run by the offline DQ shifters to check for and identify sporadic noise in data. The number of channels flagged by each of these algorithms was monitored over several runs during this period, the results are displayed in Table 3.5. The use of these algorithms results in a few hundred cells being flagged in every ATLAS run, a rather large amount. Extra refinements are required in order to improve bad channel identification.

Run number	MeanCellHits	EnergyThreshold	Both
178020	501	364	356
178021	428	209	193
178026	554	75	75
178044	483	816	429

Table 3.5: Number of LAr cells passing each flagging individual algorithm and both algorithms simultaneously in a sample of 2011 ATLAS runs

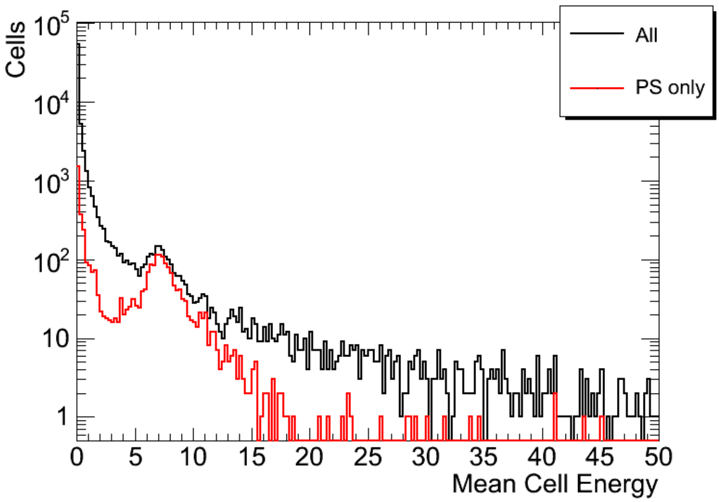

(a)

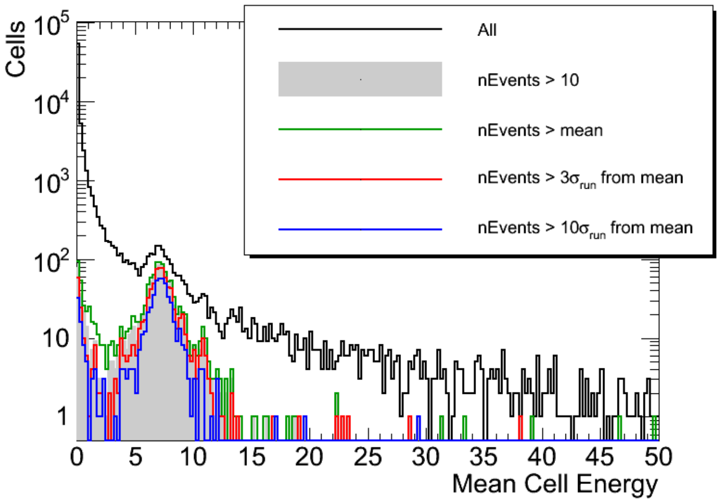

(b)

Figure 3.8: The cell mean energy distribution, measured in GeV, for LAr cells in ATLAS run number 166466 in the LArCellsEmpty stream. In 3.8a the black line includes all LAr channels, with the red line denoting cells in the EMBPS only. In 3.8b the cell mean energy distribution is shown for all cells (black), and only for cells experiencing more than 8 (green), 10 (grey), 18 (red) and 41 (blue) hits with $E > 4\sigma$ per cell. The turn on curve, peaking at approximately 8 GeV, is due to the L1 triggers thresholds.

One feature that has the potential to interfere with bad channel flagging, and is present in the LArCellsEmpty data samples, is noise due to noise bursts. A cell involved in a noise burst could be flagged by, in particular, the EnergyThreshold algorithm. In order to prevent channels being wrongly assigned SporadicBurstNoise status noise burst LBs must be removed from the LArCellsEmpty data prior to the flagging procedure. By retrieving the list of defect LBs from DQ these LBs can be removed from the samples prior to bad channel flagging. This list includes not only noise burst LBs, but LBs with HV trips and other intolerable defects, all of which are masked.

3.3.2 Luminosity Dependence

The cleaning procedure described in the previous section aids in noisy channel identification. Having isolated and flagged offending channels the nature of the noise itself can be studied further. The origin of the noise being unknown, any correlations or trends that can be identified could be useful to better understand its source. One such interesting feature is the dependence of the cell noise on instantaneous luminosity.

To study the luminosity dependence of sporadic noise, the number of channels flagged as a function of luminosity is monitored. A sample of ten runs from 2011, with luminosities in the range 4–12 $\times 10^{32}$ cm^{-2}s^{-1}, is run through the LArCellsEmpty flagging algorithm. The result can be seen in Figure 3.9. This distribution shows an increase in the number of channels flagged using the EnergyThreshold cuts of the previous section with increasing instantaneous luminosity. On closer inspection of the contributions from separate partitions, the PS can be seen to be the most notable offender. In fact, Figure 3.10 shows that this apparent correlation appears only in the PS, with the number of channels being flagged as a function of instantaneous luminosity in the other layers remaining more or less stable. Of course, the PS has far higher statistics. Closer inspection shows that this correlation with luminosity is prominent in the C-side PS only.

These results suggest that the population of cells firing multiple times in the PS bear some correlation with instantaneous luminosity, with this trend being most prominent in the C-side. For other calorimeter layers there is no obvious correlation.

Looking at the number of cells flagged as a function of LB for each layer in the barrel (Figure 3.11), the rate at which new cells are flagged in layers 1–3 remains reasonably constant. In the PS there are a large number of cells ($\sim$ 250 for this run) being flagged at the very beginning of the run, with this number settling to a constant value ($\sim$ 10 per LB) thereafter. Figure 3.12 shows the same distributions, though here a single cell may enter the distributions in any LB for which it passes the bad channel criteria. In this case the PS can be seen to be contribute many cells at a constant rate throughout the run, with a slightly downward slope in Figure 3.12, which could be further demonstration of the trend with instantaneous luminosity observed in the case of the pre-sampler cells. This suggests that there

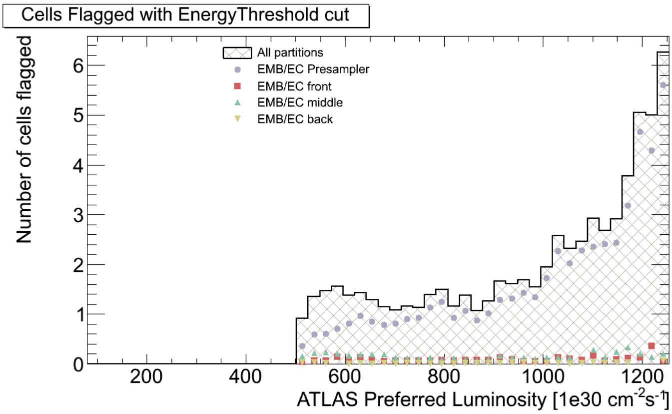

Figure 3.9: Number of LAr cells flagged (using the EnergyThreshold cuts described in Section 3.2.1) as a function of instantaneous luminosity at ATLAS ("ATLAS preferred" refers to the luminosity as measured online at ATLAS). Distribution is made using a sample of ten runs from 2011 proton-proton collisions.

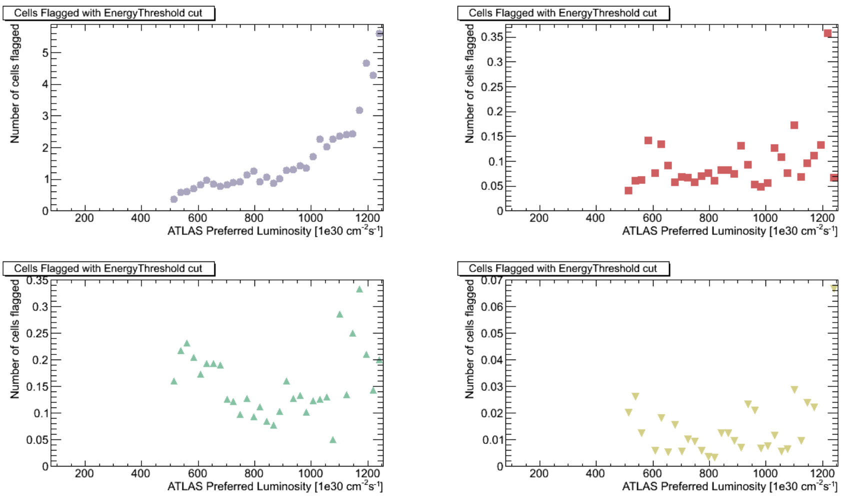

Figure 3.10: Number of cells flagged (using the EnergyThreshold cuts described in Section 3.2.1) as a function of instantaneous luminosity at ATLAS. Distribution is made using a sample of ten runs from 2011 proton-proton collisions. Luminosity dependence can be seen for cells in the PS (top left), first layer (top right), middle layer (bottom left) and back layer (bottom right) of the barrel and end-caps.

are a population of cells in the PS that fire almost every LB that are flagged in the first LB or so. For the other layers the rate of cell flagging appears constant.

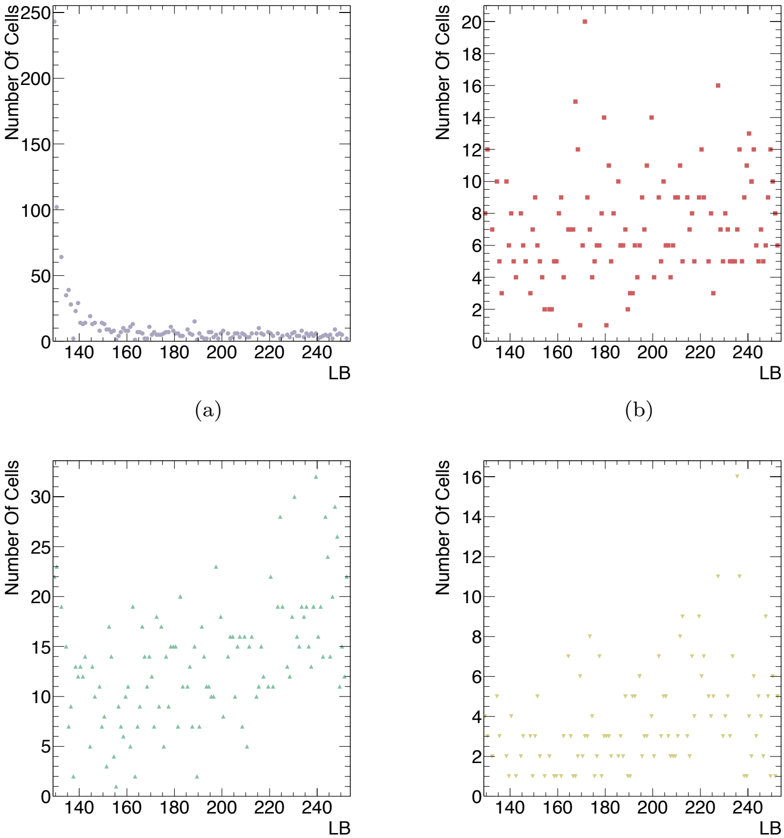

(a) (b) (c) (d)

Figure 3.11: Number of cells flagged in PS (a), front (b), middle (c), and back (d), layers of the EM barrel as a function of LB for an example run 191428 from October 2011. Once a cell has been flagged it remains so for the duration of the run, and so does not appear in subsequent LBs in these distributions.

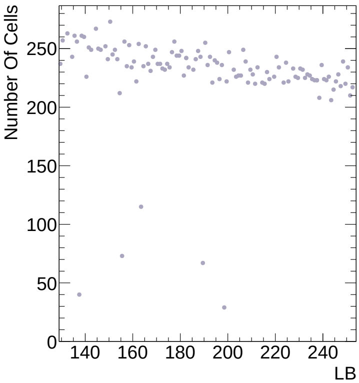

(a)

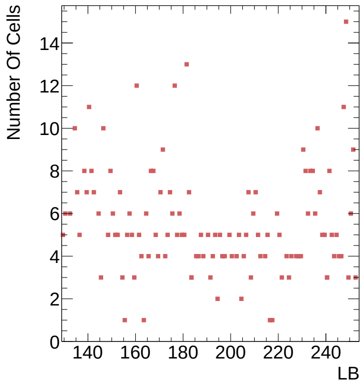

(b)

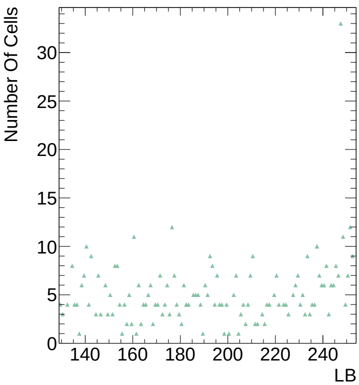

(c)

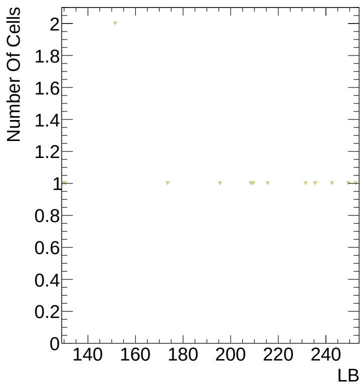

(d)

Figure 3.12: Number of cells flagged in PS (a), front (b), middle (c), and back (d), layers of the EM barrel as a function of LB for an example run 191428 from October 2011. Here a the cells are flagged on a LB by LB basis. A cell will enter into these distributions once for every LB in which it passes the bad cell criteria.

Chapter 4

Physics Object Selection

The interactions of interest at ATLAS involve a great number of particles, including electrons, muons, quarks and photons. These particles are identified at ATLAS by the way in which they interact with the detector material. The output from ATLAS is given in the form of energy deposits at specific locations within the detector. This section describes how exactly particles are identified and reconstructed at ATLAS, and how these physics "objects" are then passed on to be selected for physics analysis.

4.1 Object Definitions

At ATLAS each detector component plays a key role in particle identification. Analyses tend to work with physics "objects", and so detector output used for particle reconstruction rarely enters a physics analysis. Instead physics objects are built using various particle identification and reconstruction algorithms. In this way particle objects are loosely reconstructed and grouped into "containers" corresponding to the specific object. At this level the reconstruction criteria for each object is very loose, and as such is is possible for a single object to fall into more than one container. In order to remedy this apparent particle duplication "overlap removal" is performed on physics objects at an analysis level. More details on the overlap removal process will follow in this section.

4.1.1 Electrons

Electrons produced at ATLAS will penetrate the first two main detector subsystems, the inner detector and the ECAL. A track will be left in the inner detector while the electron energy is deposited in the ECAL. Electrons are reconstructed using the egamma algorithm. The first stage of electron identification is to find energy deposits, or "clusters" in the EM calorimeter. Energy deposited in the calorimeter are summed within longitudinal towers of 0.025×0.025 in $\Delta\eta \times \Delta\phi$, corresponding to the cell dimensions in the middle layer of the EM barrel. Scanning over regions of fixed size the "sliding window" locates local maxima in E_T, and this maximum then seeds a calorimeter cluster. For electrons, clusters are formed using 3×7

longitudinal towers in the barrel and 5×5 longitudinal towers in the end-caps. In the barrel the magnetic field causes bending of particle trajectories in the ϕ plane, which leads to the cluster size being larger in this dimension in order to contain as much of the electron energy as possible. In the end-caps the influence of the magnets is far less extreme, and so the η and ϕ dimensions are identical for clusters forming electrons. As the number of calorimeter cells incorporated into the formation of a cluster increases so too does the noise contribution to the energy read out. These cluster sizes are optimised in order to include most of the energy deposited by the particle in the calorimeter, while limiting the contribution from electronic noise. Following this, the seed cluster must be matched with a track in the tracker in order for the electron to be reconstructed. This matching is done by comparing the relative positions of the seed cluster and the inner detector track. These should lie within $\Delta\eta < 0.005$ of one another. Since the magnetic field of the solenoids causes the track that is extrapolated from the inner detector to the centre of the calorimeter cluster to bend, the requirements in the ϕ plane are $\Delta\phi < 0.01$ on the side where this bending occurs and $\Delta\phi < 0.005$ on the other. These $\eta - \phi$ requirements must be satisfied on comparing the track position to the cluster location in each calorimeter sampling. If there are more than three silicon hits in the electron track then η is taken as that associated with the track (η^{track}), otherwise the η associated with the calorimeter cluster (η^{cl}) is used. Since the fine granularity of the inner detector offers the highest precision in pin-pointing a particles position, the η measured using the tracker is most favourable.

The electron identification process uses information from the inner detector, ECAL and HCAL in order to facilitate satisfactory distinction between electrons and hadrons. In addition to the track extrapolation to the calorimeter cluster, the energy and momentum of the track and the cluster must also be in good agreement in order to reject the background from photon conversions. Energy deposits in the calorimeter due to electrons tend to be narrower than showers from hadrons, and the lateral shower shapes are used to discriminate between these and wider showers from jets. The first strip layers of the ECAL, with fine granularity, aid in identifying any substructure in showers originating from photons or pions. Electrons deposit their energy predominantly in the ECAL, with leakage into the hadronic portion of the calorimeter small compared with hadronic showers. For this reason the relative energy deposits in the two calorimeter systems serves as an additional discriminator between electrons and jets. By applying selection cuts on variables such as these, electron identification is categorised into three levels by the Egamma Algorithm, defining electrons to be "loose", "medium" or "tight". The conditions for these criteria are summarised in Table 4.1.

At an analysis level, certain constraints on the quality of electrons which are selected are put into place. These quality cuts make use of the different categories of electron identification in addition to further requirements on p_T and isolation, and are summarised in Table 4.2. So-called "baseline" electrons from 2011 data used in this analysis must satisfy the medium selection criteria [26], and are required to reside within $|\eta| < 2.47$. A baseline p_T cut of 10 GeV is imposed in order for an electron to be selected. For "signal" electrons the identification level is raised to tight, and these electrons should be isolated from other high-p_T charged particles in the event. To quantify this isolation the total transverse energy in a cone of radius $\Delta R > 0.2$ surrounding the electron must be less than 10% of the total E_T ($p_T^{cone20} < 0.1 \times p_T$). For the dilepton analysis, if the leading "good" electron is the leading lepton in the event, the p_T requirement imposed upon it is raised to 25 GeV. This ensures that the electron is on the trigger plateau, and hence is capable of having fired the single electron trigger.

In addition to the above, electrons (if the leading signal lepton in the event) selected from data are required to have a match in the level two trigger, meaning that the trigger fired due to the electron in question. Events from simulation are re-weighted to correct for discrepencies between the simulated (MC) and observed (data) effect of the single lepton triggers. The energy of electrons in simulated events is smeared prior to object selection according to the recommendations of the Egamma Working Group, to account for differences in resolution between data and MC. In order to account for differences in electron reconstruction efficiency, η- and E_T-dependent scale factors are applied to each electron surviving overlap removal and selection requirements in an MC event [26].

In general for SUSY analyses "baseline" lepton definitions are used for lepton rejection and leptons satisfying "signal" lepton definitions are desired for selection. A "zero-lepton" analysis would request events without baseline leptons, whereas an analysis focusing on leptonic channels would require events containing signal leptons.

Table 4.1: Electron identification variable definitions and cuts used on electrons within $|\eta| < 2.47$ for ATLAS data taken in 2011. For cuts which have been optimised for ten separate bins in η and in some cases eleven bins in p_T, a range for the variable in question is given.

Type	Description	Variable	Cut
	"Loose" electron cuts		
Hadronic leakage	Ratio of E_T in the HCAL compared to the E_T of the EM cluster	R_{had}	$< 0.01 - 0.065$
ECAL first layer	Fraction of cluster energy in sampling 1	f_1	< 0.005
	Total shower width in sampling 1	w_{tot}	$< 1.60 - 4.2$
	Ratio of the difference in energy between the two largest energy deposits in sampling 1 over their sum	E_{ratio}	$< 0.06 - 0.88$
ECAL second layer	Ratio of the energy sum in 3×7 cells over the energy sum in 7×7 cells	R_η	$> 0.7 - 0.92$
	Total shower width in sampling 2	$w_{\eta 2}$	$< 0.011 - 0.028$
Track	Number of pixel layer hits	N_{pix}	≥ 1
	Number of silicon hits	N_{si}	≥ 7
	Number of b-layer hits (if a b-layer hit is expected)	N_{BL}	≥ 1
	Transverse impact parameter with respect to the primary vertex	d_0	< 5 mm
	Difference between the track η and the η of the cluster	$\Delta\eta$	< 0.015
	Difference between the track ϕ and the ϕ of the cluster	$\Delta\phi$	< 0.015
	Upper limit on ratio of cluster energy and track momentum	E/p max	$< 2.5 - 10.0$
	Lower limit on ratio of cluster energy and track momentum	E/p min	$> 0.0 - 0.9$
TRT	Fraction of high threshold hits in the TRT ($|\eta| < 2.0$)	f_{HT}	$> 0.05 - 0.08$
	"Medium" electron cuts (includes "Loose" requirements)		
Track	Difference between the track η and the η of the cluster	$\Delta\eta$	< 0.005
	"Tight" electron cuts (includes "Medium" requirements)		
Track	Transverse impact parameter	d_0	< 1 mm
TRT	Fraction of high threshold hits in the TRT	f_{HT}	$> 0.10 - 0.13$

Table 4.2: Definitions and cuts defining baseline and signal electrons used for this analysis on 2011 data and simulation.

Type	Description	Variable	Cut
	Baseline electron cuts		
Identification	Electron identification requirement	el_{ID}	Medium
Momentum	Electron transverse energy	E_T	> 10 GeV
Position	Electron η position	$\|\eta\|$	< 2.47
	Signal electron cuts (includes baseline cuts)		
Identification	Electron identification requirement	el_{ID}	Tight
Momentum	Electron transverse energy	E_T	> 25 GeV
Isolation	Fraction of electron E_T contained within a cone of $\Delta R < 0.2$ surrounding the electron	$\frac{p_T^{cone20}}{p_T}$	< 0.1

4.1.2 Muons

Muons will penetrate each layer of the ATLAS detector, leaving evidence of its presence in all the sub-systems as it goes. This permits the use of information from the inner detector, calorimeters and the muon spectrometer to aid in muon identification and reconstruction. Muon identification begins in the muon system, where the passage of a muon through the MDT's allows the reconstruction of segments of the muon's track. The tracks identified in the candidate segments are fit, and a preliminary momentum estimate is extracted. The track from the combined segments is then extrapolated to inner detector, where it should be matched with an inner detector track. If a match is found, these tracks are merged using the STACO (STAtistical COmbination) algorithm. As a muon traverses the ATLAS detector it suffers energy loss in the calorimeters (typically at least 3 GeV), resulting in discrepencies between the muon momentum measurement from the inner detector and the muon spectrometer. The final step in muon identification involves correcting for this energy loss.

Selected muons for the dilepton analysis are reconstructed using the STACO algorithm following Ref. [27] with $p_T > 10$ GeV and $|\eta| < 2.4$. The STACO muons selected must be "combined" (where the reconstruction of a track in the muon spectrometer is the principle driver in the identification process) or "segment-tagged" (where reconstructed tracks in the inner detector are extrapolated to the muon system and matched to hits in the spectrometer segments) muons, according to the recommendation of the MCP (Muon Combined Performance) group at ATLAS. Signal muons are additionally required to be isolated from other high-p_T charged particles in the event ($p_T^{cone20} < 1.8$ GeV), and if the leading lepton in the event, the muon must have $p_T > 20$ GeV. All cuts associated with the inner detector track and muon quality for both baseline and signal muons are summarised in Table 4.3.

Trigger matching is performed on selected muons in data (as with electrons), and events in MC undergo trigger re-weighting. In simulation the muon momentum is smeared to better represent the resolution in data. The muon reconstruction efficiency differs between data and MC. In order to account for this, an η- and p_T-dependent scale factor is applied to each muon passing selection requirements and overlap removal in an MC event [28, 29].

Table 4.3: Muon identification variable definitions and cuts used on baseline and signal muons within $|\eta| < 2.4$ for ATLAS data taken in 2011.

Type	Description	Variable	Cut
	Baseline muon cuts		
Inner detector track	Number of pixel layer hits + number of dead pixels traversed	N_{pix}	≥ 1
	Number of SCT hits + number of dead SCTs traversed	N_{SCT}	≥ 7
	Number of b-layer hits (if a b-layer hit is expected)	N_{BL}	≥ 1
	Number of pixel and SCT holes	$N_{holes}^{pix,SCT}$	≤ 2
	Total number of TRT hits ($= N_{TRT}^{hits} + N_{TRT}^{outliers}$)		
	– if $\|\eta\| < 1.9$	N_{TRT}^{total}	> 5
		$N_{TRT}^{outliers}$	$> 0.9 N_{TRT}^{total}$
	– if $\|\eta\| \geq 1.9$ and $N_{TRT}^{total} > 5$		$> 0.9 N_{TRT}^{total}$
Momentum	Muon transverse momentum	p_T	> 10 GeV
	Signal muon cuts		
Isolation	Total p_T in a cone of radius $\Delta R > 0.2$ surrounding the muon	p_T^{cone20}	< 1.8 GeV
Momentum	Muon transverse momentum	p_T	> 20 GeV

4.1.3 Jets

Jets are comprised of hadronic particles, which will penetrate through the first three main detector sub-systems. If the hadrons are charged they will leave tracks in the inner detector, before depositing energy in both the EM and hadronic calorimeters. Energy deposits are collected together to form jet objects. There exist many algorithms which perform this grouping of jet objects, and each technique yields slightly different jet characteristics and results. Since all algorithms behave slightly differently and possess their own various features, the nature of reconstructed jets is heavily dependent on the particular algorithm in use. For this analysis jets are identified using the Anti-k$_t$ jet clustering algorithm [30, 31].

The Anti-k$_t$ algorithm looks at the p_T of each jet object in an event and iterates over constituent pairs. For each pair of jet objects, i and j, the quantity $k^2_{T,ij}$ is defined such that:

$$k^2_{T,ij} = min(p^{-2}_{T,i}, p^{-2}_{T,j}) \times \frac{\Delta R^2_{ij}}{D^2} \tag{4.1}$$

where ΔR_{ij} is the opening angle between the pair of objects given by $\sqrt{\Delta\eta_{ij} + \Delta\phi_{ij}}$, and D is the distance parameter which describes the typical jet size for the algorithm.

This iteration is performed over all constituent pairs and then the smallest value resulting from all the $k^2_{T,i}$ (where $k^2_{T,i} = p^{-2}_{T,i} \times D^{-2}$, the k^2_T of a single object) and $k^2_{T,ij}$ terms is extracted. If this minimum value is the $k^2_{T,ij}$ term for a pair of jet constituents, i and j, then these two constituents are merged. This process is repeated until the minimum is given by the $k^2_{T,i}$ value of a single object, at which point all objects merged to form jet object i have been combined to form a "final state" jet. This process is repeated until all jet objects are iterated over in this way, and the reconstruction of all final state jets is complete. By scrutinising all constituents the Anti-k$_t$ algorithm tends to perform well in including the majority of the original parton p_T in jet construction.

Clusters, which are fed into the Anti-k$_t$ algorithm, are seeded by cells acquiring energy deposits above 4σ of the cell noise. All neighbouring cells (in 3-dimensions) are included in this "pre-cluster." If a neighbouring cell has energy greater than 2σ above its background value, the neighbour's neighbours are included in the pre-cluster also. On top of this, an additional single layer of cells surrounding this pre-cluster is included in the cluster object.

In this analysis calorimeter jets with uncalibrated $p_T > 7$ GeV are reconstructed with a four-momentum recombination scheme. This means that the four-momenta of all constituent clusters are summed together to calculate the total jet four-momentum. These jet objects are identified using the Anti-k$_t$ algorithm with a distance parameter of $D = 0.4$.

Jet calibration is performed on reconstructed jets. Initially each calorimeter cell contributing to a jet is scaled to the electromagnetic energy scale (EM scale), which has been derived using test beam measurements of electrons a muons [32]. The EM scale correctly accounts for photon and electron energies, but does not account for detector leakage, dead material and inefficiencies associated with clustering and identification algorithms. Additionally, the non-compensating nature of the ATLAS calorimeters means that the calorimeter energy response is significantly different for electrons and photons, compared with hadrons. This feature must also be accounted for by correcting the jet energies to the hadronic scale. By comparing the reconstructed jet p_T in MC to the p_T at truth level[1], the jet energy response is derived as a function of p_T and η [33, 34]. The jet energy scale (JES) correction is applied on a jet by jet basis. On average for jets with $p_T \sim 20$ GeV, this calibration results in an increase of $\sim 40\%$ in the jet p_T, though this increase becomes less significant for much higher jet energies.

All reconstructed jets are required to pass several selection criteria, which remove specific non-collision backgrounds [34, 35]. The quality of jets are assessed using a collection of discriminating variables which are summarised in Table 4.4. Conditions for these non-collision backgrounds are summarised in Table 4.5.

Once calibrated, baseline jets are required to have $p_T > 20$ GeV and to reside within $|\eta| < 2.8$. For signal jets this η requirement is tightened to $|\eta| < 2.5$. Additionally, the jet vertex fraction (JVF) must be above 75%. This quantity represents the fraction of the total track p_T which is carried by tracks with impact parameters that are consistent with the primary vertex. This requirement on the JVF prevents photons from being classified as signal jets, since photons will not leave charged tracks. The requirements placed on baseline and signal jets are summarised in Table 4.6.

Heavy flavour b-jets are identified at an efficiency of 60% using the "jet fitter" algorithm [36]. As is the case for electrons and muons, scale factors are necessary to correct for discrepencies in heavy flavour physics in data and MC.

4.1.4 Overlap Removal

In order to ensure that objects are not duplicated in more than one collection of baseline objects, the following overlap removal procedure is performed. If any two baseline electrons lie within a distance of $\Delta R < 0.1$ of one another, the electron with the lowest E_T^{cl} is discarded. Following this, jets passing basic selections are required to be at least 0.2 units from all surviving baseline electrons in η–ϕ. Any jet failing this requirement is removed from the event. Baseline electrons are then required to be at least 0.4 units from all good jets in η–ϕ. Next, muons with $p_T > 250$ GeV within 0.2 units from a jet with $p_T > 500$ GeV are removed. Highly energetic jets which "punch-through" into the muon system can lead to a very high-energy muon being reconstructed from the jet debris. This causes the missing transverse momentum to be poorly measured, motivating their removal. Only $\mathcal{O}(10)$ events

[1] Truth information in MC refers to the "true" particle information in the simulation, as opposed to the information on the reconstructed particle (which is the only information available for real data).

Table 4.4: Discriminants used to identify and categorise bad jets.

Name	Description	Variable
EM fraction	Fraction of energy in the ECAL	f_{EM}
Samplig max fraction	Maximum energy fraction contained in a single calorimeter layer	f_{max}
HEC fraction	Fraction of energy in the HEC	f_{HEC}
LAr quality	Fraction of energy associated with LAr cells with a q-factor > 4000	LAr_Q
HEC quality	Fraction of energy associated with HEC cells with a q-factor > 4000	HEC_Q
Negative Energy	Negative energy associated with a jet	E_{Neg}
Mean LAr quality	Normalized jet quality ($= \frac{q}{65535}$)	LAr_Q^{mean}
Jet charged fraction	Ratio of the sum p_T of jets associated tracks and the calibrated jet p_T	f_{ch}

Table 4.5: Potential sources of bad jets and the cuts imposed on the discriminants introduced in Table 4.4 in orer to clean these events.

Source	Description	Cleaning cut
HEC spike	Large fake energy deposits in the HEC	$f_{HEC} > 0.5$ $\lvert HEC_Q\rvert > 0.5$ $LAr_Q^{mean} > 0.8$ **or** $E_{Neg} > 60$ GeV
EM noise	Noise in the EM calorimeter (sporadic, burst, etc.)	$f_{EM} > 0.95$ $\lvert LAr_Q\rvert > 0.8$ $LAr_Q^{mean} > 0.8$ $\lvert\eta\rvert < 2.8$
Cosmics/non-collision backgrounds	Cosmics and background noise	$f_{EM} < 0.05$ $f_{ch} < 0.05$ $\lvert\eta\rvert < 2$ **or** $f_{EM} < 0.05$ $\lvert\eta\rvert \geq 2$ **or** $f_{max} > 0.99$ $\lvert\eta\rvert < 2$

Table 4.6: Definitions and cuts defining baseline and signal jets used for this analysis on 2011 data and simulation.

Type	Description	Variable	Cut
	Baseline jet cuts		
Quality	Jet should not satisfy conditions listed in Table 4.5	Jet_Q	Good
Momentum	Jet transverse momentum	p_T	> 20 GeV
Position	Jet η position	$\lvert\eta\rvert$	< 2.8
	Signal jet cuts (includes baseline cuts)		
Track quality	Jet vertex fraction	JVF	> 0.75
Position	Jet η position	$\lvert\eta\rvert$	< 2.5

in the data are removed by this cut.

At this stage, the missing transverse momentum and the razor variables (see nect chapter) are calculated. By calculating all of these variables at once, a consistent view of the event is achieved. Calculating these variables before furthur overlap removal between jets and muons also ensures that energy possessed by muons produced within b-jets is also taken into account in the E_T^{miss} and razor variables.

Having computed the razor variables and E_T^{miss} for the event, baseline electrons and muons are then required to be at least 0.4 units from all good jets in η–ϕ. Any electron or muon failing this requirement is removed from the event. Finally, if any of the remaining baseline electrons and muons lie within $\Delta R < 0.1$ of one another, both objects are discarded. This cut is motivated by instances of muons undergoing bremsstrahlung where the photon is mis-identified as an electron, resulting in a poorly reconstructed muon and electron on top of one another. These objects are removed from the event so that they are not tagged as “good” leptons, but are still included in the calculation of the above mentioned event level variables in order to avoid inconsitencies in, for example, E_T^{miss}.

The electron-electron, electron-muon, and punchthrough jet-muon overlap removal were specifically investigated for their impact on the signal regions. No events containing such an overlap were found, in either data or MC simulation, to enter any of the dilepton signal regions.

4.1.5 Missing Transverse Momentum

Some objects (eg. neutrinos) will not interact with the detector system at all. In the case of supersymmetry, stable LSPs are expected to escape the ATLAS detector completely unnoticed. Evidence of the presence of such particles being produced will manifest in an energy inbalance in an event. As such, the ability to measure the amount of missing energy in an event with some surety is one of great importance.

The algorithm used to calculate E_T^{miss} includes all baseline electrons and muons, though for technical reasons electrons with $E_T < 20$ GeV are not taken into account. Jets calibrated at the EM+JES scale with $p_T > 20$ GeV are also entered into the calculation. The E_T^{miss}computation also takes into account the so-called "Cell-Out" term, which includes topological clusters not associated with reconstructed objects. All objects entering into the E_T^{miss} calculation do so after any associated smearing has been applied.

4.2 Event Cleaning

In addition to object identification, reconstruction and quality cuts, there is some further event level cleaning required in order to reject any poorly-reconstructed or contaminated events. For part of 2011 the LAr Calorimeter had a problem with 6 read-out FEBs. This resulted in a dead region of the calorimeter, affectionately referred to as the "LAr hole". The hole was situated in samplings 2 and 3 of the EMBA, and corresponded to a loss of coverage in a region of $\Delta\eta \times \Delta\phi = 0.2 \times 0.14$. Data collected during this period (and a corresponding fraction of MC events also) is checked using the "smart LAr hole veto". Any event failing this smart veto is rejected [27]. The smart LAr hole veto determines whether or not the energy in the event which is pointing towards the LAr hole (if any) contributes significantly to the E_T^{miss}in the event (typical thresholds $\sim 10\%$). Applying the smart LAr hole veto results in the removal of less than 0.1% of events in data.

Events with cosmic muon candidates are vetoed, so as to avoid counting events with artificially large E_T^{miss}. A muon is considered a cosmic candidate if it satisfies $|d_0| > 0.2$ mm and $|z_0| > 1$ mm with respect to the primary vertex. Events are also discarded if they contain so-called "bad" muons. Such muons are poorly measured and tend to fail isolation requirements, as such any event containing a muon with $\Delta_{q/p}/|q/p| \geq 0.2$ is rejected. This check is performed prior to muon-jet and muon-electron overlap removal.

Each selected event also undergoes "bad jet cleaning". Jets are quality assessed using the identifiers in Table 4.4. Specific cuts and thresholds are set to discriminate between potential sources of fake energy or energy not originating from the event (Table 4.5). This allows the definition of different levels of "bad" jets. Events are rejected if they contain a "very loose" bad jet or an "ugly" jet with $p_T > 20$ GeV. Very loose bad jets are removed because they either come from background events or are a consequence of detector defects. Ugly jets tend to be badly measured jets which are positioned in problematic regions of the calorimeter. This check for bad jets is made after overlap removal.

Problems in the MC11 simulation made it necessary to introduce the final event cleaning cuts. Events without an MC event record are removed. In addition to this, events associated with a known bug regarding energy conservation in simulation are discarded from the analysis. These MC cleaning cuts result in the removal of less than 0.1% of events in a handful of simulated samples.

4.3 Data Set and Event Selection

In 2011 ATLAS recorded ~ 4.7 fb^{-1} [37] of data, and this entire dataset is used in this analysis. The data was processed in Athena [38] release 17 and accessed for this work in the form of centrally produced, official SUSY group ntuples (version p832). All data is checked against the official "Good Runs List" in order to ensure that data used for physics analyses satisfies all data quality and integrity requirements.

4.3.1 Data Periods

During 2011 operation the ATLAS run conditions were not completely stable. For example, at times there have been hardware issues, where part of the detector may be switched off or masked. In order to identify data taken during an interval of approximately constant data-taking conditions the data is grouped into "periods." One period corresponds to a period during which the detector sub-systems are in a more or less stable configuration. The most notable periods and the corresponding state of the ATLAS detector sub-systems are listed in Table 4.7.

Period	LAr conditions	Tile conditions	Pixel conditions
B-D	All OK	5 dead modules	54 dead pixel modules 7 dead b-layer modules
E-H	6 dead FEBs	6 dead modules	56 dead pixel modules 7 dead b-layer modules
I-K	2 dead FEBs	7 dead modules	62 dead pixel modules 10 dead b-layer modules
L-M	2 dead FEBs	9 dead modules	63 dead pixel modules 10 dead b-layer modules

Table 4.7: Data-taking periods at ATLAS. During 2011 periods B-M were used for analysis. During Period A the central solenoid was switched off, and for part of it no bunch trains were introduced to the LHC ring. Periods E-H correspond to the LAr hole period, where the 6 dead FEBs resulted in a rather large region of the EMB being completely dead to read-out.

4.3.2 Analysis Triggers

In order to select events for a leptonic SUSY search, single lepton triggers are used at the event filter (EF) level. Since it is desirable to use triggers which are pre-scaled as little as possible, the lowest energy un-pre-scaled triggers available are selected from each data-taking period. All relevant triggers are listed in Table 4.8. The single muon triggers used for the lepton selection require at least one muon with a minimum p_T of 18 GeV. In the case of the electron triggers, an ever increasing instantaneous luminosity at ATLAS resulted in tightening trigger requirements. As such the p_T threshold for the lowest un-pre-scaled electron triggers increased from 20 GeV to 22 GeV during the course of 2011.

In order to ensure that the triggers used in this analysis are 100% efficient with respect to the selection of lepton objects, p_T cuts are imposed offline. Events which pass the electron triggers fall into the electron or “egamma” stream, and events which fire the muon trigger enter the muon stream. In order to account for events which result in both the electron and muon triggers firing, the electron stream always takes priority over the muon stream. Offline if an event has fired both triggers, it is taken from the electron stream and ignored in the muon stream to avoid double counting events.

Trigger	Integrated Lumi [fb^{-1}]	Periods
mu18	1.46 ± 0.06	A–I
mu18_medium	3.24 ± 0.13	J–M
e20_medium	1.69 ± 0.07	A–J
e22_medium	0.59 ± 0.02	K
e22vh_medium1 or e45_medium1	2.43 ± 0.09	L–M

Table 4.8: The lowest un-pre-scaled single lepton triggers for each data-taking period for 2011. The total integrated luminosity recorded for each trigger (following GRL cleaning) is given along with the corresponding periods for which the triggers were used.

Chapter 5

The Razor Variables

Searches for new physics processes must cover many different final states. Supersymmetric events, for example, could contain many jets, or just a few; there might be one lepton, two leptons, many leptons or none. Generally though, R-parity conserving SUSY models will require a certain amount of missing transverse momentum, energy escaping the ATLAS detector in the form of the elusive LSP. It is standard for SUSY (or indeed, alternative theories for "new physics") searches to pick a particular final state to probe and then diminish the SM background processes contributing to this search "channel" by imposing an E_T^{miss} requirement on events. Events producing the relevant final state objects will be selected only if they possess a transverse momentum imbalance above a certain threshold. One short-coming of E_T^{miss} as a discriminant is the difficulty associated with its calculation. Fake sources of E_T^{miss} include "hard" (high-momentum) hadronic jets punching-through into the muon system as well as detector defects and dead read-out modules.

Another signal characteristic one might consider derives from the implication of R-parity conserving models that heavy sparticles are pair-produced and decay thereafter into an even number of LSPs. As the particles resulting from pp collisions become increasingly heavy with respect to the LHC collision energy, the longitudinal boost to the particle-particle system should become less significant. It would therefore make sense for massive SUSY sparticles to appear less boosted compared with particles resulting from other lower mass processes. As such, SUSY searches often use transverse event information in order to separate potential SUSY events from background processes. Such transverse discriminants include effective mass (M_{eff})[1], for example. The variable set, upon which the di-lepton SUSY search featuring in this document is based, aims to isolate interesting SUSY-like events and reduce the SM background acceptance by taking advantage of the topology of signal processes without requiring an explicit E_T^{miss} cut. The "Razor" variables [39] exploit the somewhat symmetric sparticle decays inferred from the pair production of massive sparticles at the LHC. These variables were derived by Christopher Rogan in Ref. [39], and have been used in several SUSY analyses at CMS [40–43].

5.1 Concept and Definition

The concept of the Razor variables and the way in which this approximation is carried out is best described using a simple SUSY decay example. Consider an instance of squark pair-production at the LHC, where in this example each squark decays into a quark and an LSP. At the LHC the point of interaction along the z-axis cannot be known precisely, with collisions resulting in events being boosted in the longitudinal plane. A longitudinal boost, β_L, would have to be applied to the particle–particle system in order to move between the lab and centre-of-mass frames. Assuming the squarks are of the same mass and are produced with no transverse boost, in the di-squark ($\tilde{q}_1\tilde{q}_2$) rest frame - also the centre-of-mass frame in this example - the squarks have equal and opposite momenta. In practice the squarks will not be produced at rest, and so in order to reach the squark rest-frames from the centre-of-mass frame each squark must undergo an equal and opposite boost, β_T^R. In this frame, called the "rough-approximation-," or R-frame, the individual squark decays are symmetric, and it is this very feature the Razor variables exploit. This balance between each side of the SUSY decay (one "side" referring to the decays originating from one of the pair-produced sparticles) motivates the grouping of the associated final state particles into so-called "mega-jets," denoted j_1 and j_2. All visible objects from one side of the di-squark decay are collected together to create a single four-vector, representing the decay products of a single squark. The "invisible" LSPs are neglected from this grouping procedure in addition to neutrinos, which are also not visible to the ATLAS detector.

The mega-jets are constructed by combining all reconstructed objects selected, with their four-vectors equal to the sum of the four-vectors of their constituents. There are many ways in which the selected final state objects may be combined to form mega-jets, and the decision as to which mega-jet each object is associated to is based on favouring the combination which minimises the sum of the mega-jet squared four-vector masses. Each mega-jet must contain at least one reconstructed object, and once the mega-jets are formed their masses are set to zero. This is in line with the usage of the Razor variables at CMS. The latter procedure is motivated by the fact that the masses of the final state leptons and jets comprising the mega-jets are well below the SUSY mass scale. In the example considered here, each mega-jet is comprised of a jet from the hadronisation of one of the quarks. Each squark is at rest and possesses some mass $M_{\tilde{q}}$, and their respective decays can be approximated as a simple two-body decay into a mega-jet and an LSP. In this configuration, the energy of each mega-jet in the R-frame is:

$$j_{1,E} = j_{2,E} = \frac{M_{\tilde{q}}^2 - M_{LSP}^2}{2 \times M_{\tilde{q}}}, \tag{5.1}$$

[1] Effective mass (M_{eff}) is defined as the sum of the missing transverse energy and the p_T of the four highest p_T jets in the event.

where M_{LSP} is the LSP mass. From this relation, a characteristic R-frame mass, denoted M_R, can be expressed:

$$M_R = 2 \times j_{1,E} = 2 \times j_{2,E}, \tag{5.2}$$

with $M_R \to M_{\tilde{q}}$ for $M_{\tilde{q}} >> M_{LSP}$. This results in peaks in the M_R distribution at the characteristic mass of the contributing events. For example, a $t\bar{t}$ event sample produces an M_R distribution with a peak at $M_R \approx M_{top}$, the mass of the top-quark.

The R-frames of each squark can be reached from the lab frame upon the application of longitudinal and transverse boosts, β_L and β_T^R. Neglecting any hard initial state radiation ($\beta_{ISR} = 0$), where the colliding partons emit high-p_T quarks, gluons or photons before the interaction, the di-squark centre-of-mass frame is approximately accessible following a longitudinal boost, β_L. Using the assumption that the centre-of-mass frame β_T is zero with respect to the lab frame, this boost, β_L, takes the di-squark system from the lab frame to the rest frame of the system. The approximation $\beta_T \to 0$ is assumed throughout this discussion and is motivated by the fact that $\beta_T \sim p_T^{ISR}/\sqrt{\hat{s}}$, thus in general $|\beta_T| << 1$. In the example, the squarks are produced at rest, and the R-frame has been reached as it is simultaneously the centre-of-mass frame, but in practice this is not generally the case. Each squark must undergo an additional (equal and opposite) transverse boost, β_T^R, in order to reach its R-frame. The series of boosts required to take the mega-jets back from the R-frame to the lab frame are therefore:

$$j_i^R \xrightarrow{\vec{\beta}_T^R} j_i^{CM} \xrightarrow{\vec{\beta}_L} j_i^{lab} \tag{5.3}$$

where $i = 1, 2$, and $\vec{\beta}_T^R$ is the transverse boost applied to each of the mega-jet four-vectors in opposite directions.

The requirement that the two mega-jets have equal energy in their R-frame leads to a constraint on the magnitude of their transverse boost. This constraint can be expressed as:

$$\beta_T^R = \frac{\gamma_L \times (j_{1,E} - j_{2,E}) - \gamma_L \times \beta_L \times (j_{1,L} - j_{2,L})}{\hat{\beta}_T^R \cdot (\vec{j}_{1,T} + \vec{j}_{2,T})} \tag{5.4}$$

where $j_{1,L}$ and $j_{2,L}$ are the z-components of the four momenta of the respective mega-jet, $\vec{j}_{1,T}$ and $\vec{j}_{2,T}$ are the respective mega-jet momenta in the transverse plane and $\hat{\beta}_T^R$ is a unit vector indicating the direction of the transverse boost, $\vec{\beta}_T^R$. From this M_R may be expressed in terms of the magnitude of the longitudinal boost and the direction of the transverse boost:

$$M_R = \frac{2\gamma_L \times \hat{\beta}_T^R \cdot [(j_{1,E} \times \vec{j}_{2,T} + j_{2,E} \times \vec{j}_{1,T}) - \beta_L \times (j_{1,L} \times \vec{j}_{2,T} + j_{2,L} \times \vec{j}_{1,T})]}{\sqrt{|\hat{\beta}_T^R \cdot (\vec{j}_{1,T} + \vec{j}_{2,T})|^2 - \gamma_L \times [j_{1,E} - j_{2,E} - \beta_L \times (j_{1,L} - j_{2,L})]^2}}. \tag{5.5}$$

Here γ_L denotes the Lorentz gamma factor associated with the longitudinal boost, β_L. When the denominator of this expression takes on negative values, the quantity M_R is no longer well defined and becomes unphysical. This behaviour of

M_R when the denominator becomes imaginary motivates the choice of the direction assigned to the transverse boost. The value of the unit vector, $\hat{\beta}_T^R$, is chosen such that the number of events for which M_R takes on real quantities is maximised with respect to the opposite. For this to be the case:

$$\hat{\beta}_T^R = \frac{\vec{j}_{1,T} + \vec{j}_{2,T}}{|\vec{j}_{1,T} + \vec{j}_{2,T}|}, \tag{5.6}$$

resulting in:

$$|\hat{\beta}_T^R \cdot (\vec{j}_{1,T} + \vec{j}_{2,T})|^2 \to 1. \tag{5.7}$$

The remaining degree of freedom, β_L, may be minimised:

$$\frac{\partial M_R}{\partial \beta_L} = 0, \tag{5.8}$$

which yields:

$$\beta_L = \frac{j_{1,L} + j_{2,L}}{j_{1,E} + j_{2,E}}. \tag{5.9}$$

Now the transverse and longitudinal boosts necessary to move from the lab-frame to the R-frame are expressed in terms of only mega-jet quantities in the lab-frame. With γ_R being invariant under longitudinal boosts, this Lorentz factor is expressed in terms of the transverse boost, $\vec{\beta}_T^R$, only:

$$\gamma_R = \frac{1}{\sqrt{(1 - |\vec{\beta}_T^R|^2)}}. \tag{5.10}$$

Using this in conjunction with Equation 5.6, the Lorentz factor describing the boost from the lab-frame to the R-frame can also be expressed in terms of lab-frame quantities only:

$$\gamma_R = \sqrt{\frac{(j_{1,E} + j_{2,E})^2 - (j_{1,L} + j_{2,L})^2}{(j_{1,E} + j_{2,E})^2 - (j_{1,L} + j_{2,L})^2 - \frac{(|\vec{j}_{1,T}|^2 - |\vec{j}_{2,T}|^2)^2}{|\vec{j}_{1,T} + \vec{j}_{2,T}|^2}}}, \tag{5.11}$$

Now from Equations 5.6, 5.9 and 5.11, M_R may also be expressed as a function of these lab-frame observables:

$$M_R = \sqrt{(j_{1,E} + j_{2,E})^2 - (j_{1,L} + j_{2,L})^2 - \frac{(|\vec{j}_{1,T}|^2 - |\vec{j}_{2,T}|^2)^2}{|\vec{j}_{1,T} + \vec{j}_{2,T}|^2}}. \tag{5.12}$$

The quantity M_R tends to peak at $M_R \sim M_\Delta$ regardless of the value of the Lorentz factor describing the boost from the lab-frame to the centre-of-mass frame, γ_{CM}. Here M_Δ is defined as $M_\Delta = \frac{M_{\tilde{q}}^2 - M_{LSP}^2}{M_{\tilde{q}}}$. The distribution of $\gamma_R \times M_R$ meanwhile, tends to peak at $\gamma_R \times M_R \sim \gamma_{CM} M_\Delta$. Due to the way in which M_R is defined, it is best suited for instances where $\gamma_{CM} = 1$, which is unphysical kinematically, and therefore, forbidden. By using $\gamma_R \times M_R$ in place of M_R, the same peaking behaviour is seen in the variable's distribution, while the number of unphysical mega-jet configurations is minimised. For this reason this analysis chooses to use the quantity $\gamma_R \times M_R$, which is defined from Equations 5.11 and 5.12 as,

$$\gamma_R \times M_R = \sqrt{(j_{1,E} + j_{2,E})^2 - (j_{1,L} + j_{2,L})^2}. \tag{5.13}$$

From Equation 5.13, the quantity $\gamma_R \times M_R$ can be seen to contain only longitudinal information about the event. The transverse information of the system is presented in another variable, M_T^R. In the di-squark example above there are two mega-jets, each with associated E_T^{miss} from the escaping LSPs. Assigning half of the event's missing transverse momentum to each of the LSPs, M_T^R is defined as,

$$M_T^R = \sqrt{\frac{|\vec{E}_T^{miss}|(|\vec{j}_{1,T}| + |\vec{j}_{2,T}|) - \vec{E}_T^{miss} \cdot (\vec{j}_{1,T} + \vec{j}_{2,T})}{2}}. \tag{5.14}$$

Comparing M_T^R with $\gamma_R \times M_R$, it also contains information regarding the scale of the process. In the example of di-squark production with $\gamma_{CM} = 1$, the distribution of M_T^R has a kinematic end-point at M_Δ. Sources of fake E_T^{miss} can include dead read-out modules in the detector, or hadronic punch-through where high p_T jets leak through to the muon system. Scrutiny of Equation 5.14 shows that in instances where the missing transverse momentum in an event points towards one of the mega-jets, and so towards the reconstructed final state objects, the quantity M_T^R becomes small. Such a configuration is suggestive of punch-through or the final states particles traversing dead material. Standard E_T^{miss}-based searches may pick up such events in the high-E_T^{miss} tails of their distributions, whereas the same events would be situated at low M_T^R. The quantity M_T^R is therefore apparently insensitive to contributions from "fake" E_T^{miss}.

There are now two independent variables which offer a description of the mass scale of the physics process in question. Using these two sources of information together, the R-frame "Razor," R, is defined as the ratio of these two variables:

$$R = \frac{M_T^R}{\gamma_R \times M_R}. \tag{5.15}$$

For SM processes R tends to take on low values, with R being more or less uniformly distributed between 0 and 1 for SUSY-like signal events. This feature of R makes it an excellent signal-background discriminant, and background reduction can be achieved by imposing a lower bound on this variable in order to select events. The scale-indicator, $\gamma_R \times M_R$, is also used to select signal-like events. Imposing a high threshold on $\gamma_R \times M_R$ will tend to isolate SUSY with high mass-splitting, given the peaking nature of this variable. The distributions for an example background and signal process in the $\gamma_R \times M_R - R$ plane are shown in Figure 5.1. Notice that the Standard Model Z+jets background is mostly contained at low R and $\gamma_R \times M_R$, while the SUSY signal point shows no such trend.

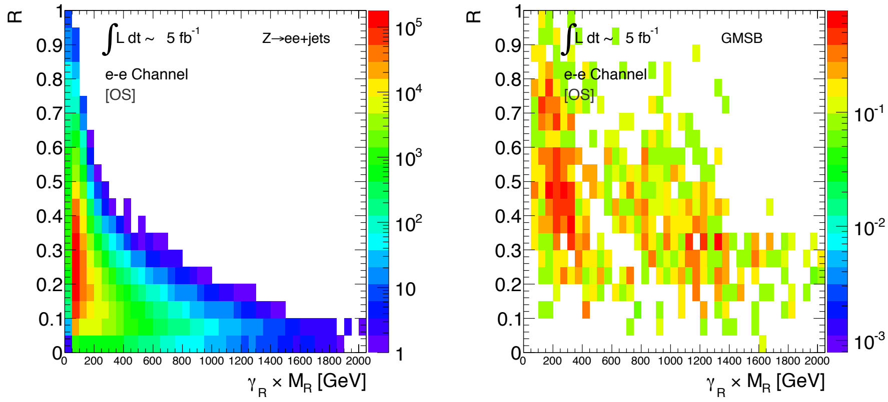

Figure 5.1: Correlation distributions in R and $\gamma_R \times M_R$ for opposite sign $Z/\gamma^* \rightarrow ee$+jets events (left) and di-electron events from a SUSY signal point (right). The SUSY model is a GMSB signal point with parameters $\Lambda = 40$ and $\tan\beta = 15$. This signal model is described in more detail in Section 6.1.1.

5.2 Razor Correlations

The Razor variables have themselves been designed in order to isolate and study physics processes involving massive particles created in pairs, which decay thereafter into SM particles and a weakly interacting particle escaping detection, the latter being characterised by missing transverse momentum in the event. This variable set is novel in many ways, though still the variables display some strong correlations with other quantities in common use in many SUSY and new physics searches. Here the Razor variables are shown with respect to some more familiar variables employed in particle physics analyses, to better understand their behaviour and characteristics.

The transverse event information is stored in the M_T^R variable, with half of the E_T^{miss} in the event being assigned to each of the escaping LSPs. When the E_T^{miss} vector is pointing in the direction of a mega-jet, M_T^R will be small compared with E_T^{miss}. For cases with real E_T^{miss}, however, Equation 5.14 suggests that M_T^R should be highly correlated with E_T^{miss}. The distributions in Figure 5.2 show the correlation between $E_T^{miss}$and M_T^R in opposite sign (OS) di-lepton events resulting from Standard Model $Z/\gamma^* \rightarrow e^+e^-$+jets and a representative SUSY signal point. Notice that these variables are more correlated in the case of signal, since there exists real E_T^{miss}. On introducing cuts on R the correlation becomes stronger as events become more signal-like. This behaviour can be seen in both signal and background distributions.

Longitudinal event information is stored in the $\gamma_R \times M_R$ variable, which tends to peak close to M_Δ, and as such acts as an indicator of the characteristic mass scale of the event. Other standard SUSY-finding variables provide similar information, like H_T for example. Here, H_T is defined as the scalar sum of the p_T of all jets (Section 4.1.3) with $p_T > 20$ GeV in the event. The correlation between these variables in the absence of, and upon applying, cuts on R is shown in Figure 5.3. For Z+jets events, high H_T values most often result from the collision of two partons where one has a high momentum-fraction (fraction of total proton momentum) and the other with a low momentum-fraction. This indicates an initial longitudinal energy imbalance, and so the final state products are boosted in the z-plane. In cases such as these the events are not symmetric in the detector, with the majority of the final state products confined to one side of the detector in η. This configuration will result in low values of $\gamma_R \times M_R$ and R. In contrast, signal like events (as well as a significant fraction of background events) will appear more symmetric in the detector, especially in the case of two heavy particles being produced at (or almost at) rest. In these instances $\gamma_R \times M_R$ will not be small, and since $\gamma_R \times M_R$ is related to the energy of the reconstructed objects (as opposed to transverse quantities like p_T, as is the case with H_T), $\gamma_R \times M_R$ can sometimes be significantly larger than the corresponding H_T values. As one would expect, Figure 5.3 shows that these variables become more strongly correlated as the R threshold increases and events exhibit more signal-like characteristics.

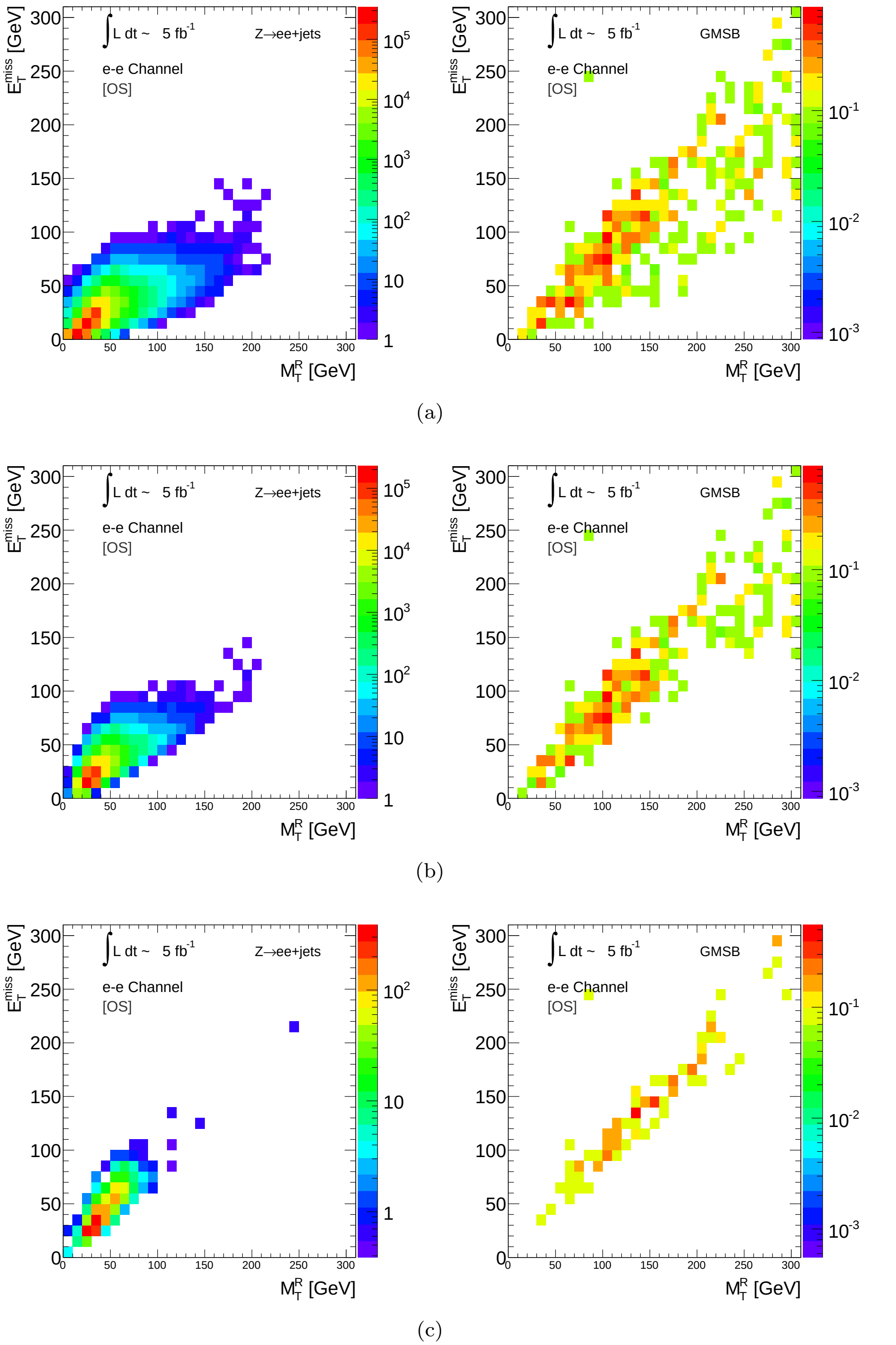

Figure 5.2: Correlation distributions in $E_T^{miss}$and M_T^R for opposite sign $Z/\gamma^* \rightarrow ee$+jets events (left) and di-electron events from a SUSY signal point (right) with $R > 0$ (a), $R > 0.25$ (b), and $R > 0.6$ (c). The SUSY model is a GMSB signal point with parameters $\Lambda = 40$ and $\tan\beta = 15$. This signal model is described in more detail in Section 6.1.1.

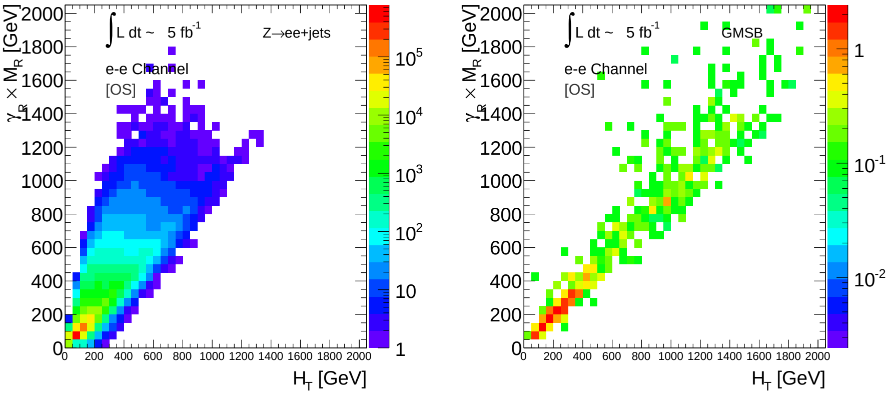

(a)

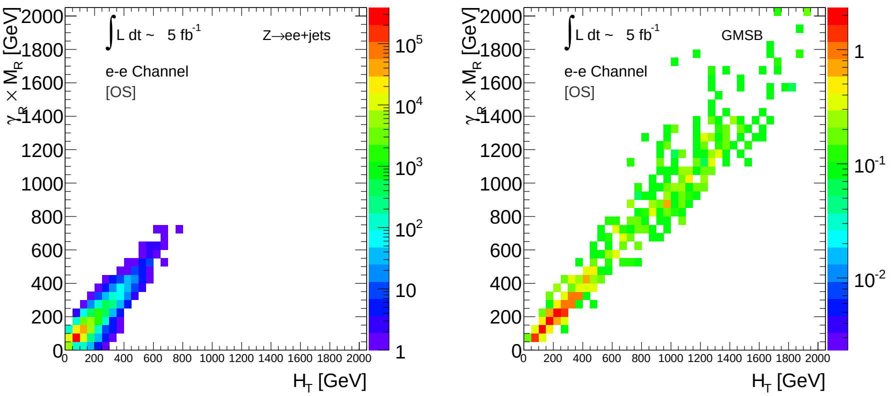

(b)

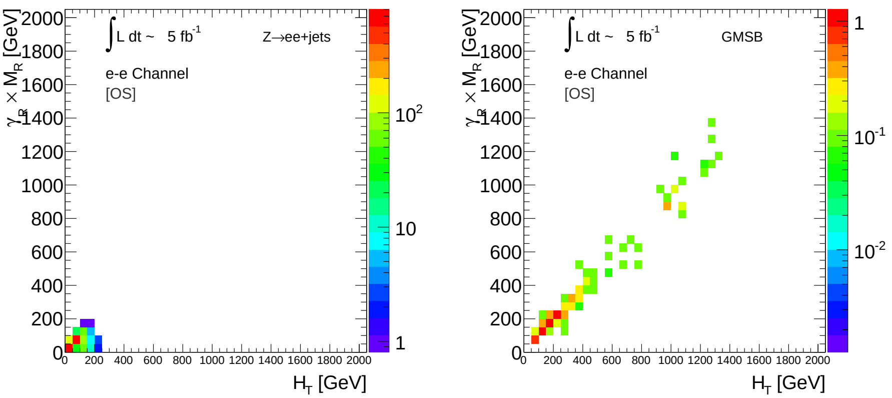

(c)

Figure 5.3: Correlation distributions in $\gamma_R \times M_R$ and H_T for opposite sign $Z/\gamma^* \rightarrow ee$+jets events (left) and events from a SUSY signal point (right) with $R > 0$ (a), $R > 0.25$ (b), and $R > 0.6$ (c). The SUSY model is a GMSB signal point with parameters $\Lambda = 40$ and $\tan\beta = 15$. This signal model is described in more detail in Section 6.1.1.

Chapter 6

Di-Lepton Analysis

The SUSY Razor analysis at ATLAS [44] makes use of the nature of these variables to search for SUSY in multiple final states. The concept of the Razor is useful in that the variables themselves are constructed upon grouping final state particles into mega-jets. Constructing the variables in this way allows these discriminants to be defined globally, independent of the channel. This is in contrast to variables such as H_T, for example, which requires jets in the final state. The Razor analysis uses zero-, one- and two-lepton final states. The combination of these channels results in a SUSY search that is more inclusive than those generally performed at ATLAS. This report focuses on the two-lepton final state only, though in practice this channel is combined with the zero- and one-lepton Razor search to maximise its reach.

This analysis has been structured as a search for evidence of SUSY in di-lepton final states. On imposing a di-lepton selection on the data taken in 2011, a sample of all detected and reconstructed events including exactly two-leptons[1] is formed. SUSY signatures must be filtered out from the overwhelming volume of Standard Model background processes. The Razor variables are employed to assist in this filtering process.

Following a procedure standard to SUSY analyses, cuts are placed on these variables, requiring that selected events lie beyond the enforced thresholds. The aim is to reject as much background events as possible, without an unacceptable number of events from potential signal models being sacrificed. This results in a signal rich region – called a "signal region" (SR) – to be defined as a selection region within which all tailored cuts are satisfied. It is in this region that the postulated signal model is searched for in data, and the background contribution from Standard Model processes must be estimated.

Various Monte Carlo generators are used to manufacture the centrally generated, official ATLAS signal and background event samples. The specific signal scenarios in use are outlined in 6.1, along with the procedure and results of the

[1]An event is required to include exactly two signal leptons according to the definitions in Sections 4.1.1 and 4.1.2.

signal region definition and optimisation process. The SM backgrounds relevant to a di-lepton selection are introduced in Section 6.2, with the various Monte Carlo generators used to produce simulated event samples outlined in Section 6.2.2. Section 6.3 contains details on the background estimation procedures employed for all SM backgrounds associated with this analysis. Though the simulation provides an estimate of the contribution in the given event selection from SM background processes, control samples dominated by specific backgrounds are used to provide background estimates based on distributions in data. These so-called "data-driven" estimations are performed on every background for which it is viable. This is discussed further in Section 6.3.

6.1 Signal Models and Signal Region Optimisation

In order to fine tune signal region cut thresholds, a single signal model point in parameter space is chosen as the "test" signal. For this analysis, a GMSB point lying just outside the 2.05 fb^{-1} ATLAS limit [45] is used. A scan over the Razor variable parameter space is performed facilitating the selection of the threshold values yielding the most generous signal significance.

In order to quantify the significance of the predicted signal contribution in the proposed signal regions, a quantity of signal significance is defined as follows:

$$N_\sigma = S/\sqrt{B} \tag{6.1}$$

Here S denotes the number of signal events, and B the number of background events in the considered region. N_σ, then, describes the number of standard deviations the observed signal is from the combinatory background; an approximation appropriate in the case of $S << B$. It is this quantity that is used to determine which regions of Razor variable parameter space offer the best signal significance enhancement.

The expected sensitivity to the GMSB and mSUGRA models probed in this analysis is presented in the following sections, with the signal regions being optimised for a signal point in the GMSB parameter space. Also included are details on two different gluino-gluino pair production simplified models. These models were selected for use in the Razor analysis due to the possibility of zero-, one- and two-lepton final states offered. Additionally, centrally produced ATLAS samples were readily available for use.

6.1.1 GMSB

The primary signal model chosen for the focus of this analysis is a minimal gauge-mediated supersymmetry breaking model, and as such the signal region definitions result largely from the performance of the selections on a test point from a grid point in the GMSB model parameter space. The GMSB signal grid probed in this search is one resulting from varying the values of $\tan\beta$ and Λ, creating a 2-Dimensional parameter space over which to scan. The other model parameters remain fixed, with this particular grid being characterised with a messenger mass, M_{mess}, of 250 TeV, $\mu > 0$ and $C_{grav} = 1$. The number of messenger multiplets, N, is set to 3. At these parameter values the next–to–lightest SUSY particle (NLSP) is a slepton (selectron or smuon) or a stau. The point chosen to optimise for lies in the slepton region at $\tan\beta = 15$, $\Lambda = 40$, lying just beyond the limit of the 2011 2.05 fb^{-1} ATLAS exclusion reach. A summary of associated parameters, including the leading order (LO) cross–section for this point, are shown in Table 6.1.

N	3
M_{mess}	250 TeV
μ	> 0
C_{grav}	1
$\tan\beta$	15
Λ	40 TeV
NLSP	$\tilde{\ell}$
σ (LO)	0.39 pb

Table 6.1: List of GMSB model parameters for the signal point selected for optimisation of the di-lepton signal regions.

The $\frac{S}{\sqrt{B}}$ distributions as a function of $\gamma_R \times M_R$ were studied. The di-lepton final states are split into a total of six channels, one for each of the possible flavour and sign combinations. The resulting distributions in the $R - \gamma_R \times M_R$ plane can be seen in Figure 6.1. For the opposite-sign (OS) final states $\frac{S}{\sqrt{B}}$ is maximised at R values of 0.4 or slightly above. Placing a threshold at $R > 0.4$ results in $\frac{S}{\sqrt{B}}$ values in the $\gamma_R \times M_R$ tails ($\gamma_R \times M_R >\sim 600$ GeV) of approximately 4σ. In general the possible significance in the same-sign (SS) channels is much higher, reaching over 20 even at low R thresholds. For this reason the threshold can be chosen to be lower. Since less SM background is expected for same-sign processes and a non-zero number of background events is desired in the signal region in order to make a reliable estimation of the background contribution therein, the R-threshold is selected such that not all background events are rejected.

The signal region definitions are based on the GMSB $\frac{S}{\sqrt{B}}$ optimisation, and are shown in Table 6.2. These regions will also be used to search for other SUSY models, outlined further in this section.

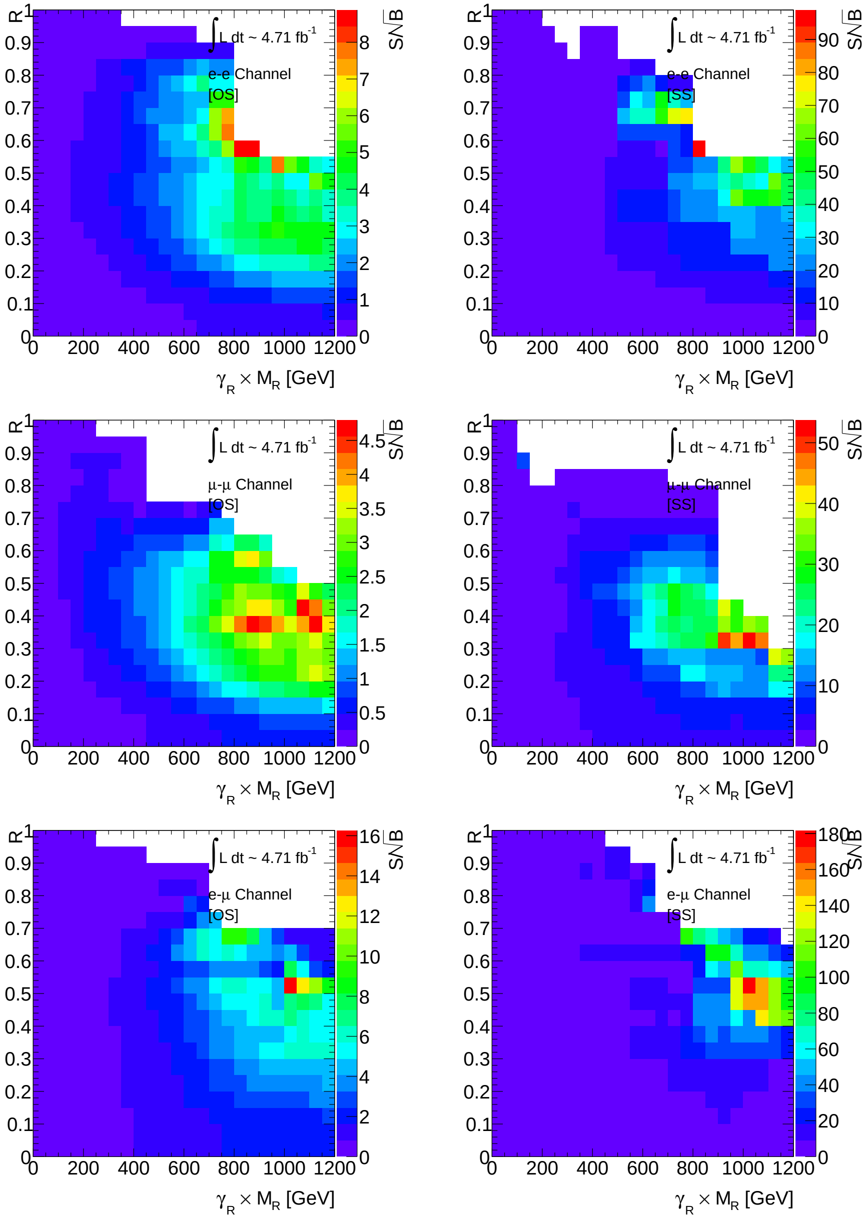

Figure 6.1: The ratio $\frac{S}{\sqrt{B}}$ as a function of inclusive $R - \gamma \times M_R$ cuts for the OS (left) and SS (right) ee, $\mu\mu$ and $e\mu$ channels. The signal model is a GMSB signal point with parameters $\Lambda = 40$ and $\tan\beta = 15$.

6.1.2 mSUGRA

The constrained supersymmetric standard model (cMSSM) assumes universality of masses and couplings at very high energies. These constraints on the MSSM reduce

Flavour Combination	Sign Combination	R Threshold	$\gamma_R \times M_R$ Threshold
electron – electron	OS	> 0.4	> 600 GeV
muon – muon	OS	> 0.4	> 600 GeV
electron – muon	OS	> 0.4	> 600 GeV
electron – electron	SS	> 0.25	> 500 GeV
muon – muon	SS	> 0.25	> 500 GeV
electron – muon	SS	> 0.25	> 500 GeV

Table 6.2: Signal region definitions according to the $\frac{S}{\sqrt{B}}$ based optimisation. In practice the R thresholds are applied to define the signal regions and SUSY-like events are searched for in the $\gamma_R \times M_R$ tails.

the number of associated parameters to five, thus simplifying the model considerably. In contrast to the GMSB the cMSSM is a minimal SuperGravity model (mSUGRA), where SUSY breaking is mediated by gravitational interactions. Limits are set on mSUGRA, and the signal significance as a function of R and $\gamma \times M_R$ is studied for a chosen point in the mSUGRA parameter space. The standard ATLAS mSUGRA signal grid is generated using Herwig [46], which is an MC generator described in Section 6.2.2, with NLO cross-sections from Prospino [47]. Three of the five mSUGRA parameters are fixed, with the grid being produced in the m_0 – $m_{1/2}$ plane. The other associated parameter values are $\tan\beta = 10$ and $A_0 = 0$ GeV with the sign of μ being positive.

A point at $m_0 = 340$ GeV and $m_{1/2} = 330$ GeV is taken to study the signal significance resulting from various R thresholds, again a point just beyong the two-lepton exclusion limits set by ATLAS dilepton analyses on early 2011 data. The resulting distributions are shown in the $R - \gamma \times M_R$ plane in Figure 6.2. The significance in the OS channels is lower than is the case for the GMSB model of Section 6.1.1, particularly in the di-muon channel. In general it appears that higher R-thresholds are desirable in order to maximise the sensitivity to a signal of this type in the OS channels. For the SS channels the potential signal significance is higher, though if the optimisation were to be done for this model perhaps the R-thresholds would need to be raised in order to gain the best sensitivity.

6.1.3 Simplified Models

Simplified models characterise new physics signatures in terms of the final state objects resulting from sparticle decays. Limits are set on two simplified models with gluino pair production. In the first of these models the gluinos decay, with a branching ratio of 100%, to a $t\bar{t}$ pair and an LSP. The final state resulting from such a topology involves a large number of soft jets, obviously including heavy flavours. The mass splitting between the gluino and the LSP must be rather large since the decay chain involves a top-quark. In fact, since the gluino must be on-shell, only points which satisfy $m_{gluino} > m_{LSP} + 2 \times m_{top}$ are considered. The simplified model grid is generated using Herwig++ [48] with the gluino and LSP masses

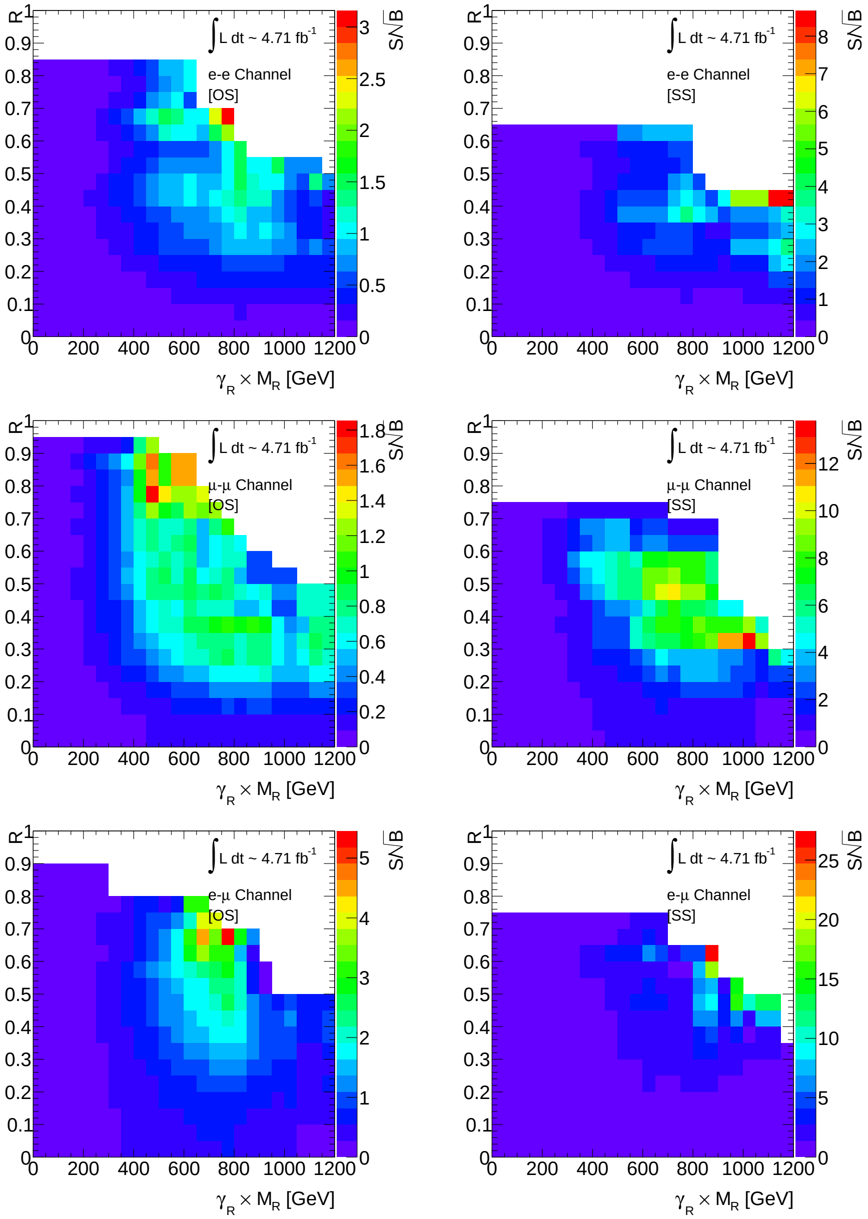

Figure 6.2: The ratio $\frac{S}{\sqrt{B}}$ as a function of inclusive R - $\gamma \times M_R$ cuts for the OS (left) and SS (right) ee, $\mu\mu$ and $e\mu$ channels. The signal model is an mSUGRA signal point with parameters $m_0 = 340$ GeV and $m_{1/2} = 330$ GeV.

being varied.

An additional interpretation is made using another model where the gluinos follow a one-step decay to the LSP. The gluino decays, via the emission of two quarks, to a chargino, with the chargino subsequently decaying into a $W^{\pm}$ and an LSP. The associated model parameters are the LSP and gluino masses, along with the relative chargino-LSP, gluino-LSP mass splittings. This simplified model grid is generated using MadGraph [49].

6.2 Standard Model Backgrounds and Monte Carlo Generators

In this Section the important backgrounds relevant to a di-lepton search are introduced and discussed. The simulation of these backgrounds, based on the current understanding of the Standard Model, is performed using an assortment of event generators. The MC generators responsible for the simulation of each of the SM backgrounds are identified, along with an explanation as to how the simulation models the behaviour expected of these processes within the ATLAS detector.

6.2.1 Standard Model Backgrounds

A variety of SM processes can produce two final state leptons. Different processes dominate depending on lepton flavour and sign combinations. The backgrounds considered for this analysis are listed in Table 6.3 along with their respective cross–sections and k-factors. The k-factor for a given process is the ratio of the NLO to LO cross–section predictions.

The background due to leptonically decaying Z–bosons (or off–shell photons) is an important contribution for same-flavour, opposite-sign lepton channels. A Feynman diagram of one such process is shown in Figure 6.3a. The Z/γ^{*}+jets background samples used in this analysis include $Z/\gamma^{*} \to ee, \mu\mu, \tau\tau$ processes, as well as processes containing heavy flavour (HF) jets ($Zbb/Zcc \to ee, \mu\mu, \tau\tau$). Final states containing two leptons of the same sign are far rarer than processes producing OS leptons in the SM. In fact $Z \to e^{+}e^{-}$ is also one of the dominant backgrounds in the case of the di-electron SS channel, where one of the electrons has had its charge mis-identified.

For both the opposite-flavour and same-flavour channels, $t\bar{t}$ and single top events are prominent backgrounds. An example of a same-flavour $t\bar{t}$ process can be found in Figure 6.3b. The cross-section for $t\bar{t}$ is the highest compared to all the other background processes considered here, but the branching ratio of 4.9% for top – anti–top pairs to decay into two prompt leptons in the final state means that it is not the dominant background. Additional contributions arise from semi-leptonic $t\bar{t}$, where only one of the tops decay leptonically, with the jet resulting from the hadronic decay of its partner – or any other jet in the event – being incorrectly reconstructed as an electron. The latter example results in the selection of a “fake” lepton, an effect that can lead to single lepton events being wrongly categorised as di-lepton events. It is this feature that necessitates the consideration of the background due to W+jets, where one of the jets fakes a lepton. A discussion of the

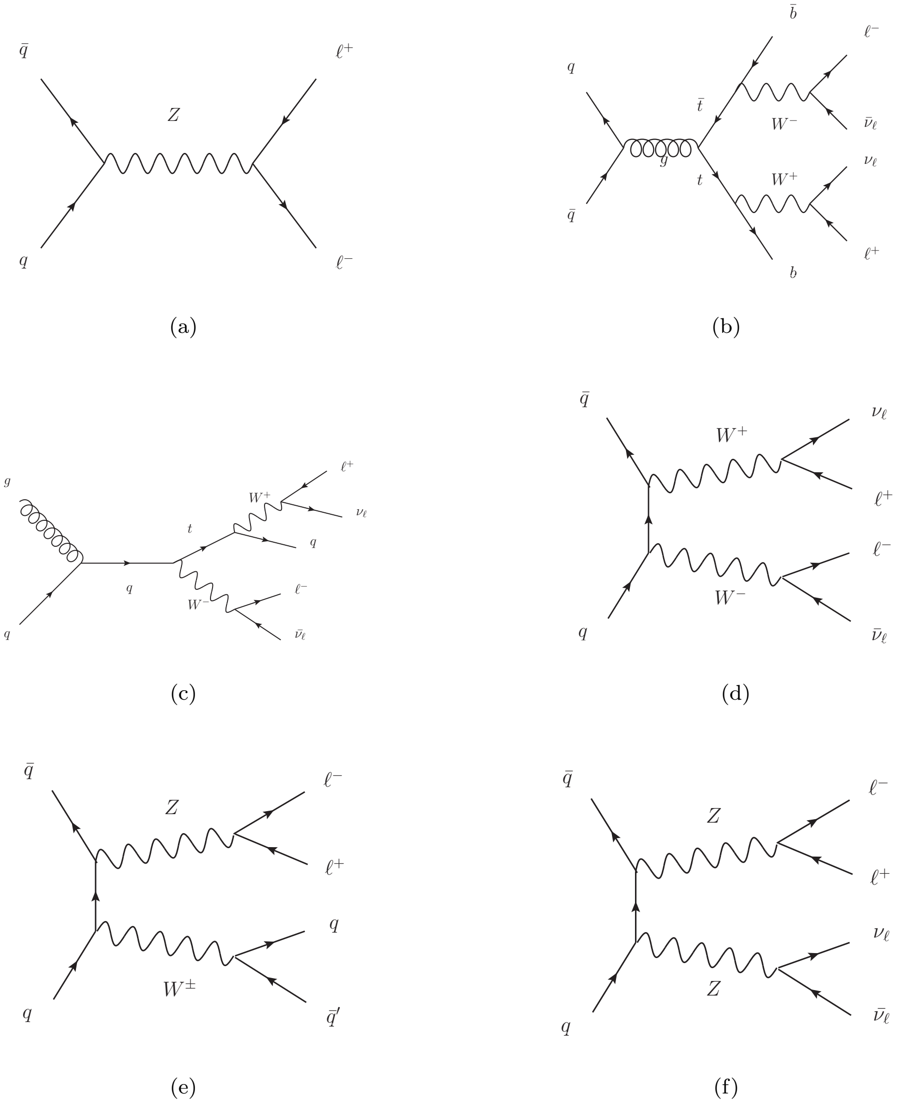

Figure 6.3: Feynman diagrams of SM process with possible di-lepton final states; $Z/\gamma^* \to \ell\ell$+jets (a), $t\bar{t}$ (b), single top (c), WW (d), WZ (e) and ZZ (f).

fake lepton background and its determination can be found in Section 6.3.2. Single top production can leave signatures similar to $t\bar{t}$ events, and in Figure 6.3c there is an example of a single top event resulting in two final state leptons. The presence of a neutrino in an event leads to real missing energy, providing a hint as to how single top processes can enter into signal–like selections.

The background due to diboson production has a far smaller cross-section compared with $t\bar{t}$. Despite this, the diboson background is important, since final states with two real leptons are possible, and often the diboson background is strikingly similar to SUSY–like signal. Diboson processes involving WZ and ZZ production can result in two real prompt leptons from a leptonically decaying Z, as illustrated in Figures 6.3e and 6.3f. This leaves the other Z, or W depending on the production mode, to decay hadronically. It could also happen that one of the leptons in $WZ \rightarrow \ell\ell\ell\nu$, is missed during the object reconstruction. This is also possible in the case of ZZ, though in that case two of the total of four leptons in the event would have to be missed. For WW, two leptons are produced if both W's decay leptonically as in Figure 6.3d, though there is still the possibility of leptons being incorrectly identified from the remnants of a W having undergone a hadronic decay.

6.2.2 Monte Carlo Generators

In high–energy physics, events are simulated using Monte Carlo generators. These computational algorithms use random numbers to determine the result of a particle interaction. This makes them especially useful for predicting the outcome of situations with many associated degrees of freedom for which the computation of an exact result is infeasible. There exist a variety of MC generators, and generally the generator is chosen based on its suitability for the process considered. All samples used in this analysis are centrally produced by the ATLAS Collaboration.

MC generators use the parton model of the proton, with the momentum shared between constituent partons, following a parton distribution function (PDF). The process of interest is defined by the user. To find the parton level cross-section the hard-scattering process is modelled, and this modelling normally includes some higher order corrections (eg. parton radiation). In general most generators will also include a description of initial state radiation (ISR) in their simulation, in addition to final state showers and hadronisation. Also the underlying event, a term describing all interactions and processes except for the hard-scattering, is generally included in MC simulations. Some generators are also capable of including NLO cross-section calculations.

Pythia [50] is a widely used MC generator that is capable of simulating both hard and soft interactions. It is a multi-purpose generator in that it includes parton showering, hadronisation, particle decays and underlying events, as well as the evaluation of matrix elements. This is all within the Pythia framework, and as such this is a generator that provides a complete event view. The matrix elements for 2 initial state partons $\rightarrow 1, 2, 3$ final state parton processes in the Pythia samples used in this analysis are provided by MadGraph [49]. MadGraph is a dedicated matrix element generator and provides all Feynman diagrams for a specified process. Pythia coupled with MadGraph is used to produce simulated $t\bar{t}$ plus vector boson samples and the WW plus two-jet samples for this analysis. This is also the case for the simplified models.

Herwig (Hadron Emission Reactions With Interfering Gluons) is an event generator that simulates hard-scattering for almost any $2 \rightarrow 2$ process. The matrix elements are evaluated to first order, with parton showers and hadronisation also being described in the simulation. HERWIG is paired with JIMMY, with HERWIG being responsible for simulating the parton showers and hadronisation and JIMMY taking care of multi-parton interactions. HERWIG calculates leading-order cross-sections and these are scaled to NLO using k-factors. This generator is responsible for the samples representing the diboson background for this analysis. Some of the SUSY signal samples are produced using HERWIG++[2]. In the case of the signal samples, cross-sections for SUSY processes are provided by PROSPINO, a LO and NLO SUSY cross-section calculator.

ALPGEN [51] is a more specialised tree level matrix element generator capable of generating events with high jet multiplicities. Where PYTHIA evaluates matrix elements for up to $2 \to 2$ processes, ALPGEN can do this for up to $2 \to 6$. ALPGEN is used to produce the background samples for $t\bar{t}$ and $Z+$ jets in this analysis, and in order to gain a full picture of the event ALPGEN is interfaced with JIMMY. It is the JIMMY event generator that adds the description of the underlying event, with the multiple parton matrix element being provided by ALPGEN. Here k-factors are still needed to scale the LO cross-sections to NLO (and to NNLO in the case of the $t\bar{t}$ samples).

Finally the background due to single top is simulated using MC@NLO [52] (Monte Carlo At Next to Leading Order). The MC@NLO framework makes use of HERWIG and JIMMY in order to combine generated events with full NLO cross-sections calculations, making the use of k-factors unnecessary.

Simulating events using one of the MC generators described above results in a very good approximation to the processes expected upon parton collisions within the ATLAS detector. This implies that, in an "ideal" detector - implying that it is capable of identifying and reconstructing exactly every particle - the result should be the same as the content provided by the MC at this level. In fact the detector is not perfect and the generated physics events output by these generators must be run through a simulation of the ATLAS detector in order to gain a realistic representation of how these processes might manifest. GEANT4 [53,54] is a toolkit for simulating the passage of particles through matter and is used to simulate how the final state objects of physics processes might interact with the detector material. Once events have been generated and passed through the detector simulation they are run through dedicated reconstruction algorithms which are used to build physics objects and calculate event level variables used in physics data analysis. These algorithms are exactly those run on real collision data.

6.3 Background Estimation Methods

In order to perform a search for SUSY in the signal regions defined for this analysis, an estimate must be made regarding the number of events expected in that signal region in the presence of SM background only. The MC samples for the various

[2] This is a new implementation written in $C{+}{+}$ that will ultimately replace HERWIG.

Process	Generator	$\sigma\times$ BR [pb]	k-factor
Z/γ^*+jets	AlpgenJimmy	12.1×10^3	1.24
Z+HF	AlpgenJimmy	70.61	1.24
Single top	MC@NLO Jimmy	37.34	-
$t\bar{t} \to \ell\nu\ell\nu$	AlpgenJimmy	10.38	1.69
$t\bar{t}$ $+W/Z/WW$	PythiaMadgraph	0.221	1.30
$WWjj$	PythiaMadgraph	0.22	-
WW	Herwig	11.50	1.26
WZ	Herwig	3.464	1.26
ZZ	Herwig	0.972	1.26

Table 6.3: List of Standard Model background samples used in the di-lepton Razor analysis, with respective production generators, cross-sections and k-factors.

backgrounds outlined in Section 6.2.1 are used as an initial check. Looking at the background sample distributions in the different regions provides an estimate when optimising the signal regions, as in Section 6.1, for example. Once the signal regions are selected, a more rigorous check of the background is performed. Such checks often involve comparing the MC distributions to those from data in predefined, background–rich, control regions (CR). In this way any discrepancies between data and MC can be identified and must be understood. In most cases the background estimation is be made using data itself rather than the MC - though in practice the MC usually enters at least as a cross-check, and so such estimates are rarely completely independent of simulation. Estimates are taken from data where ever technically and statistically feasible. Once the behaviour of each background is understood in the control region, and the MC – or data-driven control region distributions – are in good agreement with the data distributions in the same regions, an extrapolation is performed between the control region and the signal regions. For this extrapolation the expected background distribution in the signal regions is derived. This procedure normally employs a transfer factor (control region $\rightarrow$ signal region), calculated from simulation.

In this analysis, the majority of backgrounds are estimated from data, or MC that has been validated using data-driven methods. The use of the HistFitter package [55] is key for estimating the background components in the SRs. HistFitter is a fitting suite, which performs fits on multiple background distributions in various control regions, and ultimately propagates the fit results to the signal regions, providing a final background estimate. More information on this package and how it is configured for this analysis can be found in Section 6.3.1. This Section describes the techniques used to estimate the background due to the different SM processes in the SR, along with the various validations performed on these estimates.

6.3.1 Simultaneous Background Fit

HistFitter provides a framework which allows shape analysis of distributions, resulting in an insight into their implications by way of full statistical interpretations. This package is based on the HistFactory framework [56], a tool used to build probability density functions (pdfs) using analysis histograms. In this section the implementation and configuration of HistFitter used for this analysis is described.

HistFitter generates histograms for different control and signal regions. These are then organised in XML files from which pdfs are built. The pdfs include a number of different parameters, some of which are "free parameters" in the sense that they are unconstrained. These free parameters act as scaling factors, and can be adjusted freely in the fit, altering the relative contributions from the various component signal or background processes. The statistical and systematic uncertainties are represented by so-called "nuisance parameters." These generally carry Gaussian penalty terms of predetermined width. During the fit the shape of the MC distributions are varied within the boundaries allowed by the nuisance parameters. In this respect the fit fine tunes both the MC and the associated uncertainties.
Provided the fit is not overly constrained the nuisance parameters merely serve to propagate the uncertainties, and so only the free parameters should be adjusted. In practice, if the fit is over-constrained then these nuisance parameters are adjusted to prevent inconsistencies between prediction and data arising from unreasonable variations in the predicted distributions. In this case the penalty term associated with the nuisance parameter increases with the magnitude of deviation from its nominal value, increasing the uncertainty on the fit.

The HistFitter input is divided into different regions, with the region categories being control regions (CR), signal regions (SR) and some validation regions (VR). Validation regions are defined to be disjoint from both the CRs and SRs, and are used for some backgrounds to validate the extrapolation from CR to SR. Using a background fit to data in the CRs the result of the fit is applied to the VR to confirm that the fit models the data well outside of the constraints of the CRs.

The fit parameters are constrained by performing a so-called "background only" fit to the CRs. Note that all CRs are fit simultaneously, and so they all constrain one another. This is made possible by the fact that all regions are statistically independent, permitting their combination. The nuisance parameters associated with various systematic uncertainties can be treated in several different ways in the fit. In this analysis the systematic uncertainties are predominantly treated as "shape" systematics correlated across all bins of the histogram. Cross-section uncertainties affect the overall integral of the distributions, with their effect being evaluated upon varying the normalisation of the relevant histograms by $\pm 1\sigma$. Such uncertainties do not use the shape information. The sources of systematic uncertainty on physics objects are discussed in detail in Section 6.3.7.

The SM backgrounds as input to HistFitter are split into the following samples:

- Fake leptons
  This includes the totally data-driven fake lepton background sample as de-

scribed in Section 6.3.2. The uncertainty is dominated by the weights applied to the events from data comprising the fake background sample. No control regions for the fake background are defined since the background is estimated from data in the control and signal regions.

- Lepton charge flip
  This is comprised of leptons whose charge have been mis-reconstructed. This background is estimated as described in Section 6.3.3 and is only significant in the same-sign di-electron and electron-muon channels. The dominant uncertainty is that associated with the charge flip probabilities.

- Z+X
  This sample includes $Z+$ jets with both heavy and light flavour quarks, low mass Drell-Yan processes and finally the WZ and ZZ diboson backgrounds. The inclusion of these diboson processes in the $Z+X$ sample is motivated by the fact that Z-bosons are found to decay only leptonically in the signal regions. This is shown in Section 6.3.4.

- $t\bar{t}$ and single top
  The backgrounds due to single top and $t\bar{t}$ processes follow the same distributions in R and $\gamma_R \times M_R$. It therefore makes sense to merge these backgrounds into one sample for HistFitter, since the histograms will be fit in bins of $\gamma_R \times M_R$, with regions being defined in R. Since no validation is performed outside of HistFitter three separate top control regions are defined, as described in Section 6.3.5, to ensure the top background is well constrained. The normalisation is allowed to float freely in the fit.

- WW Diboson
  This background, discussed in Section 6.3.6 does not pose a significant contribution to the signal region expectation. Since it does not have a large presence in the control regions, it is constrained by a 30% cross-section uncertainty. This is to avoid giving the fit too much freedom by leaving the normalisation unconstrained.

6.3.2 Fake Leptons

A di-lepton event selection requires events containing exactly two leptons in the final state. It is important to consider the success rate of this selection, since the ability of ATLAS to successfully detect and accurately reconstruct leptons is dependent on so many factors, from the detector read-out electronics to the clustering and reconstruction algorithms.

To quantify the extent to which successful reconstruction and identification is achieved, two main quantities are considered. Firstly, there is the efficiency with which leptons are identified in ATLAS, the identification efficiency. This quantity describes the fraction of all real leptons that pass the loose selection requirements. The electron identification efficiency is measured at ATLAS in $Z \rightarrow ee$ events in bins of p_T and η [26]. It is typically over 90% for electrons with $p_T > 20$ GeV. For muons, $Z \rightarrow \mu\mu$ events from the 40 pb^{-1} of $\sqrt{s} = 7$ TeV 2010 data are probed in order to measure the efficiency, which is determined to be more than 96%.

Secondly, the lepton "fake rates" must be considered. These describe the probability that a lepton candidate is reconstructed when no real lepton is in fact present. This most commonly happens with jets being mis-identified as electrons. Similarly, jets which "punch through" into the muon system could potentially fake muons. More commonly though, muons can originate fron pions or kaons decaying in-flight as they traverse the ATLAS detector. Such muons are usually poorly isolated, but can sometimes still pass the signal muon isolation requirements. For a di-lepton selection the most common SM processes contributing to the fake lepton background are $W+$ jets and semi-leptonic $t\bar{t}$, which are mainly fake electrons.

In order to predict the fake lepton background to a di-lepton selection a matrix method [57] is used. For an inclusive single lepton selection, the number of events containing a single signal lepton (N_T) and the number of events containing a single baseline, but not signal, lepton (N_L) can be related to the true number of real (N_R) and fake (N_F) leptons:

$$N_T = r \cdot N_R + f \cdot N_F, \tag{6.2}$$

$$N_L = (1-r) \cdot N_R + (1-f) \cdot N_F. \tag{6.3}$$

where f is the fake rate for a fake loose lepton to pass the tight signal lepton criteria, and r is the efficiency with which a real loose lepton is reconstructed as a tight lepton. This results in the 2×2 matrix relation:

$$\begin{vmatrix} N_T \\ N_L \end{vmatrix} = \begin{vmatrix} r & f \\ (1-r) & (1-f) \end{vmatrix} \begin{vmatrix} N_R \\ N_F \end{vmatrix}. \tag{6.4}$$

In this way the true event composition of real and fake leptons can be derived using a control sample of events passing signal-like cuts, but with baseline leptons. For the di-lepton case, an event will be composed of either two real leptons (R), two fake leptons (F), or one of each. An inclusive sample would therefore include events with the p_T-ordered lepton real-fake combinations: RR, RF, FR, FF. The relation described in Equation 6.4 is expanded to the di-lepton case, resulting in a 4×4 matrix relating the possible loose-tight combinations to the real-fake event composition. The full matrix is given below.

$$\begin{vmatrix} N_{TT} \\ N_{TL} \\ N_{LT} \\ N_{LL} \end{vmatrix} = \begin{vmatrix} r_1 r_2 & r_1 f_2 & f_1 r_2 & f_1 f_2 \\ r_1(1-r_2) & r_1(1-f_2) & f_1(1-r_2) & f_1(1-f_2) \\ (1-r_1)r_2 & (1-r_1)f_2 & (1-f_1)r_2 & (1-f_1)f_2 \\ (1-r_1)(1-r_2) & (1-r_1)(1-f_2) & (1-f_1)(1-r_2) & (1-f_1)(1-f_2) \end{vmatrix} \begin{vmatrix} N_{RR} \\ N_{RF} \\ N_{FR} \\ N_{FF} \end{vmatrix}. \tag{6.5}$$

In the above equation the numbered subscripts refer to the r and f values for the leading (1) and sub-leading (2) leptons. On inverting this matrix, one acquires an estimate for the real-fake composition of a sample of inclusive baseline di-leptons. In order to determine the true composition for the signal lepton sample, the numbers derived from the matrix inversion must be corrected by the corresponding real efficiencies and fake rates:

$$\begin{aligned} N_{RR}^{signal} &= r_1 r_2 \cdot N_{RR} \\ N_{RF}^{signal} &= r_1 f_2 \cdot N_{RF} \\ N_{FR}^{signal} &= f_1 r_2 \cdot N_{FR} \\ N_{FF}^{signal} &= f_1 r_2 \cdot N_{FF}. \end{aligned} \tag{6.6}$$

The total number of fake di-lepton events contributing to the tight di-lepton selection (N_{events}^{fake}) is therefore described by the sum of events containing at least one fake lepton:

$$N_{events}^{fake} = N_{RF}^{signal} + N_{FR}^{signal} + N_{FF}^{signal}. \tag{6.7}$$

The number of fake di-lepton events contributing to the signal sample can be defined in terms of the real-fake event composition (Equations 6.7 and 6.5), and therefore the tight-loose event composition (Equation 6.6). Di-Lepton events taken from a control sample containing at least one baseline (and not signal) lepton are weighted by the probability for such an event to fall into the signal selection, with the matrix method permitting the determination of these event-by-event probabilities, or "fake weights." For electrons, a control sample is constructed of events passing signal-like cuts, but with one or more baseline electron failing the isolation or tight electron requirements. For muons, the control sample is composed of events where at least one baseline muon fails the isolation cut. These samples, populated with di-lepton events where at least one lepton is not a signal lepton, are disjoint from the main selections that are composed of events with exactly two signal, or tight, leptons. A fake weight is derived for each event in the loose-not-tight lepton samples, and the events are then weighted accordingly. This method is applied to data, not MC, and so the matrix method is extremely useful in that it allows for a data-driven approach to the fake background determination. Because this background is taken completely from data and accounts for all fake background, MC events passing the di-lepton signal selection must not be fakes. These are therefore required to have at least two prompt leptons from a tau, W-boson, Z-boson or SUSY particle. This ensures that there is no MC contribution to the fake background filtering into the signal selection.

6.3.3 Charge Mis-identification

In di-lepton regions where the leptons are of the same sign there is a considerable contribution charge flip. The term "charge-flip" refers to the situation where an electron (positron) is reconstructed as a positron (electron). The lepton has been correctly identified, but the charge is incorrect. Of course this process is independent of charge combination, and there will be some events with two SS leptons entering the OS lepton selection also. In the SM, processes resulting in exactly two isolated like-sign leptons are far more rare than those where the lepton pairs are OS. For this reason the background due to charge flip is negligible in the OS channels, but rather significant in the case of SS, as will be shown in this section.

The charge flip process is perhaps most obvious in the di-electron channel, where a Z mass peak is observed despite the necessity for leptons from a decaying Z-boson to really be oppositely charged. In these events one of the oppositely charged final state leptons has had its charge mis-identified, and so an opposite sign event is reconstructed as same sign. There are two main scenarios that can result in charge flip. Firstly, the charge of an electron can be mis-measured when a high-p_T electron has a nearly straight track, making it difficult to determine the curvature. Alternatively, if a high-p_T electron undergoes bremsstrahlung, the emitted photon can pair produce. This so-called "trident" process can result in the reconstruction of a single prompt lepton from the three-lepton system. The charge of this reconstructed lepton can then be the opposite of the original lepton charge. Additionally, the p_T for these electrons tends to be mis-reconstructed, and so when modelling this process the p_T of the offending electron must be artificially smeared. This process is not as prominent in the muon channels. In the case of a high-p_T muon, while it is possible that the ID track maybe be mis-measured the additional information provided by the muon system makes charge mis-reconstruction less common. Muon bremsstrahlung will most likely result in the muon being poorly isolated, overlapping with one of the electrons produced by the bremmed photon. It is this effect that motivates the electron – muon overlap removal procedure described in Section 4.1.4. Charge flip, then, is a relevant background in the ee and $e\mu$ SS channels.

From Ref. [58] it is noted that the charge flip in data is approximately 80% that in Monte Carlo. This disagreement is clearly visible in the left of Figure 6.4. The probability for an electron to undergo charge flip is both η and p_T dependent. In Ref. [59] the electron charge flip rate as a function of η is measured in data, with the lesser dependence on p_T still being modelled in Monte Carlo. Using the results of this study, charge flip probabilities are applied to OS events from MC in the ee and $e\mu$ channels, providing an estimate of the overall contribution from charge flip in these channels.

In the $e\mu$ channel events are weighted by the probability for the electron in the event to undergo charge flip. The p_T of the electron is then smeared to mimic the effect of charge mis-identification. In the di-electron channel, the probability that one of the electrons in the event charge flips is applied to the event weight. Of the two electrons, one is chosen at random to be the charge flip electron, and its p_T shifted accordingly. Ultimately, charge flip event weights represent the probability for an event to change from OS $\rightarrow$ SS. The charge flip contribution from MC events must then be subtracted by vetoing events in the SS channels with two OS leptons at truth level. The shift in the p_T of charge flip electrons is propagated through to the razor variables, which are recalculated using the charge flip electron p_T. The effect of this correction for the same sign electron channel, which is most sensitive to charge mis-identification, can be seen in Figure 6.4.

Overlap with Fake Estimate

In order to estimate the background due to fakes in the same sign di-lepton channels the matrix method is used. Some fraction of these same sign events in data with

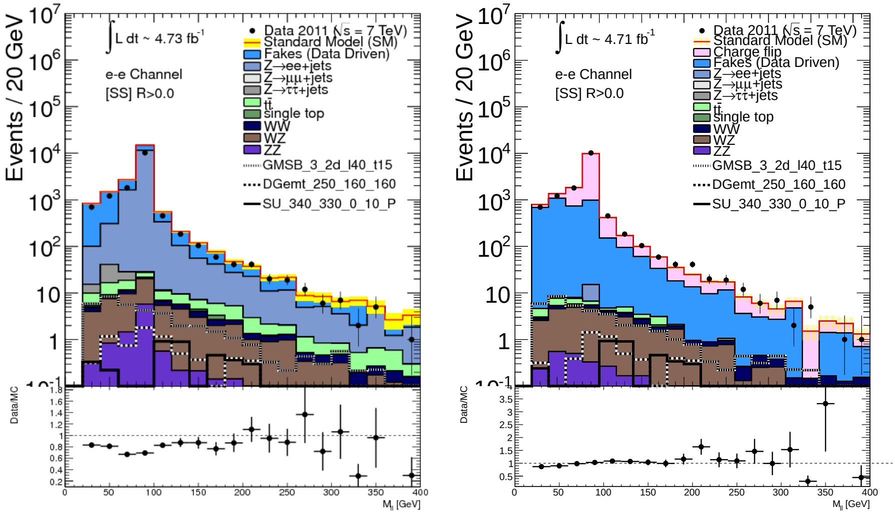

Figure 6.4: Distribution in $M_{\ell\ell}$ for the same sign di-electron channel before (left) and after (right) the of correction the charge flip background contribution.

loose electrons may also be charge flip events. If an electron undergoes charge flip it tends to be poorly isolated which can result in charge flip electrons "faking" a fake. These events must be disentangled to avoid an over-estimate. In order to correct for this overlap, opposite sign events in data containing "loose" leptons with "reversed" isolation requirements are used. The charge flip probability for these events is determined using the method above, such that each event is assigned an event weight representing the likelihood of that event being subject to charge misidentification. These weighted events are then presented as a negative component to the same sign fake background distribution, such that the contribution to the same sign fake background from originally opposite charged leptons is subtracted. The effect of this subtraction in the SS di-electron channel can be seen in Figure 6.4.

Charge Flip Background Estimation

The charge flip distributions obtained using the methods discussed above are used in order to estimate the expected background due to charge flip in the signal regions. To do this a charge flip control region is defined within HistFitter. This region is chosen so that the maximum contribution is due to charge flip, and so it makes sense to look in the same-sign di-electron channel. The control region is defined as shown in Table 6.4. The control region distribution is fit to data in 100 GeV bins in $\gamma_R \times M_R$. Figure 6.5 shows the distribution before and after the fit. The charge flip background is initially underestimated, most notably in the first three bins in $\gamma_R \times M_R$. After the fit this discrepancy becomes far less extreme, with all bins seeing agreement between data and expectation within one sigma. In fact it is the fake background that increases after the fit, rather than the charge flip background component. The fake weight uncertainties give this background some freedom in the fit. Since the fake background is entirely data driven, it is treated as uncorrelated between each control region, and is not subject to the same constraints as the other backgrounds. The uncertainty on the charge flip weights assigned to the OS events (as described earlier in this section) contributes one of the most significant systematic uncertainties associated with the background estimations.

Channel	Signal Region	Control Region
$e^{\pm}e^{\pm}$	$\gamma_R \times M_R > 500,\ R > 0.25$	$\gamma_R \times M_R > 500,\ R < 0.25$

Table 6.4: Control region definition for the charge flip background estimation in the same-sign di-electron channel.

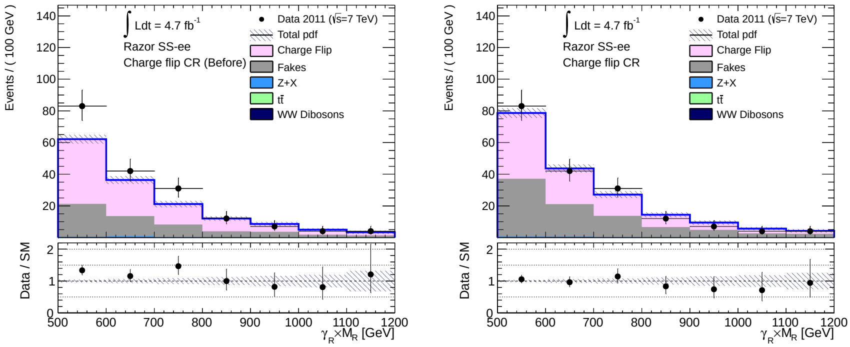

Figure 6.5: Distribution in $\gamma_R \times M_R$ for the charge flip control region both before (left) and after (right) the fit to data.

6.3.4 Z+X

In the two-lepton opposite flavour channels the background due to leptonically decaying Z-bosons is expected to be zero, due to the necessity for lepton number conservation. For same flavour - same sign lepton channels any leptonic Z contribution is due to charge flip of one of the leptons, and as such this background is accounted for by the charge flip estimate in Section 6.3.3. For the same flavour - opposite sign di-lepton signal regions a partially data driven approach is used to estimate the contribution of backgrounds with a leptonically decaying Z-boson. As such, this method estimates the background from $Z/\gamma^* \rightarrow e^+e^-, \mu^+\mu^-$, as well as WZ and ZZ processes. The validity of including WZ and ZZ in the $Z + X$ background determination is discussed later in this section. Z-control regions are defined to resemble the signal regions as closely as possible, thus the OS $\gamma_R \times M_R$ cut at 600 GeV is kept in place while the R cut at 0.4 is inverted. This allows background rich control regions (low R) while ensuring no $\gamma_R \times M_R$ bias. The signal regions and corresponding control regions are listed in Table 6.5.

In this method $Z/\gamma * +$ jets events are isolated by subtracting the non-Z contribution in the control region. The quantity of non-Z events is derived by exploiting

Channel	Signal Region	Control Region
e^+e^-	$\gamma_R \times M_R > 600,\ R > 0.4$	$\gamma_R \times M_R > 600,\ R < 0.4$
$\mu^+\mu^-$	$\gamma_R \times M_R > 600,\ R > 0.4$	$\gamma_R \times M_R > 600,\ R < 0.4$
$e^\pm\mu^\mp$	$\gamma_R \times M_R > 600,\ R > 0.4$	$\gamma_R \times M_R > 600,\ R < 0.4$

Table 6.5: Control region definitions for same flavour - opposite sign Z-background estimation.

the observed event yields in data in an identical control region defined in the $e\mu$ channel. These events are assumed to be from processes not associated with a leptonically decaying Z-boson, thus the $e\mu$ channel event yields provide an estimate of the expected events from non-Z processes in the same flavour channels. There is one background to which there is an exception, and that is the background due to fakes. This estimate relies on comparing events containing real leptons from truly leptonic events. For this reason the fake background (estimated from data) is subtracted from the total data yield in each respective control region before any comparison between channels is made. Any estimate of the total non-Z contribution to the control region is therefore incomplete until the channel specific fake background is added back into the calculation. Since the identification efficiencies for electrons and muons differ, the prompt non-Z background estimate needs to be corrected in order to extrapolate between the $e\mu$ and $ee/\mu\mu$ channels. Using the number of events observed in the Z-peak in the same flavour channel control regions, the ratio of the electron and muon identification efficiencies is derived:

$$\frac{\epsilon_e}{\epsilon_\mu} = \sqrt{\frac{(N^{CR,data}_{ee,Z-peak} - N^{CR,fakes}_{ee,Z-peak}) \times L_\mu}{(N^{CR,data}_{\mu\mu,Z-peak} - N^{CR,fakes}_{\mu\mu,Z-peak}) \times L_e}}, \tag{6.8}$$

where ϵ_e and ϵ_μ are the electron and muon identification efficiencies and L_e and L_μ represent the luminosity for the ee and $\mu\mu$ channels. This permits the non-Z contribution in the same flavour channels to be estimated:

$$N^{CR,non-Z}_{ee} = \left(\frac{1}{2} \times (N^{CR,data}_{e\mu} - N^{CR,fakes}_{e\mu}) \times \sqrt{\frac{(N^{CR,data}_{ee,Z-peak} - N^{CR,fakes}_{ee,Z-peak}) \times L_\mu}{(N^{CR,data}_{\mu\mu,Z-peak} - N^{CR,fakes}_{\mu\mu,Z-peak}) \times L_e}}\right) + N^{CR,fakes}_{ee}, \tag{6.9}$$

$$N^{CR,non-Z}_{\mu\mu} = \left(\frac{1}{2} \times (N^{CR,data}_{e\mu} - N^{CR,fakes}_{e\mu}) \times \sqrt{\frac{(N^{CR,data}_{\mu\mu,Z-peak} - N^{CR,fakes}_{\mu\mu,Z-peak}) \times L_e}{(N^{CR,data}_{ee,Z-peak} - N^{CR,fakes}_{ee,Z-peak}) \times L_\mu}}\right) + N^{CR,fakes}_{\mu\mu}. \tag{6.10}$$

The estimated number of $Z + X$ events in the signal region is then:

$$N^{SR,Z}_{ee} = (N^{CR,data}_{ee} - N^{CR,non-Z}_{ee}) \times \beta \tag{6.11}$$

$$N^{SR,Z}_{\mu\mu} = (N^{CR,data}_{\mu\mu} - N^{CR,non-Z}_{\mu\mu}) \times \beta \tag{6.12}$$

where β is an extrapolation factor denoting the ratio between the event yields in the signal region and control region. This number is taken from simulated events:

$$\beta = \frac{N_{\ell\ell}^{SR,Z}}{N_{\ell\ell}^{CR,Z}}, \tag{6.13}$$

where here Z includes $Z/\gamma^* \to e^+e^-, \mu^+\mu^-$, WZ and ZZ.

	e^+e^-	$\mu^+\mu^-$	$e^\pm\mu^\mp$
Total Data CR	3760.00 ± 61.32	4640.00 ± 68.12	727.00 ± 26.96
Total Z CR (Data Driven)	3201.30 ± 63.39	4184.96 ± 70.41	-±-
Total Z CR (HERWIG MC only)	3337.58 ± 31.26	4538.91 ± 49.21	2.85 ± 0.71
β	0.000200 ± 0.000085	0.000097 ± 0.000041	-±-
Predicted Z SR (Data Driven)	0.64 ± 0.27	0.41 ± 0.17	-±-
Predicted Z SR (Herwig MC only)	0.67 ± 0.28	0.44 ± 0.19	-±-

Table 6.6: Event yields in control regions used for Z-background estimation and resulting predictions for the signal regions. The quoted uncertainties include the statistical uncertainties only.

	HERWIG (nominal)	SHERPA	ALPGEN
	e^+e^- channel		
β	0.000200 ± 0.000085	0.000349 ± 0.000091	0.000375 ± 0.000099
Predicted Z SR (Data Driven)	0.64 ± 0.27	1.12 ± 0.29	1.20 ± 0.32
Predicted Z SR (MC only)	0.67 ± 0.28	1.16 ± 0.30	1.26 ± 0.33
	$\mu^+\mu^-$ channel		
β	0.000097 ± 0.000041	0.000262 ± 0.000051	0.000335 ± 0.000067
Predicted Z SR (Data Driven)	0.41 ± 0.17	1.10 ± 0.21	1.40 ± 0.28
Predicted Z SR (MC only)	0.44 ± 0.19	1.18 ± 0.23	1.53 ± 0.30

Table 6.7: Comparison of Z-background predictions for the signal regions with when using ALPGEN, SHERPA and HERWIG MC. Estimations using HERWIG are taken as default, with the MC shape systematic being taken from ALPGEN.

From Table 6.6 the data driven and MC only estimates for the Z contribution in the signal regions are observed to be in good agreement. The SR prediction resulting from MC is consistent with the prediction from data within the statistical uncertainty. Based on these results it appears unnecessary to apply a normalisation factor to Z Monte Carlo samples. As such, the Monte Carlo provides an estimate for the almost negligible $Z/\gamma^* + X$ background contribution in the signal regions.

It should be noted that $Z/\gamma^* \to \tau^+\tau^-$ is expected to contribute identically in the same-flavour and opposite-flavour channels. As such, any $Z/\gamma^* \to \tau^+\tau^-$ contribution in the same flavour data channels would be included in the $e\mu$ channel subtraction during the validation described in this section. Motivated by the excellent agreement between data and $Z/\gamma^* \to e^+e^-, \mu^+\mu^-$ MC, this background is also taken from MC.

The background uncertainty has components from Monte Carlo and data statistics in the control region, Monte Carlo statistics in the signal region, and the difference in background estimates obtained using different Monte Carlo samples. Herwig is the MC generator used in the production of the (WZ and ZZ) diboson samples used in the estimation of the background due to $Z + X$ processes. Despite the data-driven approach taken in the validation of this background estimate, the factor taken to extrapolate from the control to signal region is calculated from Monte Carlo. To cross-check the results of this study diboson samples produced using other generators are used. Each of the two other WZ and ZZ samples, one produced from Alpgen and the other from Sherpa, yield slightly different extrapolation factors, resulting in a small change in the signal region expectation. The numbers can be seen in Table 6.7. The data-driven estimate is consistently in good agreement with the estimate taken from MC only, implying that the simulation models the normalisation of the data well. Given the apparent difference in shape, which can be seen in the di-electron distributions of Figure 6.6, between the diboson distributions resulting from Alpgen, Herwig and Sherpa, the Herwig diboson samples are used as the default. Alpgen provides the shape systematic, since it also covers the difference between Herwig and Sherpa.

Having validated the simulated Z–background, the same–flavour control regions are set within HistFitter and the distributions fit to data therein. The $\gamma_R \times M_R$ distributions are fit in 100 GeV bins in these regions, and the result of this is shown in Figure 6.7. Here the excellent agreement between data and MC is obvious even before the fit has been performed (left hand plots).

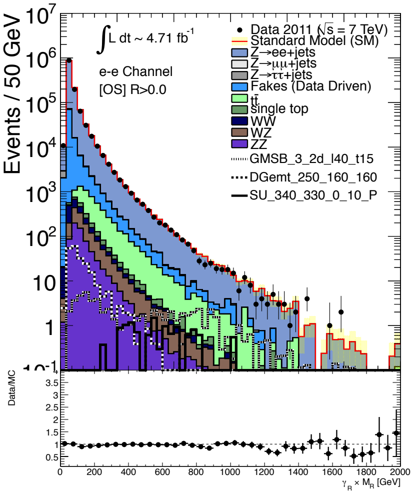

(a)

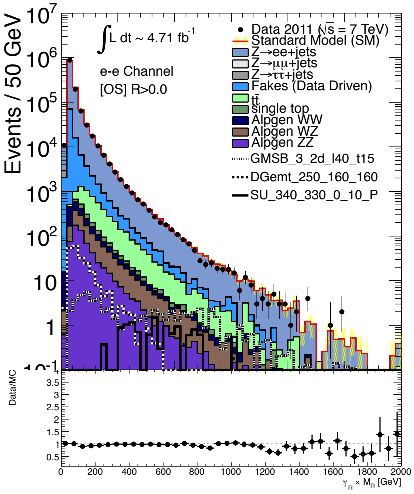

(b)

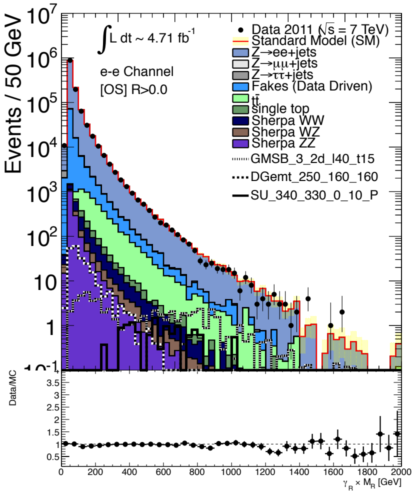

(c)

Figure 6.6: Distribution in $\gamma_R \times M_R$ (inclusive R) resulting from the use of Herwig diboson (a), Alpgen diboson (b), and Sherpa diboson (c) samples in the OS di-electron channel.

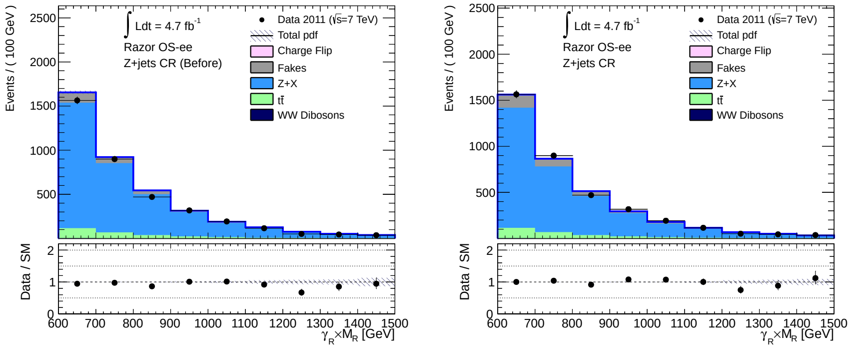

(a)

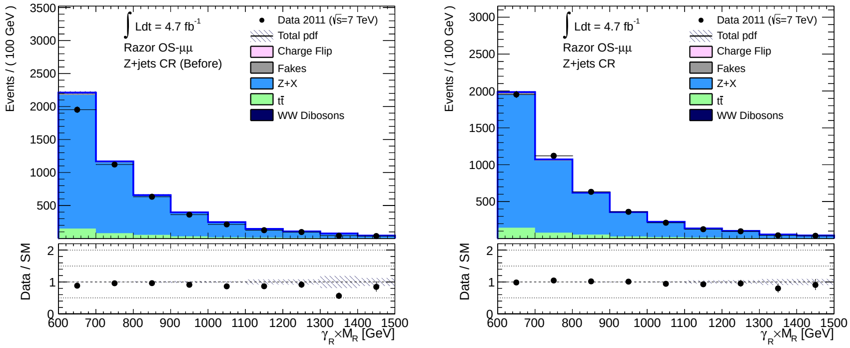

(b)

Figure 6.7: Distribution in $\gamma_R \times M_R$ for the di-electron (a) and di-muon (b) Z control regions both before (left) and after (right) the fit to data.

WZ and ZZ Contribution to the Z-Background

The diboson contribution to the Z-background from WZ and ZZ processes was studied in order to avoid overlap between background estimations. In the di-lepton channel these processes often include a leptonically decaying Z-boson, and given the method employed to estimate the Z contribution in the control (and thereafter, signal) regions, this diboson contribution becomes indistinguishable from Z/γ^*+ jets. The validity of merging these backgrounds into one $Z + X$ background estimate is determined on investigating how often WZ or ZZ events enter the signal regions due to the Z decaying into two SFOS leptons.

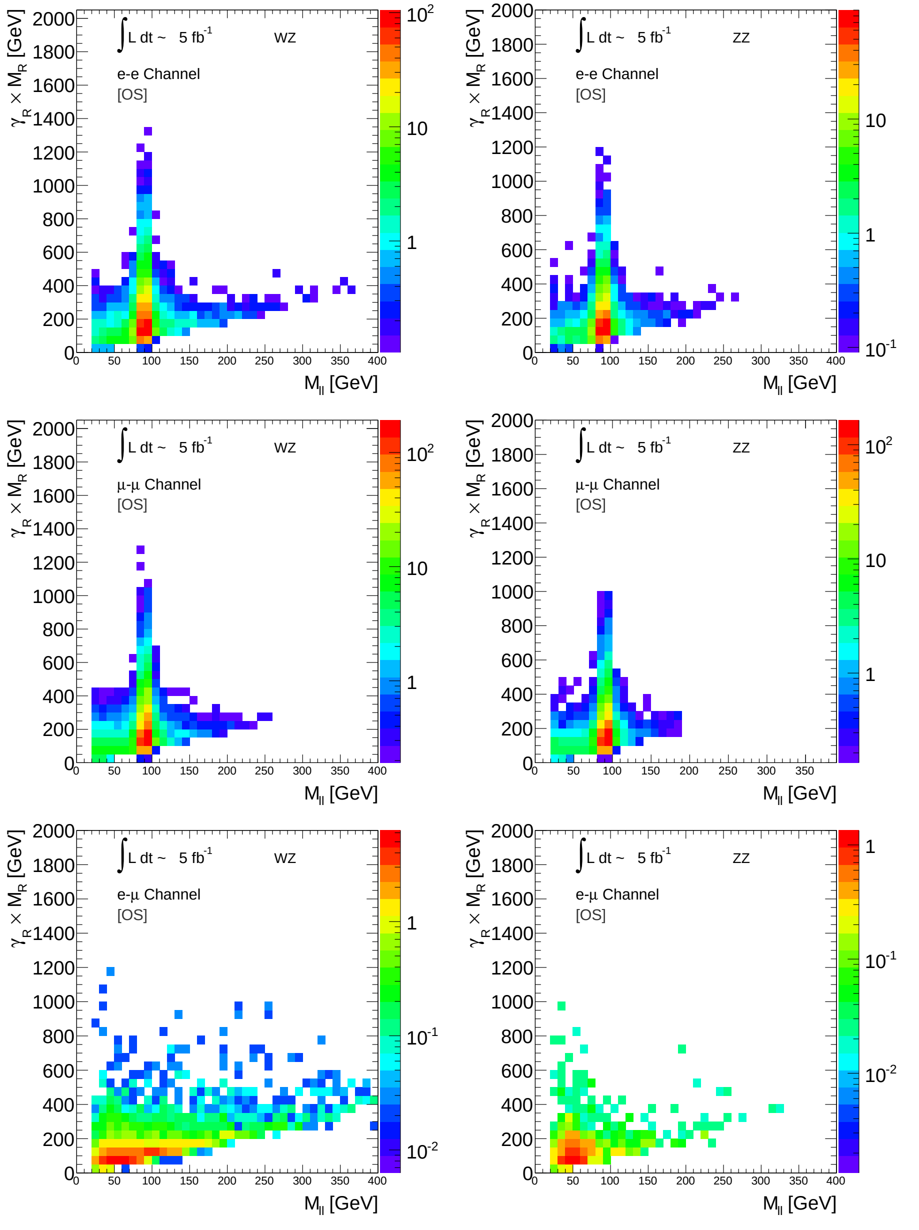

Figure 6.8: The distribution in the $\gamma_R \times M_R$ - $M_{\ell\ell}$ plane for the WZ (left) and ZZ (right) Monte Carlo in the ee, $\mu\mu$ and $e\mu$ channels.

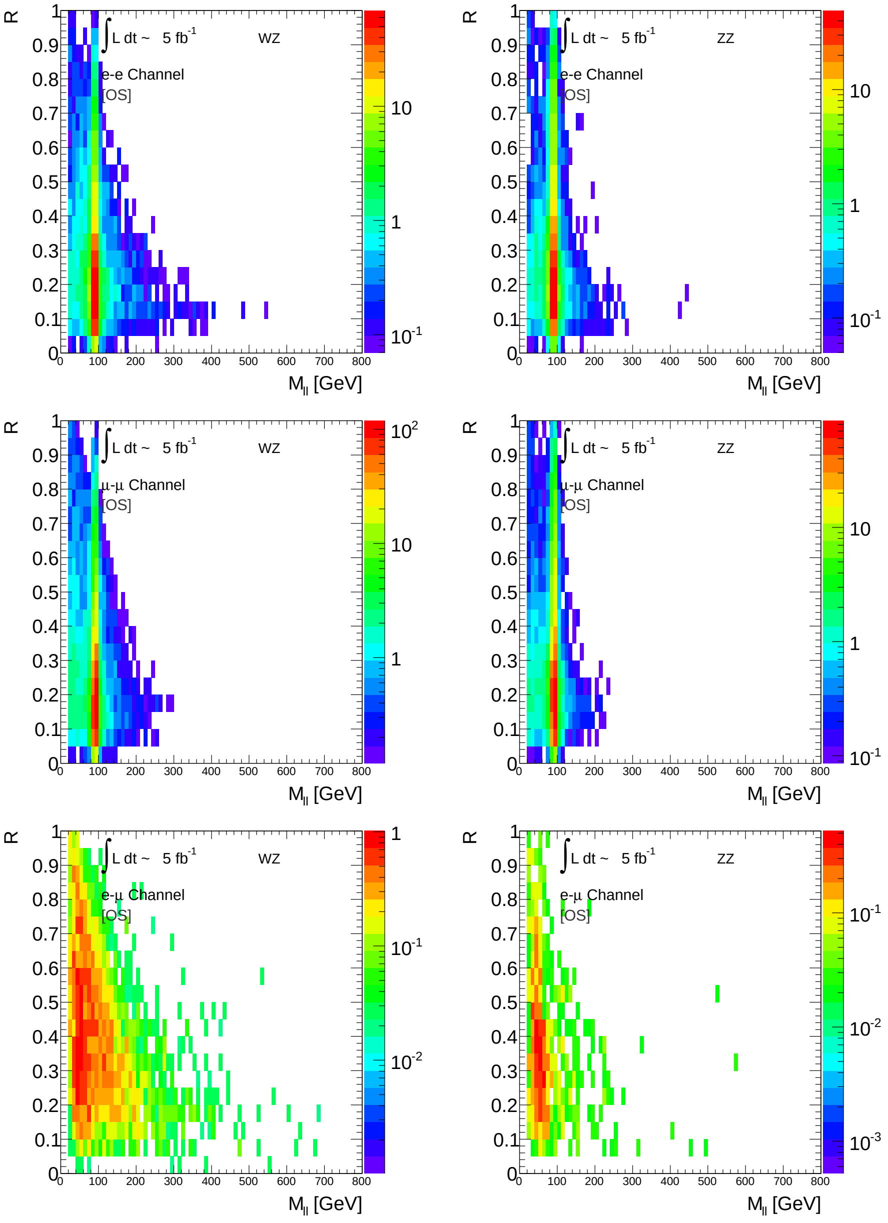

Figure 6.9: The distribution in the R - $M_{\ell\ell}$ plane for the WZ (left) and ZZ (right) Monte Carlo in the ee, $\mu\mu$ and $e\mu$ channels.

The distributions in Figure 6.8 show that on applying the signal region cuts on $\gamma_R \times M_R$, the WZ and ZZ events in the ee and $\mu\mu$ channels occur exclusively in the Z-mass peak. From Figure 6.9 it is noted that the distributions remain fairly constant in R. This confirms that any WZ and ZZ processes contributing to the same–flavour OS signal regions are expected to be Z/γ^*+ jets like. It is therefore justifiable to make a combined $Z+X$ background estimation, since the contributions from these processes in these signal regions always include a leptonically decaying Z.

6.3.5 Single Top and $t\bar{t}$

The background due to top processes is an important one for a di-lepton search. The contribution due to semi-leptonic $t\bar{t}$ and single top is accounted for in the fake background estimate of Section 6.3.2. A veto is imposed on MC events not including two prompt leptons at truth level, and so there is no double counting between the background due to semi-leptonic $t\bar{t}$ and single top fakes and fully leptonic $t\bar{t}$.

In order to estimate the background due to fully leptonic $t\bar{t}$ and single top the MC distributions are compared to those from data in several pre-defined control regions. The decision to merge the backgrounds due to these two processes into a single background estimate is motivated by the similarities in their distributions in the $R - \gamma_R \times M_R$ plane. They are almost indistinguishable from one another, and any control region defined for $t\bar{t}$ will also include a large single top component. Control regions are defined in order to isolate the top background, removing other processes as much as possible. A common method for selecting top events involves requiring b-tagged jets in the event selection. Since a top quark will decay via a b-quark (as can be seen the Feynman diagrams of Figures 6.3b and 6.3c), removing all non-heavy flavour events provides good rejection of other background processes. Three disjoint top control regions are defined, one for each opposite-sign channel. The location of these in R and $\gamma_R \times M_R$ are shown in Table 6.8.

Channel	Signal Region	Control Region
e^+e^-	$\gamma_R \times M_R > 600$, $R > 0.4$	$\gamma_R \times M_R > 400$, $0.2 < R < 0.3$, b-tag
$\mu^+\mu^-$	$\gamma_R \times M_R > 600$, $R > 0.4$	$\gamma_R \times M_R > 400$, $0.2 < R < 0.3$, b-tag
$e^\pm\mu^\mp$	$\gamma_R \times M_R > 600$, $R > 0.4$	$\gamma_R \times M_R > 400$, $0.0 < R < 0.3$, b-tag

Table 6.8: Control region definitions for the top-background estimation.

In these control regions the top MC distributions are fit to data, with the fit being done simultaneously in all three regions. The fit is performed on the $\gamma_R \times M_R$ in 100 GeV bins. The effect of the fit can be seen in Figure 6.10. The agreement, which is already typically within one sigma even before the fit is performed, is most encouraging. There is some tension between the electron and muon control regions, with the contribution to the first $\gamma_R \times M_R$ bin being overestimated in the former and underestimated in the latter. In fact, the top background does not change significantly after the fit.

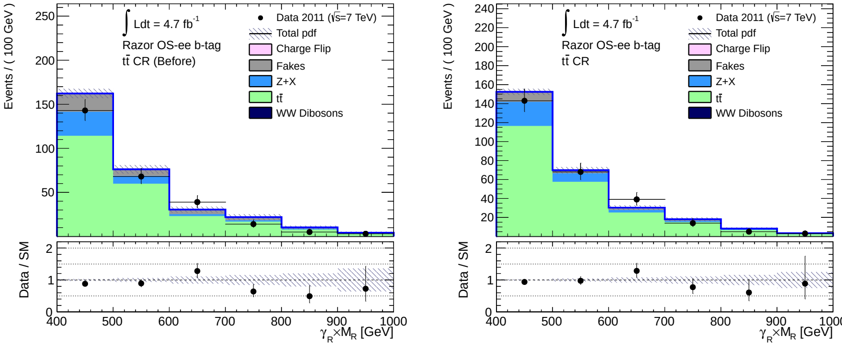

(a)

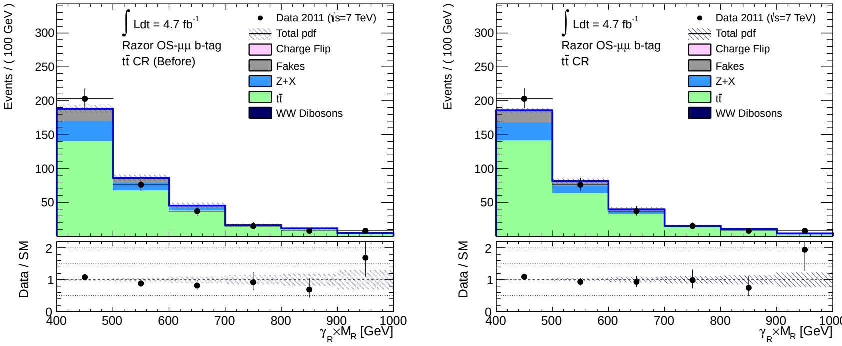

(b)

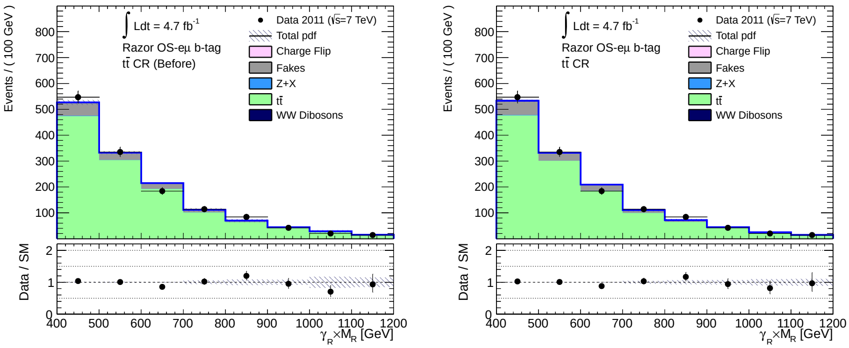

(c)

Figure 6.10: Distribution in $\gamma_R \times M_R$ for the di-electron (a), di-muon (b), and electron-muon (c) top control regions both before (left) and after (right) the fit to data.

6.3.6 Diboson

The WZ and ZZ diboson backgrounds are accounted for in the $Z + X$ estimate of Section 6.3.4, with the remaining diboson background contribution being due to

WW. Defining control regions dominated by WW diboson processes is difficult, and as a result this is the only background for which Monte Carlo is completely relied upon to provide the estimate. For this background MC samples generated by Herwig, and Pythia with MadGraph, are used with no data-driven validation methods applied. All other backgrounds are validated using data and constrained by fitting control region distributions, and so the normalisation and shape of these distributions should be well modelled. As mentioned in Section 6.3.1, the normalisation of the WW diboson MC sample is constrained by a cross-section uncertainty of 30% in order to ensure the fit does not result in a minimum with an unreasonably large amount of WW events in the signal regions. The WW diboson contribution in the signal regions is small, and so this background is not dominant in any case, though it still needs to be understood and estimated.

6.3.7 Systematic Uncertainties

There are a large number of systematic uncertainties associated with reconstructed physics objects. These uncertainties are propagated to the background fits by way of the nuisance parameters described in Section 6.3.1. The systematic uncertainties include the following:

- Luminosity
  A relative luminosity uncertainty of 3.7% is applied [37].

- Jet Energy Scale (JES)
  There is an uncertainty associated with the JES calibration of jets to the hadronic scale. Jets produced at ATLAS provide energy deposits in the calorimeters and the energy measured will not correspond to the true energy of the original quark producing the jet. The JES calibration offers a correction to the calorimeter-measured energy, scaling it to better represent the energy of the initiating quark. The uncertainty on this correction arises from many sources including calorimeter response and pile-up of events at the interaction point. An over or under-estimate of the JES can result in a different set of jets being selected for analysis since the correction is complicated in that the scaling is not the same for all jets and depends on their properties. To evaluate the effect of the JES uncertainty on the data selections this correction is fluctuated up and down resulting in separate distributions from the $\pm 1\sigma$ variations.

- Jet Energy Resolution (JER)
  In order to model the uncertainty associated with JER the energy of each jet is smeared according to a Gaussian distribution.

- Jet b-tagging
  In order to isolate heavy flavour events jets are probed for evidence of a b-quark and are (b-) tagged if they are identified as a so-called b-jet. The b-jet tagger used for this analysis works with a b-tagging efficiency of 60%. There are three separate uncertainties associated with this procedure. Firstly, some portion of the time light flavour jets will be mis-tagged as b-jets. Secondly,

jets with charm quarks are rejected from the b-jet pre-selection, and so there is an uncertainty associated with charm tagging and mis-tagging. Finally there is the obvious uncertainty associated with correctly tagging a b-jet. Each of these uncertainties are treated independently.

- Jet Vertex Fraction (JVF)
  The uncertainty associated with modelling the JVF is taken into account by applying weights of 1.2 and 0.8 to jets passing and failing the JVF cut respectively. The discrepancy between the weighted and nominal distributions represents the JVF systematic uncertainty.

- Missing Transverse Energy (E_T^{miss})
  The so-called CellOut term includes topological clusters not associated with reconstructed objects, and the components of this term are scaled up and down in order to evaluate the systematic effect. The E_T^{miss} calculation has an additional systematic uncertainty due to pile-up effects.

- Muon Resolution
  Differences in the muon resolution at ATLAS are accounted for by independently smearing the resolution in the inner detector and the muon system. The difference in the resulting distribution with respect to the nominal distribution is taken as the systematic uncertainty [29].

- Muon Scale Factors
  These scale factors are varied up and down by 1σ to provide the systematic uncertainty [28, 29].

- Electron Trigger and Reconstruction Scale Factors
  These scale factors are varied up and down by 1σ to provide the systematic uncertainty [26].

- Electron Energy Scale (EES) and Electron Energy Resolution (EER)
  The uncertainties associated with the EES and EER are applied, using central ATLAS rescaling tools [26].

Chapter 7

Results

7.1 Background Fit Results

The final estimations of the background contributions in each of the control regions are summarised in Table 7.1. The number of events before and after the the fits are shown. The fitted number of events is within 1σ of the observed in every CR. In the top control regions the fake contribution increases slightly after the fit, with there being no dramatic deviation in the top background itself. The $Z + X$ background is scaled down by the fit in both control regions, with the fake contribution again rising slightly. There is a large change in the fake background in the charge flip control region, comparing expectation with the fit results. The expected number of fake lepton events almost doubles, going from ~ 52 events before to ~ 86 after the fit. Significant uncertainties are associated with the fake background estimate, since the errors on the fake event weights are significant. In addition, the fact that this background is taken from data driven methods entirely means that it is not constrained by the control regions in the same way as the other backgrounds. This results in the background distribution having extra freedom.

The prediction for the signal regions before and after the background fit in the CRs is shown in Table 7.2. Also shown are the number of observed data events in each SR. Notice that the expected number of events in each SR before and after the fit to the CRs remain more or less the same. The fit does not have a large impact on the SR predictions in terms of the raw number of events. Of course, there is some variation in the number of events contributing from the individual background processes. The Gaussian significance shows the number of standard deviations the observed number of events is from the expected value. This is shown in Table 7.2 for each SR. Also shown is the p-value for each SR, denoting the probability of observing the number of events observed, under the background only hypothesis. After the fit all SRs are within 1σ of the expected event counts, with the only exception being the SS ee SR, which has a Gaussian significance of 1.05.

Control Region	$t\bar{t}$ ee CR	$t\bar{t}$ $\mu\mu$ CR	$t\bar{t}$ $e\mu$ CR	Z ee CR	Z $\mu\mu$ CR	Charge flip CR
Observed events	272	347	1340	3688	4579	183
Fitted background events	282.2 ± 14.5	336.9 ± 12.9	1339.9 ± 38.9	3677.7 ± 72.3	4588.5 ± 70.7	183.0 ± 13.4
Fitted top events	224.3 ± 13.1	265.6 ± 13.4	1204.6 ± 64.8	272.2 ± 23.6	343.5 ± 28.2	0.1 ± 0.0
Fitted W/Z events	39.2 ± 5.4	42.5 ± 7.1	3.0 ± 0.4	3067.4 ± 108.4	4160.3 ± 92.4	1.1 ± 0.1
Fitted WW-Diboson events	0.2 ± 0.1	0.1 ± 0.1	1.2 ± 0.4	6.2 ± 2.9	7.8 ± 4.0	1.2 ± 0.5
Fitted fake lepton events	18.6 ± 16.8	28.8 ± 0.5	131.2 ± 57.8	331.8 ± 110.0	76.9 ± 55.2	86.2 ± 19.2
Fitted charge flip events	0.0 ± 0.0	0.0 ± 0.0	0.0 ± 0.0	0.0 ± 0.0	0.0 ± 0.0	94.5 ± 14.2
Expected events	305.12	351.95	1343.19	3915.61	5048.24	148.41
Expected top events	225.28	275.77	1216.67	277.50	357.03	0.09
Expected $Z+X$ events	40.50	47.10	3.07	3359.34	4603.92	1.14
Expected WW-Diboson events	0.21	0.09	1.23	6.38	7.98	1.20
Expected fake lepton events	39.13	29.00	122.22	272.38	79.32	51.52
Expected charge flip events	0.00	0.00	0.00	0.00	0.00	94.45

Table 7.1: Background fit results for the di-lepton regions, for an integrated luminosity of 4.7 fb^{-1}. Nominal expectations (normalised to MC cross-sections in the case of MC-based estimates) are shown for comparison. The errors shown are the statistical plus systematic uncertainties.

Signal Region	OS ee	OS $\mu\mu$	SS ee	SS $\mu\mu$	OS $e\mu$	SS $e\mu$
Observed events	10	15	11	8	18	18
Fitted background events	13.79 ± 2.65	15.51 ± 2.89	5.67 ± 3.76	4.62 ± 2.89	22.18 ± 3.21	13.75 ± 8.13
Fitted top events	11.69 ± 2.13	13.34 ± 2.47	0.13 ± 0.05	0.49 ± 0.23	20.93 ± 2.95	0.62 ± 0.20
Fitted W/Z events	0.58 ± 0.11	0.47 ± 0.14	0.18 ± 0.05	0.15 ± 0.06	0.27 ± 0.05	0.35 ± 0.08
Fitted WW-Diboson events	0.35 ± 0.30	0.38 ± 0.40	0.62 ± 0.29	0.62 ± 0.40	0.43 ± 0.75	1.15 ± 0.63
Fitted fake lepton events	1.16 ± 1.26	1.32 ± 1.10	3.15 ± 3.61	3.36 ± 2.66	0.57 ± 0.57	10.60 ± 7.96
Fitted charge flip events	0.00 ± 0.00	0.00 ± 0.00	1.59 ± 0.40	0.00 ± 0.00	0.00 ± 0.00	1.04 ± 0.21
Expected events	15.27	16.03	5.74	4.72	24.18	13.81
Expected top events	13.06	14.71	0.13	0.49	22.86	0.62
Expected $Z + X$ events	0.67	0.44	0.19	0.21	0.27	0.36
Expected WW-Diboson events	0.38	0.42	0.68	0.66	0.47	1.19
Expected fake lepton events	1.16	1.32	3.15	3.36	0.57	10.60
Expected charge flip events	0.00	0.00	1.59	0.00	0.00	1.04
p_0 value	0.81	0.54	0.15	0.18	0.78	0.29
Gaussian significance	−0.88	−0.11	1.05	0.89	−0.76	0.56

Table 7.2: Background fit results for the di-lepton signal regions, for an integrated luminosity of 4.7 fb^{-1}. Nominal expectations (normalised to MC cross-sections in the case of MC-based estimates) are shown for comparison. The errors shown are the statistical plus systematic uncertainties.

Figures 7.1 – 7.6 show the $\gamma_R \times M_R$ distributions in the SRs before and after the fit. In Figures 7.1 and 7.2 the top background can be seen to move down as a result of the fit in the CRs. This effect can also be seen Figure 7.5. In these OS SRs top is the dominant background, and so this decrease in the number of expected top events as a result of the fit is most prominent. In the case of the SS SRs, which are dominated by charge flip and fakes, there is very little change after the fit.

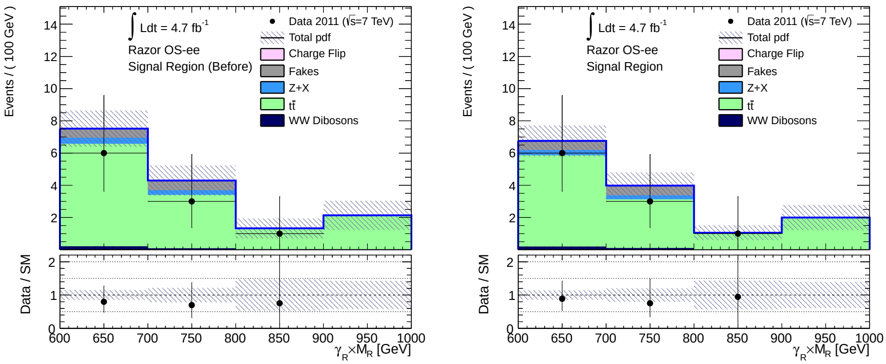

Figure 7.1: The OS di-electron signal region before (left) and after (right) the fit has been performed.

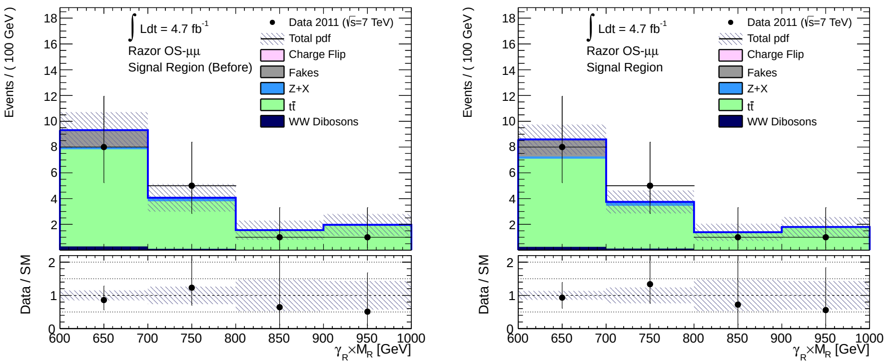

Figure 7.2: The OS di-muon signal region before (left) and after (right) the fit has been performed.

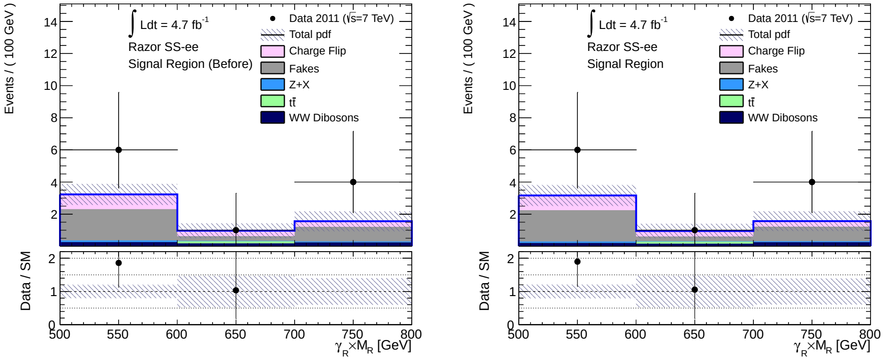

Figure 7.3: The SS di-electron signal region before (left) and after (right) the fit has been performed.

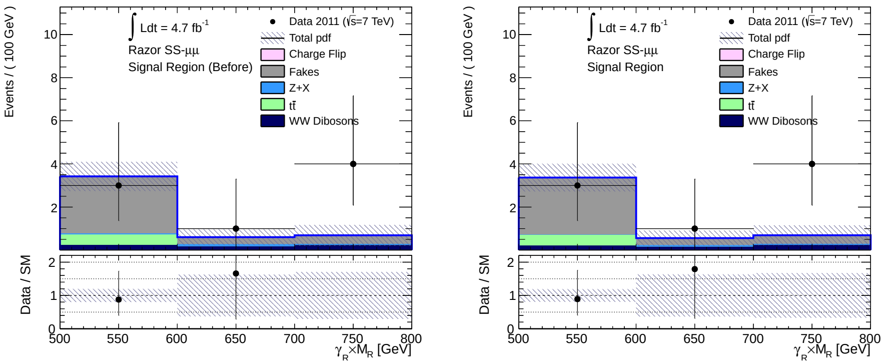

Figure 7.4: The SS di-muon signal region before (left) and after (right) the fit has been performed.

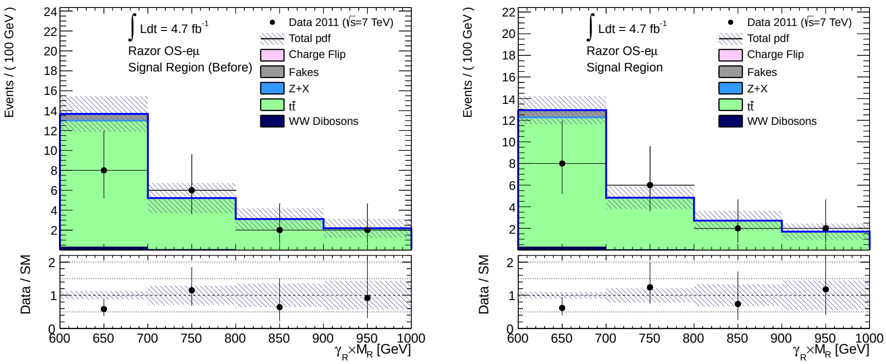

Figure 7.5: The OS electron-muon signal region before (left) and after (right) the fit has been performed.

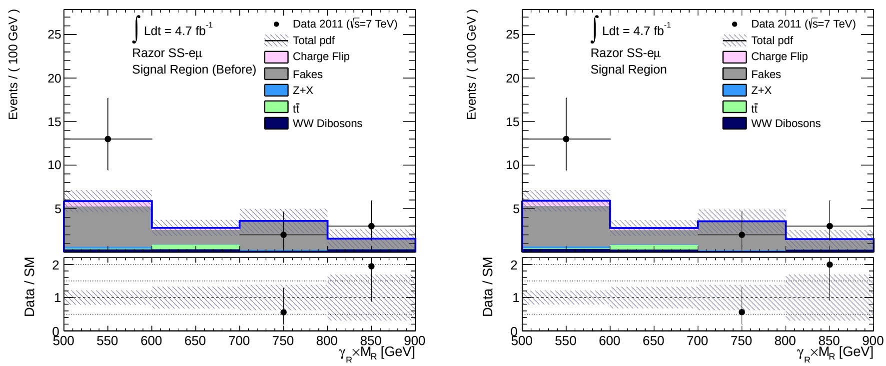

Figure 7.6: The SS electron-muon signal region before (left) and after (right) the fit has been performed.

7.2 Limits

The CL_s technique [60] is used to set limits on the production of SUSY events at 95% CL. A likelihood is constructed using the information regarding the signal shape and background contribution in the signal regions. The nuisance parameters, including their central values and widths, and their correlations are also taken into account in the likelihood. Limits are placed on the SUSY models described in Section 6.1.

7.2.1 Di-Lepton Razor GMSB Limits

Figure 7.7 shows exclusion contours in the $\tan\beta - \Lambda$ plane for the GMSB stau grid. Here the limit pushes further out in Λ where the slepton is the NLSP, with the limit contour receding slightly at higher $\tan\beta$, where the NLSP is the stau. Comparing these exclusion contours with those of other ATLAS SUSY analyses [45,61] the limit is consistent, but more specialised analyses targeting this particular signal model are able to exclude further into parameter space. As would be expected, the tau analyses [45] have better acceptance in the stau region. The SUSY strong lepton analysis [61] gains between $5 - 10$ TeV in Λ on top of the di-lepton Razor exclusion in the slepton region. This analysis requires two OS leptons and at least two to four jets, and has a higher acceptance for these high Λ points. The comparison between these analyses and their performance regarding the GMSB grid is expanded upon in Section 7.3

7.2.2 Limits on mSUGRA

Limits are shown on the mSUGRA grid with $\tan\beta = 10$, $A_0 = 0$, and $\mu > 0$ in Figure 7.8. The Razor di-lepton limit is able to exclude slightly less parameter space compared with the 8 TeV ATLAS SS di-lepton analysis [62]. This analysis selects events with exactly two same-sign leptons, at least four jets, and missing transverse momentum. The analysis is more selective in that it does not include the OS channels. At low m_0 the di-lepton Razor limits are still competitive, despite the fact that the SS analysis here is performed on 2012 data. This means higher centre-of-mass energy and integrated luminosity. At high m_0 the SS analysis clearly excludes up to higher $m_{1/2}$ compared with the Razor. Of course, the Razor signal regions were not optimised for this model.

Figure 7.9 shows the ATLAS Razor limits on mSUGRA for the zero-, one- and two-lepton channels, as well as the combined limit. The zero-lepton line dominates at low m_0, with the leptonic channels contributing more as m_0 increases and longer decay chains become more common. The two-lepton line on this plot is slightly higher in $m_{1/2}$ compared to the Razor contour of Figure 7.9. The Razor analysis combines all search channels (zero-, one- and two-lepton) and as such the simultaneous background fit – applied only to the two-lepton control regions in the analysis presented here – is applied to all control regions. The full Razor analysis at ATLAS includes two additional one-lepton top control regions, offering a better constraint

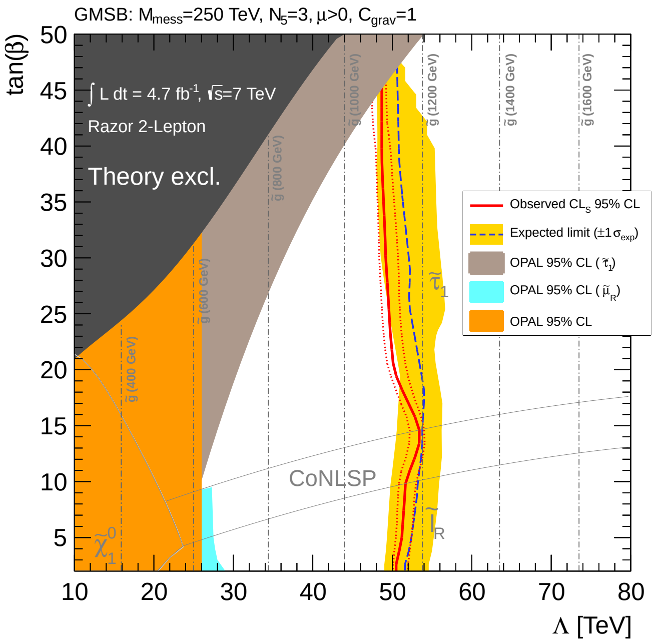

Figure 7.7: Di-lepton exclusion results for the GMSB. The red dotted line denotes the theory signal cross-section uncertainty on the observed limit.

for the top background. Since this background is dominant in the OS channels this extra constraint is important, and this is reflected in the exclusion reach. In addition to this, W control regions defined in the one-lepton channel result in the combination placing tighter constraints on the di-lepton $Z+X$ background. This is due to the fact that the backgrounds due to W- and Z-bosons are merged to form a single input sample for HistFitter, and as such these backgrounds are treated as one [44].

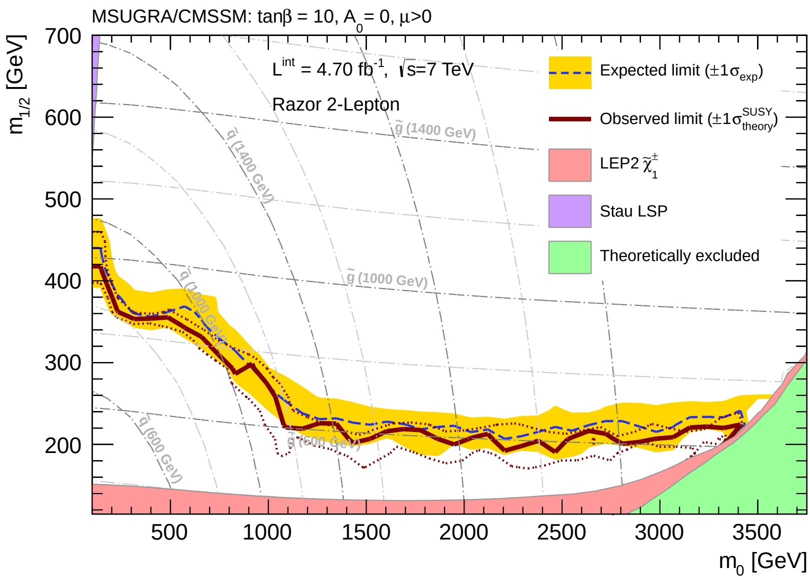

Figure 7.8: Di-lepton exclusion results for mSUGRA. The red dotted line denotes the theory signal cross-section uncertainty on the observed limit.

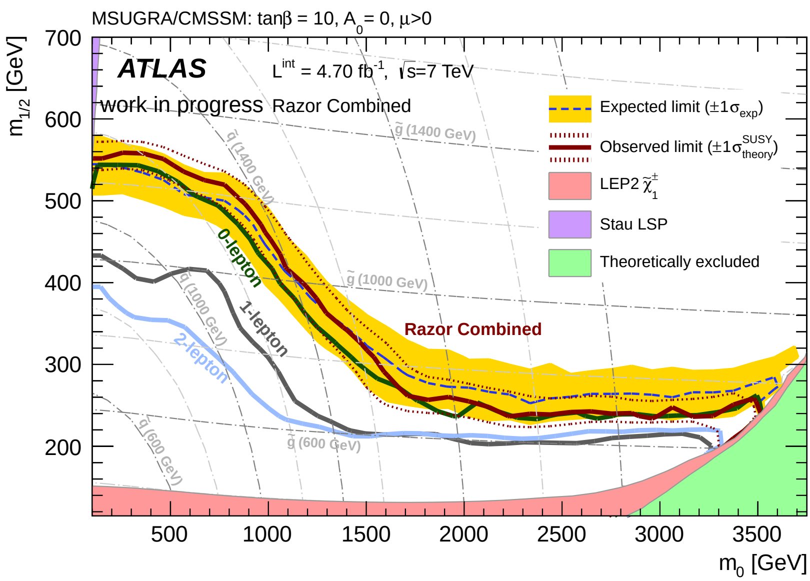

Figure 7.9: The exclusion resulting from all Razor signal regions and control regions. The individual channel contours shown represent the observed exclusion limits.

7.2.3 Interpretation Using Simplified Models

The results of this analysis are interpreted further using two separate SUSY-inspired simplified models, outlined in Section 6.1.3. Lower limits are placed on the LSP and gluino masses in both cases, with the resulting exclusion shown in the LSP mass – gluino mass plane in Figures 7.10 and 7.11.

The effect of the additional top control regions contributing to the combined Razor analysis, as discussed in the previous section, can be further seen here. Comparing the exclusion line shown on the upper plot of Figure 7.10 with the two-lepton line shown on the lower plot, the two-lepton exclusion is stronger with the extra background constraint. In some places the individual channel exclusion lines push beyond the exclusion contour resulting from the combination. The lines drawn for each individual channel represent the "observed" limits and not the "expected." In this case the zero-lepton channel produced a higher observed limit than expected, with both the one- and two-lepton channels being unable to reach their full exclusion potential. This is due, in the two-lepton channel, to a slight excess of events in the SS channels. For this reason the zero-lepton channel is driving the exclusion out, while the one- and two-lepton channels are effectively weakening the reach of the contour in this case.

The hadronic analyses push out to higher values of gluino mass where the fractional mass splitting is larger, with the di-lepton final state more sensitive to lower mass splitting SUSY.

Finally the di-lepton results are applied to a simplified model featuring a one step decay $\tilde{g} \to qq\tilde{\chi}_1^{\pm} \to W^{\pm}\tilde{\chi}_1^0$. Figure 7.11 shows the di-lepton and combined Razor limits. The inclusion of the additional top control regions in the di-lepton channel again appears to improve the di-lepton exclusion. In this case the two-lepton contribution to the combined Razor limit extends further to gluino and LSP masses of 600 and 270 GeV respectively in the latter case (Figure 7.11, lower plot), with the exclusion being limited to higher mass-splittings around a gluino mass of $\sim$ 600 GeV in the two-lepton only interpretation (Figure 7.11, upper plot). The limits placed on this model by the Razor combination are consistent with those set by the ATLAS one-lepton SUSY analysis [61].

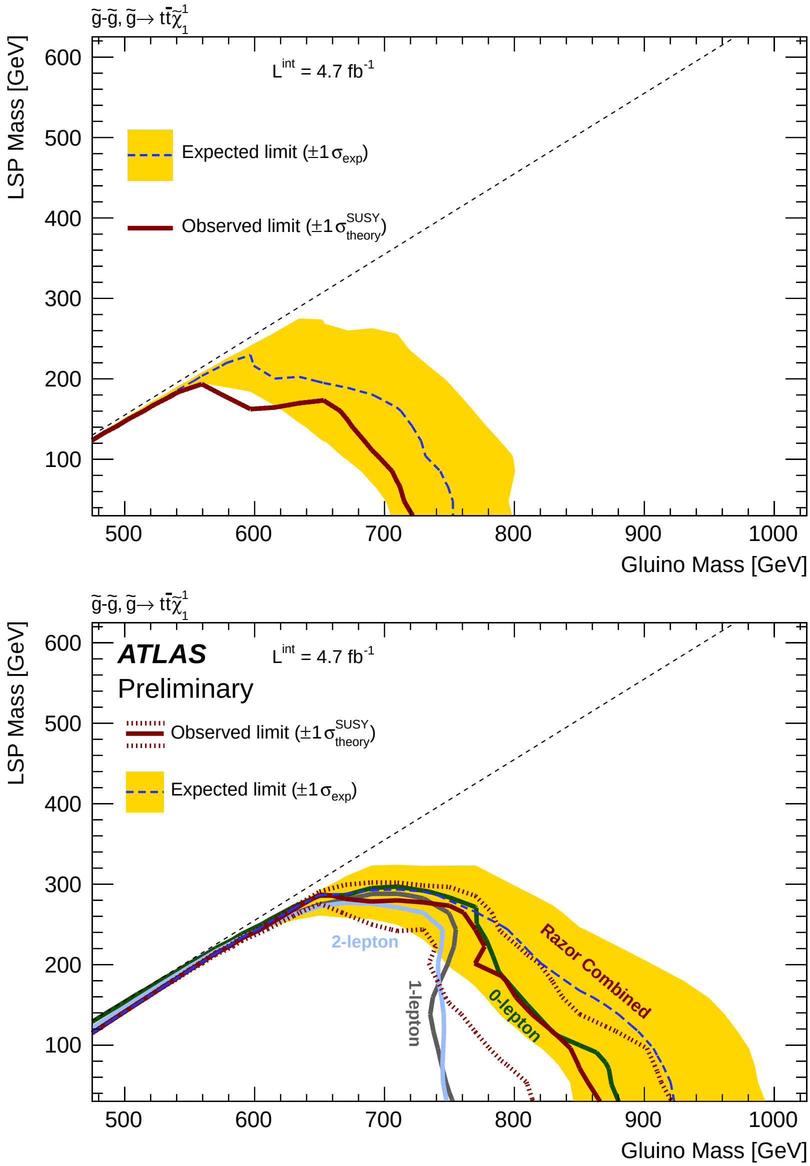

Figure 7.10: Di-lepton Razor exclusion results for the di-lepton only (top) and the combined Razor analysis (bottom). On the lower plot the individual channel contours shown represent the observed exclusion limits. The exclusion is done for a gluino pair-production simplified model, where the gluinos decay via the emission of a $t\bar{t}$ pair to the LSP.

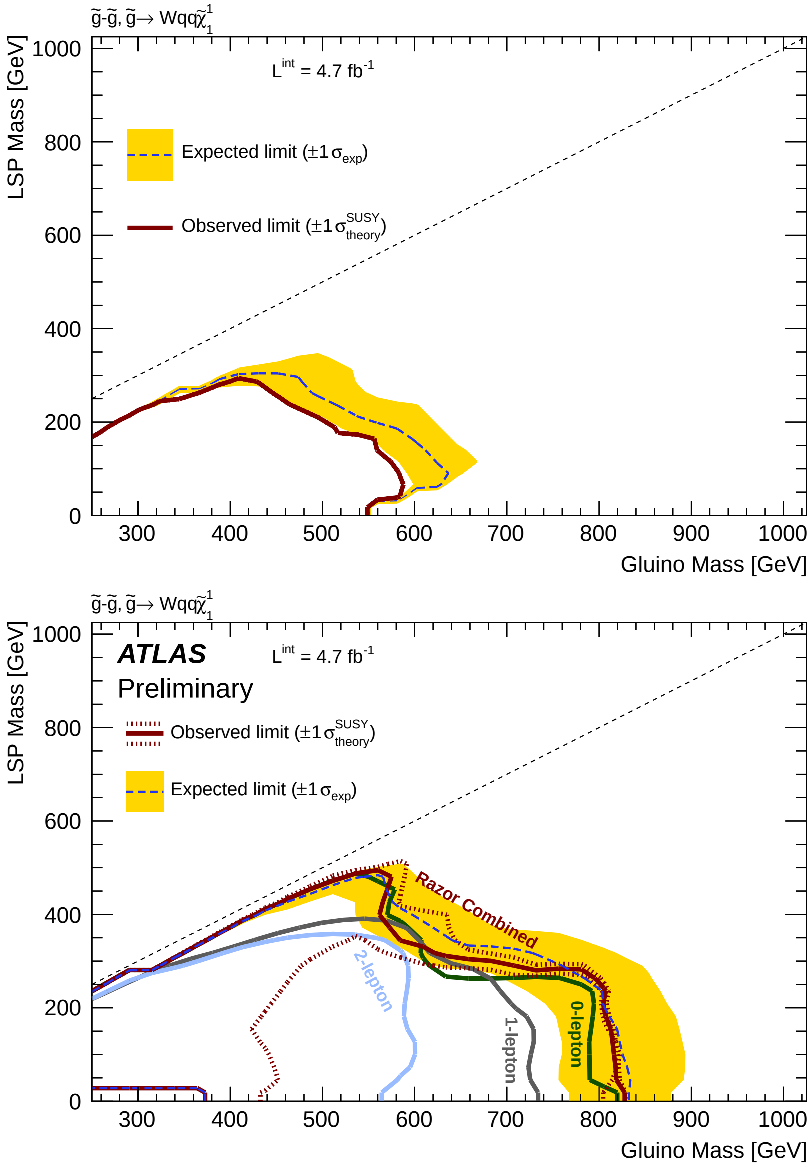

Figure 7.11: Di-lepton Razor exclusion results for the di-lepton only (top) and the combined Razor analysis (bottom). On the lower plot the individual channel contours shown represent the observed exclusion limits. The exclusion is done for a gluino pair-production simplified model, where the gluinos decay to a chargino via the emission of two quarks, with the chargino subsequently decaying into a W-boson.

7.3 Analysis Overlap

At ATLAS there are many SUSY analyses taking place, and the di-lepton Razor signal regions are not the only ones specifying a two-lepton selection, as already shown in Section 7.2. For the 2011 5 fb^{-1} analysis round three additional analysis groups, totalling an additional 7 signal regions, performed SUSY searches focusing on two final state leptons. These analyses, along with their respective signal region selections, are listed in Table 7.3. Part of the motivation for employing the help of the Razor variables to perform a SUSY search is that they attempt to isolate a certain event topology. Cutting on the Razor variables should select a different subset of signal events compared with searches using standard high-E_T^{miss} selections, for example. In order to verify whether or not the use of the Razor variables does indeed permit the selection of events from a different region of phase space compared with searches based on other variables, a comparison is made between the events selected in the signal regions of the di-lepton Razor and other ATLAS di-lepton SUSY analyses. This comparison is made using a signal point close to the 5 fb^{-1} exclusion limit, with $\Lambda = 50$ and $\tan\beta = 15$.

The total number of events overlapping in each signal region can be seen in Figure 7.12. The numbers along the diagonal denote the total number of events in each SR, with those off the diagonal corresponding to the number of events occurring in both the SRs indicated on the x and y axes. Figure 7.13 shows the fraction of events in the SR on the y-axis that overlap with events in the corresponding SR on the x-axis. These plots show that the Razor OS signal regions have moderate overlap with the strong production signal regions, as well as the OS 2-jet SR. From Figure 7.12, this overlap is of order 100 events, though as shown in Figure 7.13 this makes up only $\sim 20 - 30\%$ of the total event selection in these regions. In the case of the SS Razor SRs the overlap is tiny, with only one event occurring in the Strong Production signal regions. This relatively small event overlap supports the claim that cutting on the Razor variables does indeed seek out different events than the other two-lepton analyses.

Analysis Group	Signal Region	Selection Cuts	Number of SR Events
Direct Gaugino/Slepton [59]	SS jet-veto	jet-veto	
		$E_T^{miss,rel} > 100$ GeV	22
	OS jet-veto	jet-veto	
		$E_T^{miss,rel} > 100$ GeV	
		$\|M_Z - M_{\ell\ell}\| > 10$ GeV	432
	OS 2-jet	same flavour leptons	
		≥ 2 jets	
		b-jet veto	
		M_{CT} top-tag veto	
		$\|M_Z - M_{\ell\ell}\| > 10$ GeV	
		$E_T^{miss,rel} > 50$ GeV	377
	OS mT2	same flavour leptons	
		jet-veto	
		$\|M_Z - M_{\ell\ell}\| > 10$ GeV	
		$E_T^{miss,rel} > 40$ GeV	
		$M_{T2} > 90$ GeV	347
Strong Production [61]	OS 4-jet	≥ 4 jets $p_T > 50$ GeV	
		$M_{eff} > 650$ GeV	
		$E_T^{miss} > 100$ GeV	
		$E_T^{miss}/M_{eff} > 0.2$	546
	OS 2-jet	≥ 2 jets $p_T > 200$ GeV	
		if ≥ 4 jets ($p_T > 25$ GeV): j_4 $p_T < 50$ GeV	
		$E_T^{miss} > 300$ GeV	344
2-tau [45]	2-tau	$\Delta\phi(\text{jet}_{1,2}, E_T^{miss}) \geq 0.4$	
		$M_{T1} + M_{T2} \geq 100$ GeV	
		$H_T \geq 650$ GeV	71
Razor	SS	$\gamma_R \times M_R > 500$	
		$R > 0.25$	269
	OS	$\gamma_R \times M_R > 600$	
		$R > 0.4$	409

Table 7.3: List of di-lepton analysis groups and associated signal region cuts and event counts for 5 fb^{-1} 2011 analyses [63]. The numbers given in the last column represent the number of selected events a the GMSB signal model with $\Lambda = 50$ TeV and $\tan\beta = 15$.

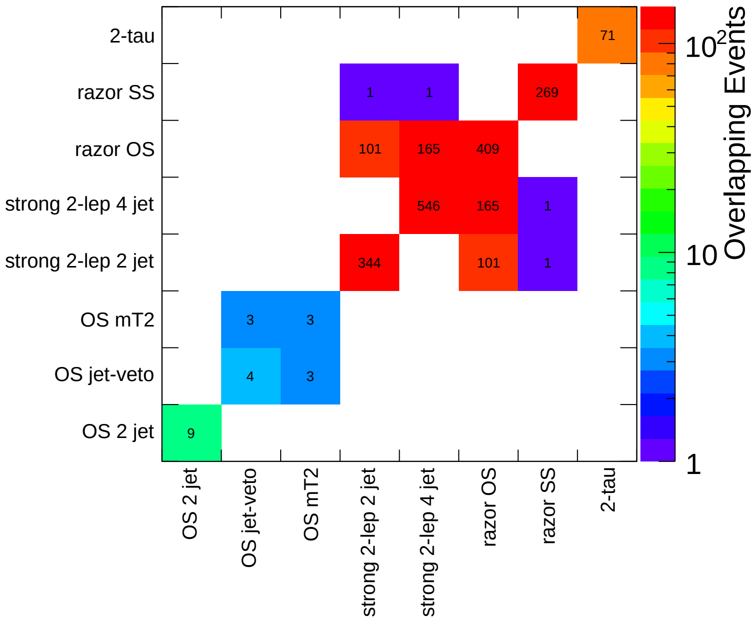

Figure 7.12: Total event overlap between 2011 di-lepton signal regions. The signal model is a GMSB signal point with parameters $\Lambda = 50$ and $\tan\beta = 15$. The plot shows the number of events occurring in both SR x and SR y.

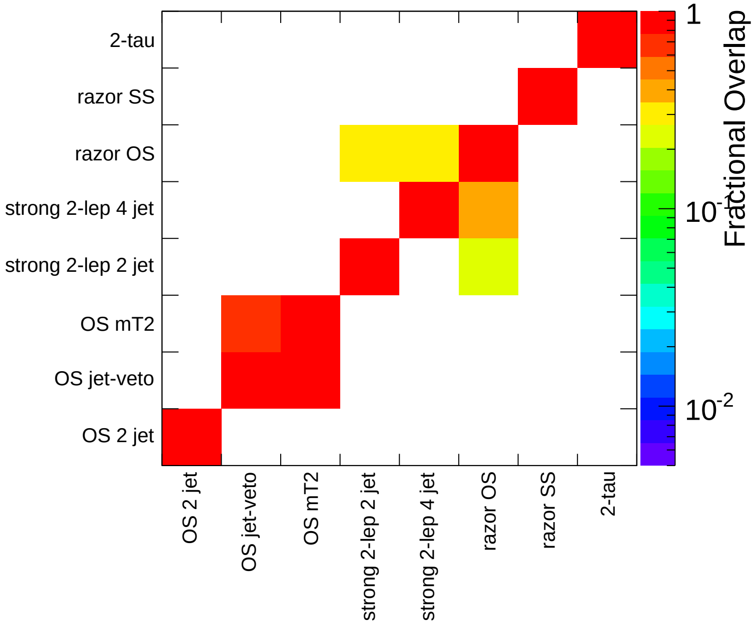

Figure 7.13: Fractional event overlap between 2011 di-lepton signal regions. The signal model is a GMSB signal point with parameters $\Lambda = 50$ and $\tan\beta = 15$. The plot shows the fraction of the total events occurring in SR y that are also contained within SR x.

Chapter 8

Conclusions and Future Prospects

A search for supersymmetry in di-lepton final states in proton-proton collisions at $\sqrt{s} = 7$ TeV using the Razor variables has been presented. This analysis makes use of the full ATLAS 2011 dataset, with an integrated luminosity of 4.7 fb^{-1} in total.

A thorough assessment of the Standard Model and fake backgrounds to the di-lepton SUSY search were presented in Section 6.2. The background due to charge mis-identification posed a particular challenge, with much of the uncertainty on the background estimates in the same-sign channels being due to the uncertainty on the charge flip weights assigned. The obtained charge flip distributions fit well to the data, with the process of disentangling the fake background being vital to obtaining the achieved agreement. This background merits further study in the future, with attention towards better understanding of the p_T- and η- dependence of the charge flip probabilities. The $Z + X$ background according to simulated events has been shown to match distributions in 2011 data within the statistical uncertainties. The top background dominated the opposite-sign signal regions, with three separate control regions being used to constrain it (five for the full combined Razor analysis). Data-driven investigations of this background will be of utmost importance in any future Razor effort selecting two OS leptons.

The di-lepton Razor analysis places an exclusion limit on the GMSB model described in Section 6.1.1 out to a gluino mass of 1100 GeV (1200 at low $\tan\beta$) to 95% C.L. Limits are also set on the cMSSM with parameter values as described in Section 6.1.2. Where the gluino and squark masses are equal the di-lepton excludes up to squark and gluino masses of ~ 1000 GeV. The results are interpreted further using SUSY-inspired simplified models involving gluino pair-production. In one of these the gluinos decay to the LSP via the emission of a $t\bar{t}$ pair. The limits set on this model exclude LSP and gluino masses up to 200 and 720 GeV, respectively. An interpretation using another model where the gluinos decay via the emission of two quarks to a chargino, with the chargino decaying to the LSP and a W-boson, is also made. In this case limits are placed up to LSP and gluino masses of 250 and

550 GeV, respectively.

This is the first time that the Razor variables have been used within the ATLAS collaboration. The results in Section 7.2 show that the di-lepton analysis produces consistent, but not strikingly improved limits. A higher number of GMSB signal events enter the signal regions (based on E_T^{miss} and M_{eff} cuts) of the two-lepton strong production analysis [61] than those based on the Razor variables. The signal regions of the two-lepton strong production analysis [61] select $\sim$ 900 events from the GMSB signal point in Section 7.3 compared with the $\sim$ 700 of the di-lepton Razor. Couple this with the fact that the expected background contribution in these signal regions is approximately half that in the Razor signal regions, and the further exclusion in Λ acheived by the strong production analysis is unsurprising It is possible that introducing jet requirements to the signal selection in conjunction with lower thresholds on R and $\gamma_R \times M_R$ could increase the sensitivity to the GMSB. This is a point of consideration for the upcoming analysis on the new 8 TeV dataset. Alternatively the superiority of the Razor variables may become apparent when applied to SUSY models not explored in this analysis round. For now the ATLAS Razor exclusion serves to corroborate the recent limits set by other ATLAS SUSY analyses, rather than extend them.

The effort to better understand the behaviour of the Razor variables with respect to various different topologies and phenomenologies is ongoing. The Razor selection truly does sample events from a different region of SUSY phase space. This is certain from the results of the overlap studies of Section 7.3. If the goal of a SUSY search genuinely is to uncover SUSY, then accessing regions of phase space untouched by other analyses is desirable for the fulfilment of a comprehensive search. Unfortunately there are an enormous number of possible SUSY scenarios, and excluded regions are extending ever further into parameter space.

With the use of the Razor variables being a new concept at ATLAS the analysis started out as an exploratory endeavour. Over its course many points of potential improvement were identified, being built on in some instances and left for implementation in future analyses in others. In this respect the analysis attempts to cover a somewhat broad range of signal models, in a generic SUSY search. Despite yielding competitive limits, it is likely that in some cases, were the models in question the focus of the optimisation, the Razor analysis may have out-performed the standard analyses. This lesson should be applied to the next iteration of the analysis, with more emphasis on research into signal models for which the Razor is best suited.

A novelty of the Razor variables is the way in which they can be applied to multiple final states in a consistent and strategic manner. The Razor analysis at ATLAS is carried out using the combination of zero-, one- and two-lepton channels, rather than pursuing SUSY scenarios based upon final state alone. This is the first time such a strategy has been employed at ATLAS. Here lies an area where the analysis can definitely be built upon, and where such a variable set may present an advantage. During the first iteration the analysis was largely experimental and perhaps overly cautious. The zero-, one-, and two-lepton channels were subject to signal region optimisation based on individual signal models for the 7 TeV analysis. If all channels optimise for a common model for which all these final states are accessible, the large acceptance might increase the sensitivity of the Razor compared with other methods. Such models will be investigated during the re-optimisation taking place for the 8 TeV data of 2012.

Acknowledgments

I would like to thank Bengt Lund-Jensen for providing me with the opportunity to undertake my Ph.D. studies at KTH, and for facilitating my work and long term stays at CERN. Thank you for your ongoing support. Many thanks also to Jonas Strandberg for providing guidance and advice over the past year. I would like to acknowledge everyone at the Particle and Astroparticle Physics department at KTH for making me welcome. My gratitude goes to Jelena, Merlin, Elena and Laura in particular - thank you for interesting conversations, lots of laughter and for always being up for a beer at the Doors! Thanks also to Christoffer, Moszi and Oscar for countless lunchtime stories, discussions and jokes (Oscar).

This work would not have been possible without the support from, and collaboration with, my colleagues at CERN. I would particularly like to thank Olivier Simard for his direction during many LAr based studies, and for being patient with my limited coding knowledge. Many thanks also to Maud Schwoerer, Thi Hong Van Nguyen, Isabelle Wingerter-Seez, Jessica Leveque and Benjamin Trocme, for providing guidance and playing their part in the “LAr noise” party.

I am eternally grateful to Louise Heelan and Zach Marshall for introducing me to the Razor analysis, and have very much enjoyed working as part of Team Razor. A big thank you to Travis Bain for describing the Razor variables in an accesible manner and providing extra motivation for pushing this analysis through! An even bigger thank you to Zach, who is still fighting to get our paper published, and has helped me no end to develop my skill set. I would also like to especially thank Remi Lafaye for his input and influence over the course of the analysis, and for always being available to talk things over on Skype.

I truly appreciate the Sussex ATLAS group who continue to look out for me even though I have flown their nest. I would like to thank Devin for introducing me to the SUSY group, for the countless coffee breaks, for the useful discussions and for his valuable friendship. Finally, thank you to Sudan, for giving me direction when I was lost, and for keeping me smiling.

List of Figures

List of Tables

References

[1] B. R. Martin and G. Shaw, *Particle Physics* (John Wiley and Sons) (1997).

[2] M. Peskin and D. Schroeder, *An Introduction to Quantum Field Theory* (Westview Press, Boulder, CO) (1995).

[3] F. Abe *et al.*, the **CDF** Collaboration, *Observation of Top Quark Production in p p Collisions with the Collider Detector at Fermilab*. Phys. Rev. Lett. **74**, (1995) 2626–2631, [`doi: 10.1103/PhysRevLett.74.2626`].

[4] B. Aharmim *et al.*, the **SNO** Collaboration, *Independent Measurement of the Total Active 8B Solar Neutrino Flux Using an Array of 3He Proportional Counters at the Sudbury Neutrino Observatory*. Phys. Rev. Lett. **101**, [`doi: 10.1103/PhysRevLett.101.111301`].

[5] K. Abe *et al.*, the **Super-Kamiokande** Collaboration, *Solar neutrino measurements in Super-Kamiokande-II*. Phys. Rev. Lett. **D78**, [`doi: 10.1103/PhysRevD.78.032002`].

[6] J. Beringer et al., the **Particle Data Group** Collaboration, *Particle Data Group*. Phys. Rev. **D86**, (2012) 010001.

[7] G. Aad *et al.*, the **ATLAS** Collaboration, *The ATLAS Experiment at the CERN Large Hadron Collider*. JINST **3**, [`doi: 10.1088/1748-0221/3/08/S08003`].

[8] S. Chatrchyan *et al.*, the **CMS** Collaboration, *The CMS Experiment at the CERN Large Hadron Collider*. JINST **3**, [`doi: 10.1088/1748-0221/3/08/S08004`].

[9] G. Aad *et al.*, the **ATLAS** Collaboration, *Observation of a new particle in the search for the Standard Model Higgs boson with the ATLAS detector at the LHC*. Phys. Lett. **B716**, [`doi: 10.1016/j.physletb.2012.08.020`].

[10] S. Chatrchyan *et al.*, the **CMS** Collaboration, *Observation of a new boson at a mass of 125 GeV with the CMS experiment at the LHC*. submitted Phys. Lett. B [`arXiv:1207.7235`].

[11] S. Weinberg, *Implications of Dynamical Symmetry Breaking*. Phys. Rev. **D13**, (1976) 974–996, [`doi: 10.1103/PhysRevD.13.974`].

[12] K. Abe *et al.*, the **Super-Kamiokande** Collaboration, *Search for Proton Decay via $p \to e\pi^0$ in a Large Water Cherenkov Detector*. Phys. Rev. Lett. **81**, (1998) 3319–3323, [`doi: 10.1103/PhysRevLett.102.141801`].

[13] F. Zwicky, *On the Masses of Nebulae and of Clusters of Nebulae*. Astrophysical Journal **86**, [`doi: 10.1086/143864`].

[14] E. Komatsu et. al., *Five-Year Wilkinson Microwave Anisotropy Probe (WMAP) Observations: Cosmological Interpretation*. Ap. J. S. **180**, [`doi: 10.1088/0067-0049/180/2/330`].

[15] K. Aamodt *et al.*, the **ALICE** Collaboration, *The ALICE Experiment at the CERN Large Hadron Collider*. JINST **3**, [`doi: 10.1088/1748-0221/3/08/S08002`].

[16] A. A. Alves *et al.*, the **LHCb** Collaboration, *The LHCb Experiment at the CERN Large Hadron Collider*. JINST **3**, [`doi: 10.1088/1748-0221/3/08/S08005`].

[17] *ATLAS Public Results TWiki*. https://twiki.cern.ch/twiki/bin/view/AtlasPublic.

[18] G. Aad *et al.*, the **ATLAS** Collaboration, *ATLAS Insertable B-Layer: Technical Design Report*. ATLAS-TDR 019 (2010).

[19] M. Aharrouche *et al.*, the **ATLAS Electromagnetic Barrel Calorimeter** Collaboration, *Energy Linearity and Resolution of the ATLAS Electromagnetic Barrel Calorimeter in an Electron Test-Beam*. Nucl. Istrum. Meth. **A568**, (2006) 601–623, [`arXiv:0608.012`].

[20] P. Strizenec *et al*, *Performance of the ATLAS Liquid Argon End-cap Calorimeter in Beam Tests*. J. Phys.: Conf. Ser. **106**, [`doi: 10.1088/1742-6596/160/1/012078`], [`012078`].

[21] C.Cojocaru *et al.*, *Hadronic Calibration of the ATLAS Liquid Argon End-Cap Calorimeter in the Pseudorapidity Region* $1.6 < |eta| < 1.8$ *in Beam Tests*. Nucl. Istrum. Meth. **A531**, (2004) 481–514, [`0407009`].

[22] T. Davidek, *ATLAS Tile Calorimeter performance for single particles in beam tests*. J. Phys.: Conf. Ser. **160**, [`doi: 10.1088/1742-6596/160/1/012057`], [`012057`].

[23] G. Aad *et al.*, the **ATLAS** Collaboration, *Position Resolution and Particle Identification with the ATLAS EM Calorimeter*. Nucl. Istrum. Meth. **A550**, (2005) 95–115, [`arXiv:0505.127`].

[24] G. Aad *et al.*, the **ATLAS** Collaboration, *ATLAS Detector and Physics Performance: Technical Design Report Volume I*. ATLAS-TDR 014 (1999).

[25] G. Aad *et al.*, the **ATLAS** Collaboration, *Comissioning of the ATLAS Muon Spectrometer with Cosmic Rays*. Eur. Phys. J. **C70**, (2010) 875–916, [`arXiv:1006.4384`].

[26] G. Aad *et al*, the **ATLAS** Collaboration, *Electron performance measurements with the ATLAS detector using the 2010 LHC proton-proton collision data.* Eur. Phys. J. **C72**, [arXiv:1110.3174].

[27] G. Aad *et al.*, the **ATLAS** Collaboration, *Further search for supersymmetry at sqrt(s) = 7 TeV in final states with jets, missing transverse momentum and one isolated lepton.* ATLAS-CONF 2012-041 (2012).

[28] G. Aad *et al.*, the **ATLAS** Collaboration, *A measurement of the atlas muon reconstruction and trigger efficiency using j/psi decays.* ATLAS-CONF 2011-021 (2011).

[29] G. Aad *et al.*, the **ATLAS** Collaboration, *Muon reconstruction efficiency in reprocessed 2010 LHC proton-proton collision data recorded with the ATLAS detector* (2011-063).

[30] G. P. Salam M. Cacciari and Gregory Soyez, *The anti-k_t jet clustering algorithm.* JHEP **04**, (2008) 063, [doi: 10.1088/1126-6708/2008/04/063], [arXiv:0802.1189].

[31] M. Cacciari and G.P. Salam, *Dispelling the N**3 myth for the k(t) jet-finder.* Phys. Lett. **B641**, (2006) 57–61, [doi: 10.1016/j.physletb.2006.08.037], [hep-ph/0512210], http://fastjet.fr/.

[32] G. Aad *et al.*, the **ATLAS** Collaboration, *Readiness of the ATLAS Tile Calorimeter for LHC collisions.* Eur. Phys. J. **C70**, (2010) 1193–1236, [doi: 10.1140/epjc/s10052-010-1508-y], [arXiv:1434.6052].

[33] G. Aad *et al.*, the **ATLAS** Collaboration, *Jet energy scale and its systematic uncertainty in ATLAS for jets produced in proton-proton collisions at $\sqrt{s}$=7 TeV.* ATLAS-CONF 2010-056 (2010).

[34] G. Aad *et al.*, the **ATLAS** Collaboration, *Measurement of inclusive jet and dijet cross sections in proton-proton collisions at 7 TeV centre-of-mass energy with the ATLAS Detector.* Eur. Phys. J. **C71**, (2010) 1512, [doi: 10.1140/epjc/s10052-010-1512-2], [arXiv:1009.5908].

[35] G. Aad *et al.*, the **ATLAS** Collaboration, *Data-Quality Requirements and Event Cleaning for Jets and Missing Transverse Energy Reconstruction with the ATLAS Detector in Proton-Proton Collisions at a Center-of-Mass Energy of $\sqrt{s} = 7$ TeV.* ATLAS-CONF 2010-038, Geneva (2010).

[36] G. Piacquadio and C. Weiser, *A new inclusive secondary vertex algorithm for b-jet tagging in ATLAS.* J. Phys.: Conf. Ser. **119**, [doi: 10.1088/1742-6596/119/3/032032].

[37] G. Aad *et al.*, the **ATLAS** Collaboration, *Updated Luminosity Determination in pp Collisions at sqrt(s) = 7 TeV using the ATLAS Detector.* ATLAS-CONF 2011-011 (2011).

[38] G. Aad *et al.*, the **ATLAS** Collaboration, *ATLAS Computing: Technical Design Report.* ATLAS-TDR 017 (2005).

[39] C. Rogan, *Kinematics for new dynamics at the LHC* [arXiv:1006.2727].

[40] S. Chatrchyan *et al.*, the **CMS** Collaboration, *Search for supersymmetry with the razor variables.* CMS-PAS-SUS 11-008 (2011).

[41] S. Chatrchyan *et al.*, the **CMS** Collaboration, *Search for supersymmetry with the razor variables at CMS.* CMS-PAS-SUS 12-005 (2012).

[42] S. Chatrchyan *et al.*, the **CMS** Collaboration, *Search for supersymmetry with the razor variables at CMS.* CMS-PAS-SUS 11-024 (2012).

[43] S. Chatrchyan *et al.*, the **CMS** Collaboration, *A search for the decays of a new heavy particle in multijet events with the razor variables at CMS in pp collisions at sqrt(s)=7 TeV.* CMS-PAS-SUS 12-009 (2012).

[44] T. Bain *et al.*, the **ATLAS** Collaboration, *A search for supersymmetry using the razor variables in pp collisions at* $\sqrt{s} = 7$ *TeV with the ATLAS detector* (ATL-COM-PHYS-2012-057).

[45] G. Aad *et al.*, the **ATLAS** Collaboration, *Search for events with large missing transverse momentum, jets, and at least two tau leptons in 7 TeV proton-proton collision data with the ATLAS detector.* submitted to Phys. Lett. B [arXiv:1203.6580].

[46] G. Corcella *et al.*, *HERWIG 6: An event generator for hadron emission reactions with interfering gluons (including supersymmetric processes).* JHEP **01**, (2001) 010, [doi: 10.1088/1126-6708/2001/01/010], [hep-ph/0011363].

[47] R. Hoepker W. Beenakker and M. Spira, *PROSPINO: A Program for the Production of Supersymmetric Particles in Next-to-leading Order QCD* (1996), [9611232].

[48] M. Bahr *et al.*, *Herwig++ Physics and Manual.* Eur. Phys. J. **C58**, (2008) 639–707, [doi: 10.1140/epjc/s10052-008-0798-9], [arXiv:0803.0883].

[49] J. Alwall *et al.*, *MadGraph/MadEvent v4: The New Web Generation.* JHEP **09**, (2007) 028, [doi: 10.1088/1126-6708/2007/09/028], [arXiv:0706.2334].

[50] T. Sjostrand, S. Mrenna, and P. Skands, *PYTHIA 6.4 physics and manual.* JHEP **0605**, (2006) 026, [doi: 10.1088/1126-6708/2006/05/026], [hep-ph/0603175].

[51] M.L. Mangano *et al.*, *ALPGEN, a generator for hard multiparton processes in hadronic collisions.* JHEP **07**, (2003) 001, [doi: 10.1088/1126-6708/2003/07/001], [hep-ph/0206293].

[52] P. Motylinski S. Frixione, E. Laenen and B. R. Webber, *Single-top production in MC@NLO.* JHEP **03**, (2006) 092, [doi: 10.1088/1126-6708/2006/03/092], [hep-ph/0512250].

[53] S. Agostinelli et al, *Geant4 - a simulation toolkit.* Nucl. Instr. and Meth. **A506**, (2003) 250.

[54] G. Aad *et al.*, the **ATLAS** Collaboration, *The ATLAS Simulation Infrastructure.* Eur. Phys. J **C70**, (2010) 823–874, [`arXiv:1005.4568`].

[55] *Hist Fitter TWiki.* https://twiki.cern.ch/twiki/bin/viewauth/AtlasProtected/SusyFitter.

[56] *HistFactory Documentation.* https://twiki.cern.ch/twiki/pub/RooStats/WebHome/HistFactoryLikelihood.pdf.

[57] B. Abi *et al.*, *Mis-identified lepton backgrounds to top quark pair production for Moriond 2011 analysis* URL `https://cdsweb.cern.ch/record/1328921`.

[58] G. Aad *et al.*, the **ATLAS** Collaboration, *Search for supersymmetric particles in events with lepton pairs and large missing transverse momentum in* $\sqrt{s} = 7$ *TeV proton-proton collisions with the ATLAS experiment.* Eur. Phys. J. **C71**, (2011) 1682, [`arXiv:1103.6214`].

[59] I. Santoyo Castillo *et al.*, the **ATLAS** Collaboration, *Searching for direct gaugino production and direct slepton production with two leptons and missing transverse momentum at* $\sqrt{s} = 7$ *TeV (supporting INT note).* ATL-COM-PHYS 2011-1721 (2012).

[60] A. Read, *Presentation of search results: the* CL_s *technique.* J. Phys. G: Nucl. Part. Phys. **28**(10), (2002) 26932704, [`doi: 10.1088/0954-3899/28/10/313`].

[61] G. Aad *et al.*, the **ATLAS** Collaboration, *Further search for supersymmetry at* $\sqrt{s} = 7$ *TeV in final states with jets, missing transverse momentum and isolated leptons with the ATLAS detector* [`arXiv:1208.4688`].

[62] G. Aad *et al.*, the **ATLAS** Collaboration, *Search for Supersymmetry in final states with two same-sign leptons, jets and missing transverse momentum with the ATLAS detector in pp collisions at* $\sqrt{s} = 8$ *TeV.* ATLAS-CONF 2012-028 (2012).

[63] M. Lungwitz, A. Rose, F. Salvatore, B. Toggerson. Private communication.